



저작자표시-비영리-변경금지 2.0 대한민국

이용자는 아래의 조건을 따르는 경우에 한하여 자유롭게

- 이 저작물을 복제, 배포, 전송, 전시, 공연 및 방송할 수 있습니다.

다음과 같은 조건을 따라야 합니다:



저작자표시. 귀하는 원저작자를 표시하여야 합니다.



비영리. 귀하는 이 저작물을 영리 목적으로 이용할 수 없습니다.



변경금지. 귀하는 이 저작물을 개작, 변형 또는 가공할 수 없습니다.

- 귀하는, 이 저작물의 재이용이나 배포의 경우, 이 저작물에 적용된 이용허락조건을 명확하게 나타내어야 합니다.
- 저작권자로부터 별도의 허가를 받으면 이러한 조건들은 적용되지 않습니다.

저작권법에 따른 이용자의 권리는 위의 내용에 의하여 영향을 받지 않습니다.

이것은 [이용허락규약\(Legal Code\)](#)을 이해하기 쉽게 요약한 것입니다.

[Disclaimer](#)

공학박사 학위논문

Self-Scheduled Parameter-Varying Control of Asymmetric
Variable-Span Morphing Unmanned Aerial Vehicle

비대칭 가변스팬 모핑 무인 항공기의 자체스케줄 파라미터 가변 제어

2023 년 2 월

서울대학교 대학원

기계항공공학부

이 지 훈

Self-Scheduled Parameter-Varying Control of
Asymmetric Variable-Span Morphing Unmanned
Aerial Vehicle

비대칭 가변스팬 모핑 무인 항공기의 자체스케줄 파라미터 가변 제어

지도교수 김 유 단

이 논문을 공학박사 학위논문으로 제출함

2022 년 12 월

서울대학교 대학원

기계항공공학부

이 지 훈

이지훈의 공학박사 학위논문을 인준함

2022 년 12 월

위 원 장 김 현 진 (인)

부위원장 김 유 단 (인)

위 원 박 찬 국 (인)

위 원 심 형 보 (인)

위 원 박 종 호 (인)

Self-Scheduled Parameter-Varying Control of
Asymmetric Variable-Span Morphing Unmanned
Aerial Vehicle

by

Jihoon Lee

Submitted to the Graduate School of
Seoul National University
in partial fulfillment of the requirements for the degree of

Doctor of Philosophy

Department of Mechanical and Aerospace Engineering
Seoul National University

Advisor: Prof. Youdan Kim

February 2023

Self-Scheduled Parameter-Varying Control of
Asymmetric Variable-Span Morphing Unmanned
Aerial Vehicle

by

Jihoon Lee

Approved as to style and content by:

H. Jin Kim, Chair, Ph.D.

Youdan Kim, Vice-Chair, Ph.D.

Chan Gook Park, Member, Ph.D.

Hyungbo Shim, Member, Ph.D.

Jongho Park, Member, Ph.D.

Abstract

Self-Scheduled Parameter-Varying Control of Asymmetric Variable-Span Morphing Unmanned Aerial Vehicle

Jihoon Lee

Department of Mechanical and Aerospace Engineering
The Graduate School
Seoul National University

In this dissertation, a novel framework for flight control of a morphing unmanned aerial vehicle (UAV) is proposed. The proposed method uses asymmetric span morphing for lateral-directional motion control considering the dynamic characteristics of the morphing actuators while exploiting the advantages of symmetric span morphing for longitudinal flight performance enhancement. The proposed control system is self-scheduled based on linear parameter-varying (LPV) methods, which guarantees stability and performance for the variations of the morphing configuration and the flight condition. Therefore, the morphing UAV is allowed to swiftly metamorphose into the optimal configuration to maximize the system-level benefit according to the maneuvering command and the flight condition.

First, a high-fidelity nonlinear model of an asymmetric variable-span morphing UAV is obtained from the NASA generic transport model. The impacts of morphing on the center of mass, inertia matrix, and aerodynamic coefficients are modeled based on the asymmetrically damaged wing model. The span variation ratios of the left and right wings are decomposed into symmetric and asymmetric morphing parameters, which are considered as the scheduling parameter and

the control input, respectively. The nonlinear model is decoupled and linearized to obtain point-wise linear time-invariant (LTI) models for the longitudinal and lateral-directional motions throughout the grid points over the entire rectangularized scheduling parameter domain. The LPV model of the morphing UAV is derived for the longitudinal and lateral-directional motions by associating the family of LTI models through interpolation.

Second, the longitudinal and lateral-directional control augmentation systems are designed based on LPV methods to track the normal acceleration command and the angle of sideslip and the roll rate commands, respectively. The inherent dynamic characteristics of the morphing actuator, such as low bandwidth, are considered in the control design procedure through a frequency-dependent weighting filter. The span morphing strategy to assist the intended maneuver is studied considering the impacts of morphing on various aspects. Numerical simulations are performed to demonstrate the effectiveness of the proposed control scheme for pushover-pullup maneuver and high-g turn.

Finally, the longitudinal and lateral-directional autopilots are designed based on LPV methods to track the airspeed and altitude commands and the angle of sideslip and roll angle commands, respectively. A nonlinear guidance law is coupled with the autopilots to enable three-dimensional trajectory tracking. Numerical simulation results for the trajectory-tracking flight show that the proposed controller shows satisfactory performance, while the closed-loop system using the conventional gain-scheduled controller may lose stability when the scheduling parameter varies rapidly or widely.

Keywords: Morphing Aircraft, Unmanned Aerial Vehicle, Linear Parameter-Varying Control, Gain Scheduling, Robust Control, Flight Control System, Con-

trol Augmentation System, Autopilot, Trajectory Tracking, Nonlinear Guidance

Student Number: 2014-22511

Contents

Abstract	i
Contents	v
List of Tables	ix
List of Figures	xi
1 Introduction	1
1.1 Background and Motivation	1
1.2 Literature Review	6
1.2.1 Fixed-Wing Aircraft Implementing Morphing Technologies	6
1.2.2 Flight Control of Morphing Aircraft	7
1.2.3 Gain Scheduling Approaches to Controller Design	7
1.3 Objectives and Contributions	9
1.3.1 Objectives	9
1.3.2 Contributions	9
1.4 Dissertation Outline	11
2 Mathematical Preliminaries	13
2.1 LPV Systems	15
2.1.1 Taxonomy of Dynamical Systems	15

2.1.2	Definition of LPV Systems	15
2.1.3	LPV Modeling by Linearization	20
2.2	Gain Self-Scheduled Induced \mathcal{L}_2 -Norm Control of LPV Systems .	24
2.2.1	Norms of Signals and Systems	24
2.2.2	Analysis of LPV Systems	25
2.2.3	LPV Controller Design	30
2.2.4	Software for Synthesis and Analysis	30
3	Asymmetric Variable-Span Morphing UAV Model	33
3.1	Nonlinear Model of a Morphing UAV	36
3.1.1	Nominal Model of a Baseline Model	36
3.1.2	Morphing UAV Model	41
3.2	Derivation of an LPV Model of a Morphing UAV	52
3.2.1	Trim Analysis and Scheduling Parameter Selection	52
3.2.2	Pointwise Linearization of a Nonlinear Model	55
3.2.3	Linear Parameter-Varying Modeling and Analysis	58
4	CAS Design Based on LPV Method for Morphing-Assisted	
	Maneuvers	61
4.1	Longitudinal CAS Design for Normal Acceleration Control	65
4.1.1	Performance Specifications	65
4.1.2	Controller Synthesis and Analysis	68
4.2	Lateral-Directional CAS Design for Turn Coordination and Roll	
	Rate Control	73
4.2.1	Performance Specifications	73
4.2.2	Controller Synthesis and Analysis	75

4.3	Span Morphing Strategy	83
4.3.1	Effects of Span Morphing	83
4.3.2	Criteria for Span Variation	85
4.4	Nonlinear Simulation of Morphing-Assisted Maneuvers	86
4.4.1	High-Fidelity Flight Dynamics Simulator	86
4.4.2	Push-over and Pull-up	86
4.4.3	High-g Turn	89
5	Autopilot Design Based on LPV Methods for Morphing-Assisted Flights	109
5.1	Longitudinal Autopilot Design for Airspeed and Altitude Control	111
5.1.1	Performance Specifications	111
5.1.2	Controller Synthesis and Analysis	113
5.2	Lateral-Directional Autopilot Design for Turn Coordination and Roll Angle Control	121
5.2.1	Performance Specifications	121
5.2.2	Controller Synthesis and Analysis	123
5.3	Nonlinear Guidance Law for Trajectory Tracking	131
5.4	Nonlinear Simulation of Morphing-Assisted Flights	132
5.4.1	Waypoint Following at Low Altitude	132
5.4.2	Circular Trajectory Tracking at High Altitude	132
5.4.3	Helical Ascent under Fast Morphing	132
5.4.4	Spiral Descent with Morphing Scheduling	139
6	Conclusion	147
6.1	Concluding Remarks	147

6.2 Future Work	148
Bibliography	151
국문초록	177

List of Tables

Table 3.1	Geometrical parameters of the GTM.	35
Table 3.2	Nominal and damaged properties of the GTM.	35
Table 4.1	Typical types of automatic control systems.	62
Table 4.2	Weighting filters for the longitudinal CAS design.	69
Table 4.3	Weighting filters for the lateral-directional CAS design. . .	76
Table 5.1	Weighting filters for the longitudinal autopilot design . . .	114
Table 5.2	Weighting filters for the lateral-directional autopilot design.	124

List of Figures

Figure 2.1	Taxonomy of dynamical systems	16
Figure 2.2	$P - \Theta$ structure of the LPV control system	23
Figure 2.3	LFT representation of the LPV control system	24
Figure 2.4	Open-loop LPV plant	29
Figure 2.5	Generalized open-loop LPV plant	29
Figure 2.6	Closed-loop LPV control system	29
Figure 2.7	LFT representation of the closed-loop LPV control system	29
Figure 3.1	NASA GTM-T2.	34
Figure 3.2	Parameter variation due to η_l when $\eta_r = 0\%$	47
Figure 3.3	Parameter variation due to η_s when $\eta_a = 0\%$	47
Figure 3.4	Maximum variation of the aerodynamic coefficients from the nominal configuration due to morphing when $\beta \in$ $[-20, 20]$ deg.	50
Figure 3.5	Control surface increment to the aerodynamic coeffi- cients when $\beta = 0$ deg.	51
Figure 3.6	Trimmable region of the nominal GTM.	53
Figure 3.7	Rectangular scheduling parameter domain.	54
Figure 3.8	Trim angle of attack and throttle.	56
Figure 3.9	Longitudinal open-loop poles in various configurations. .	59

Figure 3.10	Lateral-directional open-loop poles in various configurations.	60
Figure 4.1	Control system design framework for morphing UAV . . .	64
Figure 4.2	Closed-loop interconnection structure of the longitudinal CAS.	67
Figure 4.3	Bode magnitude plot of the normal acceleration CAS. . .	71
Figure 4.4	Step response of the normal acceleration CAS.	72
Figure 4.5	Closed-loop interconnection of the lateral-directional CAS.	74
Figure 4.6	Bode magnitude plot of the lateral-directional CAS - angle of sideslip.	77
Figure 4.7	Bode magnitude plot of the lateral-directional CAS - roll rate.	78
Figure 4.8	State response to the angle of sideslip step command. . .	79
Figure 4.9	Input response to the angle of sideslip step command. . .	80
Figure 4.10	State response to the roll rate step command.	81
Figure 4.11	Input response to the roll rate step command.	82
Figure 4.12	GTM flight dynamics simulator.	87
Figure 4.13	Building blocks of GTM.	88
Figure 4.14	Flight trajectory of the push-over and pull-up - LPV. . .	90
Figure 4.15	Controlled states and symmetric morphing parameter history for the push-over and pull-up - LPV.	91
Figure 4.16	State history for the push-over and pull-up - LPV. . . .	92
Figure 4.17	Input history of the push-over and pull-up - LPV.	93
Figure 4.18	Flight trajectory of the push-over and pull-up - \mathcal{H}_∞ . . .	94

Figure 4.19	Controlled states and symmetric morphing parameter history for the push-over and pull-up - \mathcal{H}_∞	95
Figure 4.20	State history for the push-over and pull-up - \mathcal{H}_∞	96
Figure 4.21	Input history of the push-over and pull-up - \mathcal{H}_∞	97
Figure 4.22	Flight trajectory of the high-g turn (top view) - LPV.	98
Figure 4.23	Flight trajectory of the high-g turn (side view) - LPV.	99
Figure 4.24	Controlled states and symmetric morphing parameter history for the high-g turn - LPV.	100
Figure 4.25	State history of the high-g turn - LPV.	101
Figure 4.26	Input history of the high-g turn - LPV.	102
Figure 4.27	Flight trajectory of the high-g turn (top view) - \mathcal{H}_∞	103
Figure 4.28	Flight trajectory of the high-g turn (side view) - \mathcal{H}_∞	104
Figure 4.29	Controlled states and symmetric morphing parameter history for the high-g turn - \mathcal{H}_∞	105
Figure 4.30	State history of the high-g turn - \mathcal{H}_∞	106
Figure 4.31	Input history of the high-g turn - \mathcal{H}_∞	107
Figure 5.1	Closed-loop interconnection of the longitudinal autopilot	112
Figure 5.2	Bode magnitude plot for the longitudinal autopilot - true airspeed.	115
Figure 5.3	Bode magnitude plot for the longitudinal autopilot - al- titude.	116
Figure 5.4	State response to the true airspeed step command.	117
Figure 5.5	Input response to the true airspeed step command.	118
Figure 5.6	State response to the altitude step command.	119
Figure 5.7	Input response to the altitude step command.	120

Figure 5.8	Closed-loop interconnection of the lateral-directional autopilot.	122
Figure 5.9	Bode magnitude plot for the lateral-directional autopilot - angle of sideslip.	125
Figure 5.10	Bode magnitude plot for the lateral-directional autopilot - roll angle.	126
Figure 5.11	State response to the angle of sideslip step command. . .	127
Figure 5.12	Input response to the angle of sideslip step command. . .	128
Figure 5.13	State response to the roll angle step command.	129
Figure 5.14	Input response to the roll angle step command.	130
Figure 5.15	Flight trajectory of the waypoint-following flight.	133
Figure 5.16	State history of the waypoint-following flight.	134
Figure 5.17	Input history of the waypoint-following flight.	135
Figure 5.18	Flight trajectory of the circular trajectory-following flight.	136
Figure 5.19	State history of the circular trajectory-following flight. .	137
Figure 5.20	Input history of the circular trajectory-following flight. .	138
Figure 5.21	Flight trajectory of the helical ascent.	140
Figure 5.22	State history of the helical ascent.	141
Figure 5.23	Input history of the helical ascent.	142
Figure 5.24	Flight trajectory of the helical descent.	143
Figure 5.25	State history of the helical descent.	144
Figure 5.26	Input history of the helical descent.	145

Chapter 1

Introduction

1.1 Background and Motivation

A morphing unmanned aerial vehicle (UAV) is an advanced aerial platform capable of in-flight, controlled, large-scale shape transformations to improve efficiency, adaptability, and performance in various flight conditions and missions. As the complexity of modern UAV missions increases, it is difficult for the fixed-shape aircraft to effectively and efficiently accomplish the given missions. As a result, the need for versatile morphing aircraft has been gradually increased. Since the first manned flight, aircraft designers have always been attracted by the concept of variable-geometry aircraft, and several aircraft are capable of transforming their external shape within a limited extent [1]. In the past, the morphing capability was limited to altering flight characteristics by changing shape. However, recent developments in materials, sensors, and actuators have aroused interest in the development of morphing aircraft [2]. Usually, the development process involves complicated trade-off analyses and multidisciplinary optimization. In addition, morphing for direct flight control is made possible by effective actuator drive systems. As various concepts of the morphing aircraft appear, the need for techniques to effectively control the morphing aircraft is

emerging [3]. However, the control system design frameworks proposed so far still fails to fully utilize the benefits of morphing in every possible aspect.

Conventional fixed-wing aircraft are designed for optimal flight performance within the intended flight conditions and specified missions, which significantly sacrifices performance for other regimes. In contrast, the ability to change the configuration enables the morphing aircraft to fly nearly optimally in a wider range of the flight conditions. Especially, morphing wings can be utilized to generate aerodynamic control forces by directly controlling the airflow around a vehicle. This additional degree of freedom can be used i) to accomplish a normally impossible movement with conventional control surfaces alone, ii) to increase agility and maneuverability when paired with conventional control surfaces, iii) or to partially replace conventional control surfaces in the case of actuator failure. During the flight, morphing configurations can be optimized in real-time to maximize system-level benefits such as maneuverability, energy saving, survivability, etc. Numerous studies have been conducted on the advantages of morphing, but a few studies have been conducted on the control system that enables its full utilization.

Two main reasons make it difficult to use morphing parameters as control inputs in the control system design of the morphing aircraft. First, conventional control surfaces apply minimal aerodynamic forces and use long moment arms to generate control torque for the roll, pitch, and yaw axes. However, wing morphing often generates forces and moments simultaneously on multiple axes. In addition, there is usually significant nonlinearity between the morphing parameters and the generated aerodynamic forces and torques. In large-scale shape change, the position of the center of mass (CM), moment of inertia (MOI),

and the product of inertia (POI) can also change significantly. Second, the dynamic response of most morphing actuators are slow to the command compared to the traditional hydraulically-actuated control surfaces. The low bandwidth of morphing actuators may significantly degrade the overall performance of the control systems. Therefore, bandwidth gap should be carefully considered when using the morphing parameters as control inputs.

If the morphing parameters are considered as exogenous parameters, the designed controller should be able to change its characteristics according to the changing morphing parameters. Since the dynamic characteristics change significantly depending on the morphing shape, it is generally difficult to ensure a sufficient level of stability and performance with a fixed controller. For example, control systems with traditional gain scheduling techniques cannot guarantee the closed-loop stability when the scheduling parameter changes rapidly. In addition, interpolation or blending between point controllers involves a trial-and-error procedure with little theoretical guidance. Furthermore, in the region of transition between the design points, the robustness and performance guarantees of specific operating points are lost. Assuming that the parameters change slowly hinders the fundamental advantages of morphing.

Historically, gain scheduling has been a prevalent design technique for flight control system design of nonlinear system. Recently, a gain self-scheduled linear parameter-varying (LPV) control method has been attracting attention as a control method suitable for morphing aircraft. Therefore, the majority of the initial studies employing the LPV architecture were associated with flight control systems. The LPV framework allows the flight controller for the morphing aircraft to be designed with theoretical guarantees of robustness and perfor-

mance across a broad range of operating conditions and configurations. The nonlinearity of the plant can also be properly addressed by incorporating the nonlinearity into the scheduling parameters. Different bandwidths of the actuators can be considered in the design process because the LPV framework shares the basic control interconnection structure with a standard multivariable controller such as \mathcal{H}_∞ controller. In addition, the stability guarantee for arbitrary parameter changes opens the way to freely use the morphing parameters without any problems compromising stability.

In this dissertation, a high-fidelity asymmetric variable-span morphing aircraft model is obtained using the damage model data of the baseline NASA generic transport model (GTM) [4]. The linear time-invariant (LTI) models of the longitudinal and lateral-directional dynamics are obtained by linearizing the nonlinear model throughout the entire flight conditions and morphing shapes. The LPV models are obtained by parameterizing the family of the point-wise LTI models through interpolation. The symmetric component of the span variation is considered as a scheduling parameter along with airspeed and altitude, and the asymmetric component is considered as a lateral-directional axis control input along with the ailerons and rudders. The control augmentation systems (CAS) and autopilots are designed for manual and automatic flights, respectively. The symmetric morphing parameters are utilized to assist the morphing aircraft in achieving the commanded maneuver and enhancing the flight performance over the different flight conditions, while the asymmetric morphing parameter is used as an additional control input of the lateral-directional axis. Through numerical simulation of various maneuvers, it is shown that the maneuverability of the morphing aircraft can be enhanced by appropriately changing

the symmetric morphing parameter. In addition, it is shown that the proposed control system successfully follows the flight trajectory even under rapid variation of flight conditions and extremely fast morphing, while the baseline \mathcal{H}_∞ controller with the same parameter setting quickly loses closed-loop stability.

1.2 Literature Review

In this section, a literature review of existing studies on the subject covered in this dissertation is conducted. First, studies on applying morphing wing technology to fixed-wing aircraft are reviewed. Second, control system design methods applied to the flight control of morphing aircraft are reviewed. Finally, studies on which LPV control techniques are applied to aerospace systems are reviewed.

1.2.1 Fixed-Wing Aircraft Implementing Morphing Technologies

Wright's Flyer, the first powered airplane, can be considered as a morphing aircraft in the form of controlling because it deforms wings without a separate control surface [5]. After that, various types of variable-geometry aircraft have been developed until the 1980s, mainly for military purposes. Then, from the 1990s, modern morphing aircraft began to appear, and morphing technology has recently been applied to small unmanned aerial vehicles [6–12]. This trend is mainly due to the development of new materials, actuators, and sensors, and the fact that modern tasks that should be executed by the aircraft are significantly different from those of the past [13]. The impact of morphing wings on aircraft performance was examined in [14], where several morphing strategies were provided and compared. Early examples of morphing aircraft utilized shape memory alloy (SMA) for continuous flap deflection [15–18]. Now, there are many examples where the advanced material is used for wing skin [19–29]. In the majority of cases, additional actuators are installed under the skin where the skin is used in a passive manner. The flight dynamics of morphing aircraft

have been also extensively studied [30–42].

1.2.2 Flight Control of Morphing Aircraft

Various linear control methods have been applied to control of morphing aircraft, including proportional-integral-derivative (PID) control [43, 44], and \mathcal{H}_∞ control [45–47]. Many studies adopted a gain scheduling technique [43, 44, 48–52] or switching methods [45, 50, 53–60]. Learning-based or data-driven approaches (reinforcement learning, neural network-based adaptive control) [53, 55, 61–67] to consider the time-varying nature of morphing aircraft, robust approaches [43, 44, 46, 48, 49, 68–75] and adaptive approaches [46, 60, 62, 64, 69, 76–86] were also adopted. Control allocation methods were adopted to deal with an over-actuated model of morphing aircraft obtained as a result of incorporating morphing parameters into control inputs [87, 88]. Various nonlinear control methods have also been applied, which include sliding mode control [60, 81, 84, 89–93], nonlinear dynamic inversion [94, 95] with indirect adaptation mechanism [96], backstepping control [79, 97–99], and disturbance observer-based control [98, 100, 101]. LPV and robust control methods are also extensively applied [44, 46, 48–50, 52, 56, 59, 90, 91, 102, 103].

1.2.3 Gain Scheduling Approaches to Controller Design

Classical gain scheduling techniques have been widely adopted for the system with wide range of operation. LTI-based methods such as classical control, loop-shaping, \mathcal{H}_2 (LQG) optimal control, \mathcal{H}_∞ suboptimal control, mixed-sensitivity control, mu-synthesis can be applied. Many LPV techniques such as switching LPV control, model predictive control based on LPV model, data-

driven strategies, and LPV control with scheduling uncertain parameters were applied to aerospace domain problems [59, 81, 104–123]. Fuzzy gain scheduling techniques were also studied [124, 125].

1.3 Objectives and Contributions

1.3.1 Objectives

The objective of this dissertation is to develop a control system that can fully exploit the shape-changing ability while rigorously satisfying all the stability requirements at the same time.

1.3.2 Contributions

The contribution of this dissertation can be divided into three parts. First, a high-fidelity model of asymmetric variable-span morphing UAV is developed. Second, the control augmentation system is designed based on LPV methods which exploit variable span morphing parameters as both control input and scheduling parameters. Finally, autopilot is designed based on LPV methods where a morphing configuration determination logic is implemented.

Development and Analysis of a Morphing Aircraft Model

A high-fidelity model of asymmetric variable-span morphing UAV is developed, where nonlinear and LPV models of morphing aircraft are derived. A nominal model is first presented, and the morphing model is derived from the damage model. Trim condition is investigated, and point-wise LTI model is obtained through Jacobian linearization. LPV model is constructed by introducing scheduling parameters, and the constructed LPV model is analyzed in the frequency domain and time domain to obtain physical insight for the design of controller.

Design of Gain Self-Scheduled Flight Control System

The control augmentation system is designed based on LPV methods which exploit variable span morphing parameters as control input and scheduling parameters. A control augmentation system is designed for the morphing-assisted maneuvers of morphing UAVs based on LPV methods. A normal acceleration CAS is designed for the control of longitudinal motion, and a roll rate CAS is designed for the control of lateral-directional motion. The CAS utilizes symmetric and asymmetric morphing for improved agility and maneuverability, respectively. Numerical simulation for push-over and pull-up maneuvers and high-g turn is performed to demonstrate the effectiveness of the proposed scheme.

Morphing Strategy

An autopilot is designed for a morphing-assisted flight of morphing UAVs based on LPV methods. Airspeed and altitude autopilots are designed for the control of longitudinal motion. Roll angle autopilot is designed for the control of lateral-directional motion. The autopilot utilizes symmetric and asymmetric morphing for improved agility and maneuverability, respectively. Numerical simulations for waypoint following flight and orbit following flight are performed to demonstrate the effectiveness of the proposed scheme.

1.4 Dissertation Outline

The organization of this dissertation is as follows. In Chap. 2, mathematical preliminaries are summarized. In Chap. 3, the LPV model of morphing aircraft is derived. In Chap. 4, LPV-based CAS is designed, and in Chap. 5, LPV-based autopilot is designed. In Chap. 6, the summary of the main results of this dissertation and suggestions for future work are provided.

Chapter 2

Mathematical Preliminaries

In this chapter, mathematical preliminaries for LPV system modeling, analysis, and controller synthesis are presented. LPV control synthesis is a technique to design a control system that provides gain-scheduled controllers with a strict stability guarantee and performance characteristics. Real-time parameter information is used for scheduling by the controller. In contrast to the conventional gain scheduling approaches, the LPV control structure incorporates the time-varying nature of the associated LPV dynamics. *A priori* stability and desired performance assurances reduce the need for extensive simulations to validate the stability and performance attributes.

At the price of conservatism, one of the primary benefits of LPV control synthesis is the existence of a sound theoretical framework assuring *a priori* stability and performance for all parameters within a corresponding domain. In addition, the design of the associated controller is global with regard to the parameterized operating envelope, and the controller is directly synthesized as opposed to being constructed from a family of local linear controllers. While the LPV control synthesis prioritizes a linear model above a nonlinear model of the plant, the final controller is often nonlinear. The control synthesis is closely connected to linear multi-variable control techniques due to the fact

that LPV synthesis utilizes the induced L_2 -norm as a performance metric. As a drawback, the controller synthesis is much more complex, and in most cases, conservatism is required to arrive at a practical and convex problem. Note that an LPV representation of a nonlinear system is not unique. For all parameter values, it is preferable to have an LPV description that is close to the nonlinear system. The more conservatism is imposed during the LPV controller synthesis process if the discrepancy between the LPV model and the nonlinear model is significant.

2.1 LPV Systems

2.1.1 Taxonomy of Dynamical Systems

The objective of a mathematical representation of the nonlinear flight dynamics is to generate models that adequately capture aircraft behavior, which are applicable for systematic control design. The state-space representation is a mathematical model of a dynamical system with the input, output, and state variables composed of first-order ordinary differential equations (ODEs). Continuous-time dynamical systems described by nonlinear ODEs can be classified into a few categories according to explicit dependency on time and the scheduling parameter. The nonlinear systems can be further refined depending on the input affinity. If the system becomes linear, LTV, LTI, and LPV systems can be defined. Note that the LPV system differs from the LTV system in that the parameters are not known in advance. A taxonomy of dynamics model classifications is shown in Fig. 2.1.

2.1.2 Definition of LPV Systems

LPV systems can be defined as linear systems whose system matrices are known functions of time-varying parameters. The time variations of parameters are assumed to be measurable but unknown *a priori*. Therefore, in the LPV controller synthesis procedure, the parameters are regarded as free variable parameters with arbitrary values in the region, and the LPV system description will differ from that of the nonlinear system. More conservatism is introduced during the LPV modeling step, the greater the disparity from the nonlinear model. LPV descriptions of nonlinear systems are not unique, and it is preferable to have an LPV description that is close to the nonlinear system for all

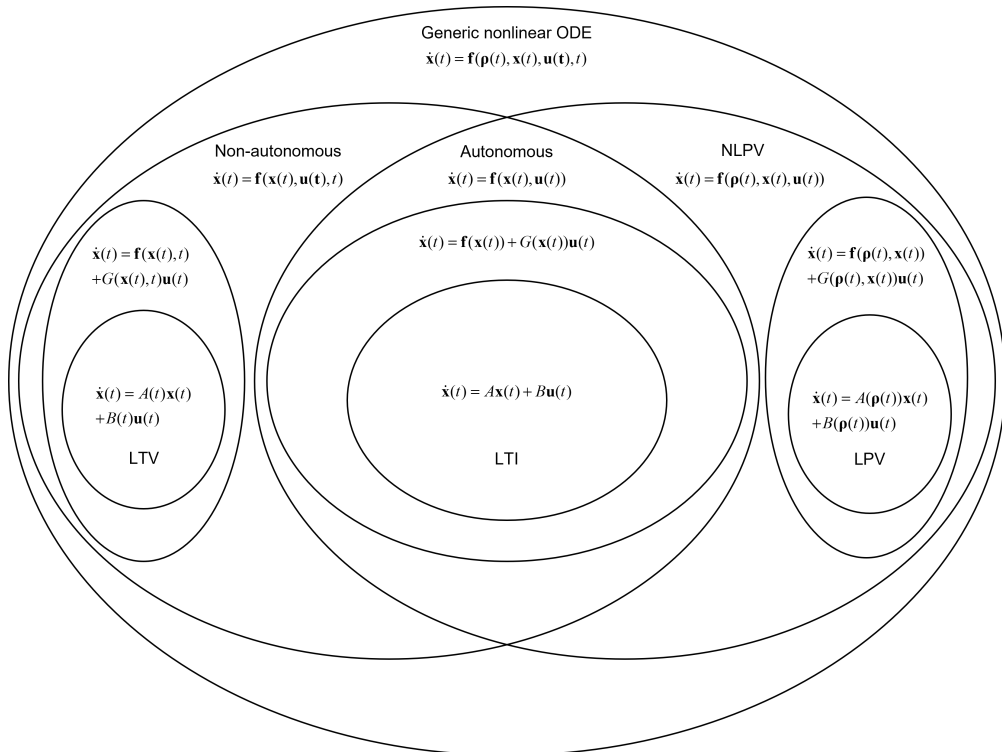


Figure 2.1 Taxonomy of dynamical systems

parameter values. LPV systems are characterized by linear differential equations with potentially nonlinear data dependencies on time-varying parameters. The objective of LPV synthesis is to generate a controller with the same structure so that the entire controlled system satisfies specified stability and performance requirements across the entire range of permissible parameter trajectories. In order to improve performance over robust controllers, which lack adaptability, LPV controllers utilize online measurements of time-varying parameters. LPV control techniques are viewed as an alternative to conventional gain-scheduling approaches for nonlinear systems due to the fact that time-varying parameters frequently provide an interpretation of the system's operational point. The resultant LPV controllers are automatically gain-scheduled and do not require *ad hoc* techniques for interpolating gains, which is a distinct advantage of LPV control theory over conventional gain-scheduled control. LPV synthesis makes use of the computational capacity of existing convex optimization tools to ensure stability, performance, and resilience, which are frequently difficult to achieve with conventional design methods.

The following definition describes the set of all admissible parameter trajectories, which guarantees the existence and uniqueness of the solution to the differential equation governing an LPV system.

Definition 2.1. (*Parameter Variation Set*) Given a compact set $\mathcal{P} \subset \mathbb{R}^{n_p}$, the parameter variation set is defined as

$$\mathcal{F}_{\mathcal{P}} \triangleq \{\boldsymbol{\rho}(t) \in C^0 : \boldsymbol{\rho} \in \mathcal{P}\} \quad (2.1)$$

where C_0 stands for the class of piecewise continuous functions.

Assuming that the parameter can vary arbitrarily fast and using a sin-

gle Lyapunov function (SLF) may lead to conservative controller synthesis. A parameter-dependent Lyapunov function (PDLF) method based on the rate-bounded parameter can be used to obtain a less conservative result or to find a stabilizing solution for a problem that cannot be solved with a rate-unbounded method. Practically, the bounded parameter variation rate assumption is also valid for a wide range of applications in the field of aerospace engineering. A rate-bounded parameter variation set is described as follows.

Definition 2.2. (*Rate-bounded Parameter Variation Set*) Given a compact set $\mathcal{P} \subset \mathbb{R}^{n_\rho}$ and finite non-negative numbers $\{\nu\}_{i=1}^{n_\rho}$, the rate-bounded parameter variation set is defined as

$$\mathcal{F}_\mathcal{P}^\nu \triangleq \{\boldsymbol{\rho}(t) \in C^1 : \boldsymbol{\rho} \in \mathcal{P}, |\dot{\rho}_i| \leq \nu_i, i = 1, \dots, n_\rho\} \quad (2.2)$$

where C_1 stands for the class of piecewise continuously differentiable functions.

A generic rate-bounded open-loop LPV system is described as follows.

Definition 2.3. (*Open-loop LPV System*) Given a compact set $\mathcal{P} \subset \mathbb{R}^{n_\rho}$ and finite non-negative numbers $\{\nu\}_{i=1}^{n_\rho}$, the rate-bounded parameter open-loop LPV system is defined as

$$\begin{bmatrix} \dot{\mathbf{x}} \\ \mathbf{u} \end{bmatrix} = \begin{bmatrix} A(\boldsymbol{\rho}) & B(\boldsymbol{\rho}) \\ C(\boldsymbol{\rho}) & D(\boldsymbol{\rho}) \end{bmatrix} \begin{bmatrix} \mathbf{x} \\ \mathbf{y} \end{bmatrix} \quad (2.3)$$

where $\boldsymbol{\rho} \in \mathcal{F}_\mathcal{P}^\nu$ is the parameter, $\mathbf{x} \in \mathbb{R}^{n_x}$ is the state, $\mathbf{y} \in \mathbb{R}^{n_y}$ is the measurement, and $\mathbf{u} \in \mathbb{R}^{n_u}$ is the control input. All of the matrices are continuous functions with appropriate dimensions.

The LPV system can be augmented with a control objective by introducing additional weighted inputs and outputs, which form a generalized rate-bounded open-loop LPV system described as follows.

Definition 2.4. (*Generalized Open-loop LPV System*) Given a compact set $\mathcal{P} \subset \mathbb{R}^{n_\rho}$, a generalized rate-bounded open-loop LPV system is defined as

$$\begin{bmatrix} \dot{\mathbf{x}} \\ \mathbf{z} \\ \mathbf{y} \end{bmatrix} = \begin{bmatrix} A(\boldsymbol{\rho}) & B_1(\boldsymbol{\rho}) & B_2(\boldsymbol{\rho}) \\ C_1(\boldsymbol{\rho}) & D_{11}(\boldsymbol{\rho}) & D_{12}(\boldsymbol{\rho}) \\ C_2(\boldsymbol{\rho}) & D_{21}(\boldsymbol{\rho}) & D_{22}(\boldsymbol{\rho}) \end{bmatrix} \begin{bmatrix} \mathbf{x} \\ \mathbf{w} \\ \mathbf{u} \end{bmatrix} \quad (2.4)$$

where $\boldsymbol{\rho} \in \mathcal{F}_{\mathcal{P}}^{\nu}$, $\mathbf{z} \in \mathbb{R}^{n_z}$ is the performance output, and $\mathbf{w} \in \mathbb{R}^{n_w}$ is the external input. All of the matrices are continuous functions with appropriate dimensions.

For control design in the LPV framework, it is further assumed that i) the future trajectory of the parameter is not known in advance, and ii) the parameter is measurable in real-time. If the first assumption is omitted, the LPV system should be viewed as an LTV system. Then, predictive control approaches can be applied to exploit future information. If the second assumption is omitted, the LPV system should be viewed as an uncertain LTI system. Then, gain scheduling becomes impossible, and robust or adaptive control approaches can be applied to deal with the uncertainties.

Additional conservatism resulting from the choice of basis functions can be introduced in the case of rate-bounded design. However, the LPV model is still a collection of linear designs, and it is impossible to differentiate between real disturbances and normal manifestations of nonlinearity in each of these linear designs. Therefore, any further improvement in performance and robustness can only be accomplished by directly recognizing plant nonlinearity, as opposed to treating it as a nuisance in a linear model. Therefore, the nonlinear dynamics must be incorporated explicitly into the mathematical description but without excessive generalization.

2.1.3 LPV Modeling by Linearization

The goal of the LPV modeling process is to obtain an LPV model that mimics the following nonlinear system.

$$\dot{\mathbf{x}} = A(\boldsymbol{\rho})\mathbf{x} + B(\boldsymbol{\rho})\mathbf{u} \cong \mathbf{f}(\mathbf{x}, \mathbf{u}, \boldsymbol{\rho}) \quad (2.5)$$

$$\mathbf{y} = C(\boldsymbol{\rho})\mathbf{x} + D(\boldsymbol{\rho})\mathbf{u} \cong \mathbf{h}(\mathbf{x}, \mathbf{u}, \boldsymbol{\rho}) \quad (2.6)$$

where $\boldsymbol{\rho}$ is the parameter vector varying within a region that can be state-dependent. It is often assumed that parameter dependencies have clear structures, such as affine, polynomial, polytopic, or LFT dependencies. In numerous industrial contexts, a finite family of linear models is used to characterize the behavior of a system over its entire operational range. The linearized models characterize the behavior of the system near a particular operational point, and the collection is parameterized by physical parameters. Creating polynomial least squares fits of the state-space matrices in order to obtain a continuous parameterization of the operational envelope is rational if the state variables have physical significance.

Using the characteristics of the given trajectory (flight envelope) as quantifiable scheduling variables, the optimal LPV model can be obtained. Local validity is restricted to a parameterized family of linearized models derived from linearization-based scheduling or numerous black-box point designs. If an LPV model is constructed from such a collection of linearized models, the resulting linear parameter-dependent model's accuracy in comparison to the original nonlinear model or plant remains uncertain. Classical gain scheduling is primarily limited to stationary local controller synthesis. Although a nonlinear system can be linearized along a particular trajectory, gain scheduling

techniques expanding the stability zone using a family of linearizations along different trajectories do not exist yet.

Consequently, in the LPV controller synthesis process, the parameters are seen as free variable parameters taking arbitrary values in the domain, and the LPV description will differ from the nonlinear system. The greater this discrepancy, the more conservativeness is incorporated in the LPV controller synthesis stage. Note that LPV representations of nonlinear systems are not unique, and it is desired to have an LPV description that is close to the nonlinear system for all possible parameter values.

Jacobian Linearization

The traditional approach, which uses Jacobian linearization of a nonlinear system about specific operating points, is known as linearization-based scheduling. A parameterized set of LTI models that represent the original nonlinear model is produced when a suitable scheduling variable is chosen to parameterize the set of linear models.

Velocity-Based Linearization

Linearization-based scheduling techniques are limited to modeling on equilibrium points. It is possible to enable linearization at each operational point by using so-called velocity-based or off-equilibrium linearizations.

QLPV Representation

The concept behind quasi-LPV (QLPV) scheduling is to turn a nonlinear model into an LPV form while concealing the nonlinear elements by incorpo-

rating them into the scheduling variable. Due to the fact that this procedure includes a transformation rather than a linearization, the final LPV model is identical to the original nonlinear model.

SDC Parametrization

State-dependent coefficient (SDC) parameterization, also known as extended linearization, or apparent linearization, is the process of factorizing a nonlinear system into a linear-like structure that contains SDC matrices. The state-dependent Riccati equation (SDRE) control method utilizes the SDC matrices.

Fuzzy Linearization

The nonlinear plant dynamics can be represented as multiple blended models of the form

$$\dot{\mathbf{x}} = \sum_i \mathbf{f}_i(\mathbf{x}, \mathbf{u})\mu(\boldsymbol{\Phi}) \quad (2.7)$$

$$\mathbf{y} = \sum_i \mathbf{h}_i(\mathbf{x}, \mathbf{u})\mu(\boldsymbol{\Phi}) \quad (2.8)$$

where $\boldsymbol{\Phi}(\mathbf{x}, \mathbf{u})$ is the scheduling parameter and the blending weights satisfy

$$\sum_i \mu_i = 1, \quad \mu_i \geq 0 \quad (2.9)$$

The LPV model is represented as

$$\begin{bmatrix} \dot{\mathbf{x}} \\ \mathbf{y} \end{bmatrix} = S(\boldsymbol{\rho}) \begin{bmatrix} \mathbf{x} \\ \mathbf{u} \end{bmatrix} \quad (2.10)$$

where $\boldsymbol{\rho}$ is the scheduling parameter and

$$S(\boldsymbol{\rho}) = S_0 + \sum_i \rho_i S_i \quad (2.11)$$

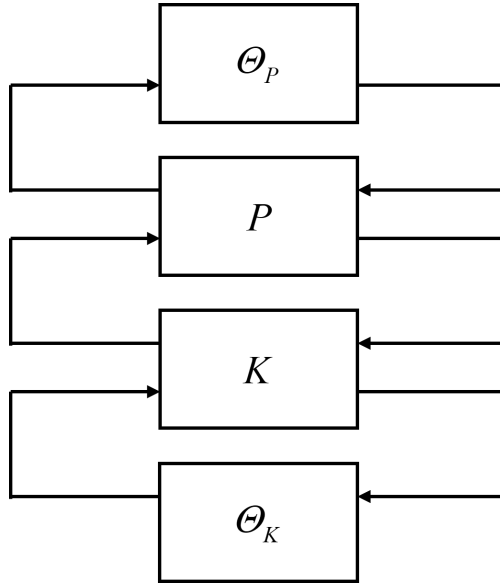


Figure 2.2 $P - \Theta$ structure of the LPV control system

Linearization by LFT techniques

The most common representation used in robust controller design is a model set based on linear fractional transformation (LFT). The scheduling variables serve the same purpose as the uncertainties in terms of analysis. In the LPV system, the parameter dependence can be represented as an LFT. This representation gives the LPV system a $P - \Theta$ structure as shown in Fig. 2.2. In Fig. 2.2 the parameter-varying or nonlinear terms are located in Θ , and the LTI terms are located in P . The LPV control system can be represented as shown in Fig. 2.3 by lower LFT. Creating the LFT form is equivalent to a realization problem and not necessarily unique or minimal.

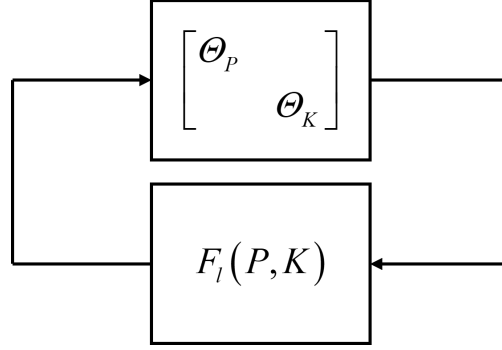


Figure 2.3 LFT representation of the LPV control system

2.2 Gain Self-Scheduled Induced \mathcal{L}_2 -Norm Control of LPV Systems

2.2.1 Norms of Signals and Systems

The p -norm of the vector \mathbf{x} is defined by

$$1 - norm : \|\mathbf{x}\|_1 = \sum_{i=1}^m |x_i| \quad \text{for } p = 1 \quad (2.12)$$

$$p - norm : \|\mathbf{x}\|_p = \left(\sum_{i=1}^m |x_i|^p \right)^{1/p} \quad \text{for } 1 < p < \infty \quad (2.13)$$

$$\infty - norm : \|\mathbf{x}\|_\infty = \max_{1 \leq i \leq m} |x_i| \quad \text{for } p = \infty \quad (2.14)$$

The p -norm of a signal $x(t)$ is defined by

$$1 - norm : \|x\|_1 = \int_{-\infty}^{\infty} |x(t)| dt \quad \text{for } p = 1 \quad (2.15)$$

$$p - norm : \|x\|_p = \left(\int_{-\infty}^{\infty} |x|^p dt \right)^{1/p} \quad \text{for } 1 < p < \infty \quad (2.16)$$

$$\infty - norm : \|x\|_\infty = \sup_{t \in \mathcal{R}} |x(t)| \quad \text{for } p = \infty \quad (2.17)$$

The p-norm of a vector-valued signal $\mathbf{x}(t)$ is defined by

$$\mathcal{L}_p - norm : \quad \|\mathbf{x}\|_p = \left(\int_{-\infty}^{\infty} \sum_{i=1}^m |x_i|^p dt \right)^{1/p} \quad \text{for } 1 < p < \infty \quad (2.18)$$

$$\mathcal{L}_\infty - norm : \quad \|\mathbf{x}\|_\infty = \sup_{t \in \mathcal{R}} |\mathbf{x}(t)| \quad \text{for } p = \infty \quad (2.19)$$

For a linear, time-invariant, stable system \mathcal{G} , ∞ -norm, or the induced 2-norm, is given by

$$\|\mathcal{G}\|_\infty = \sup_{\omega \in \mathcal{R}} \|G(j\omega)\|_2 \quad (2.20)$$

\mathcal{L}_2 -norm can be defined as a number γ which is the minimum positive number satisfying

$$\|\mathbf{y}\|_2 < \gamma \|\mathbf{u}\|_2 + \beta \quad (2.21)$$

\mathcal{L}_2 is a Hilbert space consists of all complex matrix functions F such that

$$\int_{-\infty}^{\infty} \text{trace}[F^*(j\omega)F(j\omega)]d\omega < \infty \quad (2.22)$$

\mathcal{H}_2 is a closed subspace of \mathcal{L}_2 with functions that are analytic in the open right-half plane (RHP). \mathcal{L}_∞ is a Banach space consisting of all bounded complex matrix functions F with the norm

$$\|F\|_\infty = \text{ess sup}_{\omega \in \mathcal{R}} \bar{\sigma}[F(j\omega)] \quad (2.23)$$

\mathcal{H}_∞ is a closed subspace of \mathcal{L}_∞ with functions that are analytic in the open RHP.

2.2.2 Analysis of LPV Systems

The LPV controller is defined as follows.

Definition 2.5. (*LPV Controller*) Given a compact set $\mathcal{P} \subset \mathbb{R}^{n_\rho}$, a rate-dependent LPV dynamic output-feedback controller $K_{\mathcal{P}}^{\nu}$ is defined as:

$$\begin{bmatrix} \dot{\mathbf{x}}_k \\ \mathbf{u} \end{bmatrix} = \begin{bmatrix} A_k(\boldsymbol{\rho}, \dot{\boldsymbol{\rho}}) & B_k(\boldsymbol{\rho}, \dot{\boldsymbol{\rho}}) \\ C_k(\boldsymbol{\rho}, \dot{\boldsymbol{\rho}}) & D_k(\boldsymbol{\rho}, \dot{\boldsymbol{\rho}}) \end{bmatrix} \begin{bmatrix} \mathbf{x}_k \\ \mathbf{y} \end{bmatrix} \quad (2.24)$$

where $\boldsymbol{\rho} \in \mathcal{F}_{\mathcal{P}}^{\nu}$ and $\mathbf{x}_k \in \mathbb{R}^{n_k}$ is the controller state. All of the matrices are continuous functions with appropriate dimensions.

Let us define a closed-loop state $x_{cl} \triangleq [x^T x_k^T]^T$. Then, a closed-loop LPV system $\Sigma_{\mathcal{P}}$ is given by

$$\begin{bmatrix} \dot{x}_{cl} \\ z \end{bmatrix} = \begin{bmatrix} A_{cl}(\boldsymbol{\rho}, \dot{\boldsymbol{\rho}}) & B_{cl}(\boldsymbol{\rho}, \dot{\boldsymbol{\rho}}) \\ C_{cl}(\boldsymbol{\rho}, \dot{\boldsymbol{\rho}}) & D_{cl}(\boldsymbol{\rho}, \dot{\boldsymbol{\rho}}) \end{bmatrix} \begin{bmatrix} x_{cl} \\ w \end{bmatrix} \quad (2.25)$$

where

$$A_{cl} \triangleq \begin{bmatrix} A + B_2 D_k C_2 & B_2 C_k \\ B_k C_2 & A_k \end{bmatrix} \quad (2.26)$$

$$B_{cl} \triangleq \begin{bmatrix} B_1 + B_2 D_{21} \\ B_k D_{21} \end{bmatrix} \quad (2.27)$$

$$C_{cl} \triangleq \begin{bmatrix} C_1 + D_{12} D_k C_2 & D_{12} C_k \end{bmatrix} \quad (2.28)$$

$$D_{cl} \triangleq D_{11} + D_{12} D_k D_{21} \quad (2.29)$$

The controller should be designed so that parameter-dependent stability is guaranteed. An LPV system $\Sigma_{\mathcal{P}}$ given in Eq. (2.25) is said to be parameter-dependent stable if the function A_{cl} is parameter-dependent stable. Parameter-dependent stability of the function A_{cl} is defined as follows [126].

Theorem 2.1. (*Parameter-Dependent Stability*) Given a compact set $\mathcal{P} \subset \mathbb{R}^{n_\rho}$, finite non-negative numbers $\{\nu\}_{i=1}^{n_\rho}$, and a function $A(\boldsymbol{\rho}, \beta) \in C^0 : \mathbb{R}^{n_\rho} \times$

$\mathbb{R}^{n_\rho} \rightarrow \mathbb{R}^{n_x \times n_x}$, the function A is parameter-dependent stable over \mathcal{P} if there exists a function $P(\boldsymbol{\rho}) \in C^1 : \mathbb{R}^{n_\rho} \rightarrow \mathbb{R}^{n_x \times n_x}$ such that $P(\boldsymbol{\rho}) > 0$ and

$$A^T(\boldsymbol{\rho}, \beta)P(\boldsymbol{\rho}) + P(\boldsymbol{\rho})A(\boldsymbol{\rho}, \beta) + \sum_{i=1}^{n_\rho} \left(\beta_i \frac{\partial P}{\partial \rho_i} \right) < 0 \quad (2.30)$$

for all $\boldsymbol{\rho} \in \mathcal{P}$ and $|\beta_i| \leq \nu_i, i = 1, \dots, n_\rho$.

In this study, an induced \mathcal{L}_2 -norm of the closed-loop system is considered, which should be optimized while guaranteeing parameter-dependent stability. Before the induced \mathcal{L}_2 -norm is defined, a state transition matrix and a causal linear operator are defined as follows.

Definition 2.6. (*State Transition Matrix*) $\Phi_\rho(t, t_0)$ is the state transition matrix of the undriven system $\dot{\mathbf{x}}_{cl}(t) = A_{cl}(\boldsymbol{\rho}, \dot{\boldsymbol{\rho}})\mathbf{x}_{cl}(t)$ such that

$$\mathbf{x}_{cl}(t)\Phi_\rho(t, t_0) = \mathbf{x}_{cl}(t_0) \quad (2.31)$$

Definition 2.7. (*Causal Linear Operator*) For $\mathbf{x}(t_0) = \mathbf{0}$, the LPV system $\Sigma_{\mathcal{P}}$ given in Eq. (2.25) generates a causal linear operator $G_\rho : L_{2,e}^{n_d} \rightarrow L_{2,e}^{n_z}$, which is given by

$$\mathbf{z}(t) = \int_{t_0}^t C_{cl}(\boldsymbol{\rho}, \dot{\boldsymbol{\rho}})\Phi_\rho(t, \tau)B_{cl}(\boldsymbol{\rho}, \dot{\boldsymbol{\rho}})d\tau + D_{cl}(\boldsymbol{\rho}, \dot{\boldsymbol{\rho}})d(t) \quad (2.32)$$

and the set of causal linear operators described by the LPV system $\Sigma_{\mathcal{P}}$ given in Eq. (2.25) is denoted as

$$G_{\mathcal{F}_{\mathcal{P}}^\nu} \triangleq \{G_\rho : \boldsymbol{\rho} \in \mathcal{F}_{\mathcal{P}}^\nu\} \quad (2.33)$$

The induced \mathcal{L}_2 -norm represents a ratio from the external input to the performance output. An induced \mathcal{L}_2 -norm is defined as follows.

Definition 2.8. (*Induced \mathcal{L}_2 -norm*) Given a parameter-dependent stable LPV system $\Sigma_{\mathcal{P}}$ given in Eq. (2.25), for a zero initial condition $\mathbf{x}(t_0) = \mathbf{0}$, the induced \mathcal{L}_2 -norm is defined as

$$\|G_{\mathcal{F}_{\mathcal{P}}}\|_{2 \rightarrow 2} = \sup_{\rho \in \mathcal{P}} \sup_{\|\mathbf{w}\| \neq 0, \mathbf{w} \in \mathcal{L}_2} \frac{\|\mathbf{z}\|_2}{\|\mathbf{w}\|_2} \quad (2.34)$$

Figures 2.4-2.7 show the structure of the open-loop LPV plant, generalized open-loop LPV plant, closed-loop LPV control system, and LFT representation of the closed-loop LPV control system.

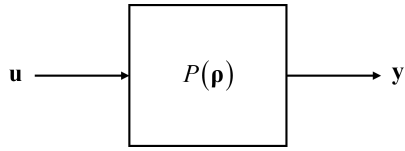


Figure 2.4 Open-loop LPV plant

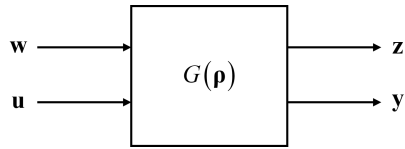


Figure 2.5 Generalized open-loop LPV plant

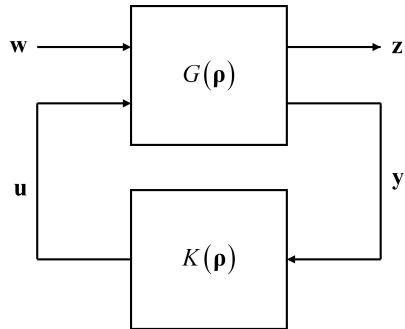


Figure 2.6 Closed-loop LPV control system

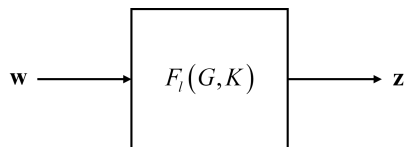


Figure 2.7 LFT representation of the closed-loop LPV control system

2.2.3 LPV Controller Design

The LMI approach is based on the generalized scaled bounded real lemma, which is formalized as follows [126].

Theorem 2.2. (*Generalized Scaled Bounded Real Lemma*) *Given a compact set $\mathcal{P} \subset \mathbb{R}^{n_\rho}$, finite non-negative numbers $\{\nu\}_{i=1}^{n_\rho}$, and an LPV system, if there exists a function $P(\boldsymbol{\rho}) \in C^1 : \mathbb{R}^{n_\rho} \rightarrow \mathbb{R}^{(n_x+n_k) \times (n_x+n_k)}$ such that $P(\boldsymbol{\rho}) > 0$ and*

$$\begin{bmatrix} R(\rho, \beta) & XB_{cl}(\boldsymbol{\rho}) & C_{cl}^T(\boldsymbol{\rho}) \\ B_{cl}^T(\boldsymbol{\rho})X & -\gamma I_{n_w} & D_{cl}^T(\boldsymbol{\rho}) \\ C_{cl}^T(\boldsymbol{\rho}) & D_{cl}(\boldsymbol{\rho}) & -\gamma I_{n_z} \end{bmatrix} < 0 \quad (2.35)$$

where

$$R(\boldsymbol{\rho}, \beta) = A_{cl}^T(\boldsymbol{\rho}, \beta)P(\boldsymbol{\rho}) + P(\boldsymbol{\rho})A_{cl}(\boldsymbol{\rho}, \beta) + \sum_{i=1}^{n_\rho} \left(\beta_i \frac{\partial P}{\partial \rho_i} \right) \quad (2.36)$$

is satisfied for all $\boldsymbol{\rho} \in \mathcal{P}$ and $|\beta_i| \leq \nu_i$, $i = 1, \dots, n_\rho$, then the function A_{cl} is parameter-dependent stable over \mathcal{P} and there exists a scalar δ with $0 \leq \delta < \gamma$ such that $\|G_{\mathcal{F}_\rho^\nu}\|_{2 \rightarrow 2} \leq \delta$.

The above theorem formulates a sufficient condition for the performance index γ .

2.2.4 Software for Synthesis and Analysis

The LPV control techniques share the same roots as multi-variable robust control techniques. Therefore, the MATLAB-based software for the LPV framework makes use of the Robust Control Toolbox's data structure and control synthesis and analysis algorithms [127, 128].

LPVTools

LPVTools is a framework for modeling, analysis, and synthesis for the linear parameter-varying systems [127]. Once the open-loop plant is augmented with the performance specifications and the generalized plant is constructed, the optimization problem of LPV controller synthesis is transformed into a convex feasibility problem with infinite constraints imposed on the linear matrix inequality (LMI) formulation. The infinite-dimensional problem can be approximated with a finite-dimensional problem by gridding the scheduling parameter domain. The LMI problem can be solved using off-the-shelf LMI optimization solvers. The complexity of the LPV analysis problem is approximately $O(n_r 2^{n_\rho} (n_x + n_u + n_y) (n_b n_x^2)^3)$ in case of rate-bounded design and $O(n_r (n_x + n_u + n_y) n_x^6)$ in case of rate-unbounded design where n_r is the number of grid points, n_ρ is the number of scheduling parameters, n_x is the number of states, n_u is the number of inputs, n_y is the number of outputs, and n_b is the number of basis functions [127]. Note that the complexity exponentially grows as the number of scheduling parameters increases. In general, the computation load of the rate-bounded synthesis is much greater than the rate-unbounded design. Even though the rate-bounded design is much less conservative, the rate-bounded synthesis problem is more difficult to solve. Furthermore, the synthesis results depend on the selection of the basis functions. The fact that there is no systematic way to construct the set of basis functions makes the design procedure more challenging. Therefore, the rate-unbounded design often becomes a more practical choice unless it is inevitable to consider the rate bounds to obtain a feasible solution.

LPVcore

LPVcore is a complimentary MATLAB toolbox for LPV framework users [128]. LPVcore employs innovative techniques for LPV system identification and control synthesis. LPVcore is an open-source MATLAB toolbox for LPV system modeling, identification, and control. The linear connection between inputs and outputs in LPV systems is disrupted by a measurable, time-varying signal known as the scheduling signal. These distinctions enable LPV devices to record events that are nonlinear and time-varying. The LPV framework is composed of algorithms for modeling, analyzing, identifying, and controlling. The European Research Council finances the Eindhoven University of Technology and Drebble's APROCS project for the development and upkeep of LPVcore [128].

Chapter 3

Asymmetric Variable-Span Morphing UAV Model

In this study, the NASA GTM as shown in Fig. 3.1 is selected as the baseline model for the development of a morphing UAV model. The GTM simulation software is available under the NASA open-source agreement [4]. GTM's high-fidelity models of dynamics, aerodynamics, sensors and actuators are ideal not only for analyzing the impacts of morphing in flight but also for demonstrating that the suggested technique can attain the intended performance in a real system.

In the GTM, six damage cases are included, and therefore a nonlinear variable-span morphing model can be derived for the case in which 25% of the left wing tip is lost. The effects due to variable-span morphing can be modeled by assuming that the wingtips can telescope continuously instead of being lost. Thus, mass, the CM, MOI, POI, and aerodynamic coefficients become dependent on morphing parameters. By linearizing the acquired nonlinear parameter variation model of the morphing UAV at each operational point, it is possible to generate LTI models that decouple longitudinal and lateral-directional motions. By studying the LTI model in the time and frequency domains, it is possible to get the knowledge required for controller design. The LPV model



Figure 3.1 NASA GTM-T2.

can be constructed by applying interpolation to the LTI model family. It can be shown that the LPV model captures the nonlinearity of the original system adequately.

The geometric parameters of the GTM are summarized in Table 3.1. The mass-related properties of the GTM are shown in Table 3.2. Note that all the parameters are represented in the aircraft reference system (ARS). In the ARS, the x-axis is positive forwards, the y-axis is positive toward the right wing, and the z-axis is positive downwards. The datum (origin) of the ARS is 8.745 in forward of the nose on the centerline and 16.86 in below the top of the fuselage. The gross mass and inertia matrix components are for full-fuel gear-up configuration.

Table 3.1 Geometrical parameters of the GTM.

Parameter	Symbol	Value	Unit
Planform area	S	5.9018	ft ²
Span	b	6.8488	ft
Mean aerodynamic chord	\bar{c}	0.9153	ft
Sweep	Λ	28.43	deg
Dihedral	Γ	5	deg
Leading edge of MAC	\bar{c}_{MAC}	4.5462	ft

Table 3.2 Nominal and damaged properties of the GTM.

Property	Nominal value	Damage increment	Unit
m	57.75	-0.81	lb
x_{cg}	-4.7475	0.0123	ft
y_{cg}	-0.0118	0.0523	ft
z_{cg}	-0.9761	0.0027	ft
J_x	1.221	-0.25821	slug · ft ²
J_y	4.655	-0.01727	slug · ft ²
J_z	5.587	-0.27400	slug · ft ²
J_{xy}	0.006	-0.05998	slug · ft ²
J_{yz}	0.000	-0.01346	slug · ft ²
J_{zx}	0.274	-0.00295	slug · ft ²

3.1 Nonlinear Model of a Morphing UAV

In this section, a nonlinear model of a morphing UAV is derived. First, the equations of motion of the nominal model, aerodynamic model, and the sensor and actuator models are explained in detail. Then, in the case of asymmetric variable-span morphing, the CM, inertia matrix, and aerodynamic coefficients are obtained as the functions of morphing parameters.

3.1.1 Nominal Model of a Baseline Model

Before presenting the morphing aircraft modeling, the process to construct the baseline model is explained.

Equations of Motion

The equations of motion for a morphing UAV are the same as those of a typical fixed-wing aircraft. The states shown below are directly used for numerical simulation.

In the navigation equations, flat Earth and constant gravitational acceleration are assumed. The geographic coordinate system is used to generate the position in the north-east-down (NED) coordinate system based on the world geodetic system 1984 (WGS84), which is used only for visualization of a spatial trajectory of the vehicle. The navigation equations in the geodetic coordinates can be represented as

$$\dot{\varphi} = \frac{V_N}{R_0 + h} \quad (3.1)$$

$$\dot{\lambda} = \frac{V_E \sec L}{R_0 + h} \quad (3.2)$$

$$\dot{h} = -V_D \quad (3.3)$$

where

$$\begin{bmatrix} V_N \\ V_E \\ V_D \end{bmatrix} = \begin{bmatrix} c\theta c\psi & -c\phi s\psi + s\phi s\theta c\psi & s\phi s\psi + c\phi s\theta c\psi \\ c\theta s\psi & c\phi c\psi + s\phi s\theta s\psi & -s\phi c\psi + c\phi s\theta s\psi \\ -s\theta & s\phi c\theta & c\phi c\theta \end{bmatrix} \begin{bmatrix} U \\ V \\ W \end{bmatrix} \quad (3.4)$$

and φ is the geodetic latitude, λ is the longitude, h is the height above ground, R_0 is the Earth's radius, V_N , V_E , and V_D are North, East, and down components of the velocity vector in the local geographic coordinate system, respectively, U , V , and W are x-axis, y-axis, and z-axis components of the velocity vector in the body-fixed coordinate system, respectively, ϕ , θ , and ψ are the Euler angles (roll, pitch, and yaw angles) of the vehicle body axes relative to the geographic system, respectively, and s and c stand for the sine and cosine, respectively. The forward-right-down system is used for the body-fixed coordinate system, whose origin is attached to the CM of the vehicle.

Under the assumption of constant gravitational acceleration, the force equations can be represented as

$$\dot{U} = RV - QW + \frac{X_G + X_A + X_T}{m} \quad (3.5)$$

$$\dot{V} = -RU + PW + \frac{Y_G + Y_A + Y_T}{m} \quad (3.6)$$

$$\dot{W} = QU - PV + \frac{Z_G + Z_A + Z_T}{m} \quad (3.7)$$

where

$$X_G = -g \sin \theta \quad (3.8)$$

$$Y_G = g \sin \phi \cos \theta \quad (3.9)$$

$$Z_G = g \cos \phi \cos \theta \quad (3.10)$$

and P , Q , and R are x-axis, y-axis, and z-axis components of the angular velocity vector in the body-fixed coordinate system, respectively, X_G , X_A , X_T , Y_G , Y_A , Y_T , Z_G , Z_A , and Z_T are x-axis, y-axis, and z-axis components of the gravity, aerodynamic force, and engine thrust vectors in the body-fixed coordinate system, respectively, g is the gravitational acceleration, and m is the mass of the vehicle. The aerodynamic force model and engine thrust model will be described in detail in the following subsections.

The kinematic equations of the Euler angle dynamics can be represented as

$$\dot{\phi} = P + \tan \theta (Q \sin \phi + R \cos \phi) \quad (3.11)$$

$$\dot{\theta} = Q \cos \phi - R \sin \phi \quad (3.12)$$

$$\dot{\psi} = \frac{(Q \sin \phi + R \cos \phi)}{\cos \theta} \quad (3.13)$$

The moment equations can be represented as

$$\begin{bmatrix} P \\ Q \\ R \end{bmatrix} = J^{-1} \left(\begin{bmatrix} l_A + l_T \\ m_A + m_T \\ n_A + n_T \end{bmatrix} - \begin{bmatrix} P \\ Q \\ R \end{bmatrix} \times \left(J \begin{bmatrix} P \\ Q \\ R \end{bmatrix} \right) \right) \quad (3.14)$$

where l_A , l_T , m_A , m_T , n_A , and n_T are x-axis, y-axis, and z-axis components of the aerodynamic torque vector and the torque vector generated by the engine about the CM in the body-fixed coordinate system, respectively, and J is the inertia matrix of the vehicle with respect to the body-fixed coordinate system. The gravitational moments are always zero because the equations of motion are described with respect to the CM.

Aerodynamic Model

The aerodynamic data of the NASA GTM is directly used where the aerodynamic coefficients are given as data lookup tables of aerodynamic angles only. The dependence on altitude is considered in the atmospheric density term, which is obtained from the 1976 US standard atmosphere. The dependence on airspeed is considered in the dynamic pressure term. The GTM is a medium-sized UAV (57.71 lb) that flies in the subsonic regime (Mach 0.09~0.18), while the compressibility effects may be negligible below Mach 0.3. Therefore, it can be concluded that a sufficiently accurate simulation is possible using the GTM.

The aerodynamic force components can be represented as

$$X_A = \bar{q}SC_X \quad (3.15)$$

$$Y_A = \bar{q}SC_Y \quad (3.16)$$

$$Z_A = \bar{q}SC_Z \quad (3.17)$$

where $\bar{q} = \frac{1}{2}\rho V_T^2$ are the dynamic pressure, S is the planform area of the main wing, ρ is the atmospheric density, V_T is the true airspeed (TAS), and C_X , C_Y , and C_Z are body-axis aerodynamic force coefficients.

The aerodynamic torque components can be represented as

$$\begin{bmatrix} l_A \\ m_A \\ n_A \end{bmatrix} = \begin{bmatrix} \bar{q}SbC_l \\ \bar{q}S\bar{c}C_m \\ \bar{q}SbC_n \end{bmatrix} + (\mathbf{r}_{cp} - \mathbf{r}_{cm}) \times \begin{bmatrix} X_A \\ Y_A \\ Z_A \end{bmatrix} \quad (3.18)$$

where b is the wing span, \bar{c} is the mean aerodynamic chord (MAC), C_l , C_m , and C_n are body-axis aerodynamic moment coefficients, respectively, and \mathbf{r}_{cp} and \mathbf{r}_{cm} are the position vectors of the center of pressure (25% MAC) and the CM (21.99% MAC) in the ARS.

The coefficient vector $\mathbf{C} = [C_X C_Y C_Z C_l C_m C_n]^T$ consists of the basic airframe components \mathbf{C}_{ba} , control surface components \mathbf{C}_{cs} , dynamic derivative components \mathbf{C}_{dd} , and stall-rolling moment asymmetry components \mathbf{C}_{rma} . The basic airframe component is given in the form of a data lookup table which depends on the angle of attack (AOA) and the angle of sideslip (AOS). The control surface components are also dependent on the corresponding control surface deflections. The aerodynamic coefficients are built up as

$$\mathbf{C} = \mathbf{C}_{ba} + \Delta\mathbf{C}_{cs} + \Delta\mathbf{C}_{dd} + \Delta\mathbf{C}_{rma} \quad (3.19)$$

Sensor and Actuator Models

In the GTM, five sensor systems are included.

- Air data system (ADS)
- MIDG II GPS/INS (MIDG)
- MAG3 6-DOF analog IMU with a triaxial magnetometer, accelerometer, and gyro (MAG3)
- Surface potentiometers (Pots)
- Engine control unit (ECU)

The ADS provides AOA, AOS, dynamic pressure, TAS, temperature ratio, and barometric altitude. The MIDG provides Euler angles, geodetic latitude, longitude, altitude, and geographical velocity at a 50 Hz sampling rate. The MAG3 provides angular velocity and 3-axis acceleration. The pots provide control surface deflections, and the ECU provides internal data of the left and right engines.

The sensor measurements are corrupted with appropriate dynamics, scale factor error, bias, white noise, saturation, truncation error, and transport delay.

The control surface models for elevators, ailerons, rudders, spoilers, and flaps include rate limit, saturation, transport delay, and optional dead zone with the following first-order dynamics with 5 Hz bandwidth (BW).

$$\frac{10\pi}{s + 10\pi} \quad (3.20)$$

Two Jetcat P70 engines are modeled, which include throttle-to-RPM nonlinearity (as a cubic polynomial), RPM-to-thrust nonlinearity (as a cubic polynomial), ram drag model, the influence of atmospheric pressure, and saturation with the following first-order lag model.

$$\frac{-0.1474s + 0.7314}{s^2 + 1.336s + 0.7314} \quad (3.21)$$

The fuel flow rate is given as a parabolic function of the RPM. The gyroscopic effect of the spinning rotor, off-axis thrust, and torque generated by the thrust that is not aligned with the CM and differential thrust is also included.

3.1.2 Morphing UAV Model

Based on the nominal UAV model, a morphing UAV model is derived. The GTM includes six damage cases.

- Rudder Off
- Vertical Tail Off
- Left Outboard Flap Off
- Left Wingtip Off

- Left Elevator Off
- Left Stabilizer Off

Except for the fourth case, it corresponds to the loss of the control surface. Case 4 is a loss of outboard (approximately 25% semi-span) left wingtip. The primary aerodynamic effect is a rolling moment bias to make the left wing down ($-\Delta_d C_l$), and this effect increases when alpha increases. Since the ailerons are installed at the tip of the wing, the ailerons cannot be used in the original model. However, in this study, it is assumed that the tip of the wing can telescope and the aileron can still operate as it is installed a little further inside.

If the size of the aileron is increased as much as it is closer to the centerline, the effect of the roll axis moment can be maintained the same. In this way, the magnitude of the force generated by the ailerons increases, but most of them are offset when the ailerons are used in the opposite directions. Similar to the left wing, it is assumed that the right-wing could also telescope. Using the changes in mass, inertia matrix, and aerodynamic coefficient when the tip of the left wing is lost, it is possible to model the mass, inertia matrix, and aerodynamic coefficient when the left and right wings are individually adjusted. In this study, left and right morphing parameters η_l and η_r are defined, which represent each wing's length variation ratio ranging from -25% to 0%. Then, symmetric and asymmetric morphing variables are defined as follows.

$$\eta_s = \frac{\eta_l + \eta_r}{2} \quad (3.22)$$

$$\eta_a = \frac{\eta_l - \eta_r}{2} \quad (3.23)$$

It is also assumed that the variations in the aerodynamic coefficients between both ends, the shortest and longest version of the variable span, can be

approximated through linear interpolation with acceptable errors. Note that the CM and the inertia matrix can be exactly obtained using the model information. It can be shown that the center of gravity shift is obtained as a linear function of the morphing variables, and the MOIs and POIs are obtained as a parabolic function of the morphing variables.

In the damaged configuration, the variations in the mass $\Delta_d m$, CM $\Delta_d \mathbf{r}_{cm}$, inertia matrix $\Delta_d J$, and the aerodynamic coefficients $\Delta_d \mathbf{C}$ are known. In the morphed configuration, the variations in the mass Δm , CM $\Delta \mathbf{r}_{cm}$, inertia matrix ΔJ , and the aerodynamic coefficients $\Delta \mathbf{C}$ can be represented as the functions of the morphing parameters. In this study, the quasi-static assumption is adopted, and the unsteady effect during the morphing process is not modeled because the original model does not include the unsteady effect.

Center of Mass and Inertia Matrix in Morphed Configuration

The aircraft can be divided into three components: the moving left wingtip (subscript l), stationary main body (subscript b), and the moving right wingtip (subscript r). The CM variations of the left and right wingtips in the morphed configuration can be represented as

$$\Delta \mathbf{r}_l = -\frac{\eta_l}{25} \begin{bmatrix} \frac{b \tan \Lambda}{8} \\ \frac{b}{8} \\ \frac{b \tan \Gamma}{8 \cos \Lambda} \end{bmatrix}, \quad \Delta \mathbf{r}_r = -\frac{\eta_r}{25} \begin{bmatrix} \frac{b \tan \Lambda}{8} \\ -\frac{b}{8} \\ \frac{b \tan \Gamma}{8 \cos \Lambda} \end{bmatrix} \quad (3.24)$$

where Λ is the leading edge sweep angle, and Γ is the wing dihedral angle. The gross CM variation in the morphed configuration can be represented as

$$\Delta \mathbf{r}_{cm} = \left(\frac{m_l}{m} \right) \Delta \mathbf{r}_l + \left(\frac{m_r}{m} \right) \Delta \mathbf{r}_r \quad (3.25)$$

where m_l and m_r are the mass of the left and right wingtips, respectively. Finally, the morphed gross CM can be represented as

$$\mathbf{r}_{cm} = \bar{\mathbf{r}}_{cm} + \Delta\mathbf{r}_{cm} \quad (3.26)$$

Note that

$$m_l = m_r = \Delta_d m \quad (3.27)$$

and

$$m = m_l + m_b + m_r \quad (3.28)$$

where m_b is the main body mass.

The nominal gross CM can be represented as

$$m\bar{\mathbf{r}}_{cm} = m_l\bar{\mathbf{r}}_l + m_b\bar{\mathbf{r}}_b + m_r\bar{\mathbf{r}}_r \quad (3.29)$$

where $\bar{\mathbf{r}}_l$, $\bar{\mathbf{r}}_b$, and $\bar{\mathbf{r}}_r$ are the nominal CM of the left wingtip, main body, and the right wingtip, respectively. Note that

$$\bar{\mathbf{r}}_r = \begin{bmatrix} 1 & 0 & 0 \\ 0 & -1 & 0 \\ 0 & 0 & 1 \end{bmatrix} \bar{\mathbf{r}}_l \quad (3.30)$$

The damaged gross CM can be represented as

$$(m - m_l)(\bar{\mathbf{r}}_{cm} + \Delta_d\mathbf{r}_{cm}) = m_b\bar{\mathbf{r}}_b + m_r\bar{\mathbf{r}}_r \quad (3.31)$$

Subtracting Eq. (3.31) from Eq. (3.29) yields $\bar{\mathbf{r}}_l$ as

$$m_l\bar{\mathbf{r}}_{cm} - (m - m_l)\Delta_d\mathbf{r}_{cm} = m_l\bar{\mathbf{r}}_l \quad (3.32)$$

which can be rewritten as

$$\bar{\mathbf{r}}_l = \bar{\mathbf{r}}_{cm} - \left(\frac{m}{m_l} - 1 \right) \Delta_d\mathbf{r}_{cm} \quad (3.33)$$

Now, $\bar{\mathbf{r}}_r$ can be obtained by Eq. (3.30). Then, $\bar{\mathbf{r}}_b$ can be calculated by either Eq. (3.29) or Eq. (3.31). The components' morphed CM can be represented as

$$\mathbf{r}_i = \bar{\mathbf{r}}_i + \Delta\mathbf{r}_i, \quad i = l, b, r \quad (3.34)$$

By applying the parallel axis theorem, also known as the Huygens-Steiner theorem, the nominal and morphed gross inertia matrix can be represented as

$$\bar{J} = \bar{J}_l - m_l[\bar{\mathbf{r}}_l - \bar{\mathbf{r}}_{cm}]^2 + \bar{J}_b - m_b[\bar{\mathbf{r}}_b - \bar{\mathbf{r}}_{cm}]^2 + \bar{J}_r - m_r[\bar{\mathbf{r}}_r - \bar{\mathbf{r}}_{cm}]^2 \quad (3.35)$$

$$J = \bar{J}_l - m_l[\mathbf{r}_l - \mathbf{r}_{cm}]^2 + \bar{J}_b - m_b[\mathbf{r}_b - \mathbf{r}_{cm}]^2 + \bar{J}_r - m_r[\mathbf{r}_r - \mathbf{r}_{cm}]^2 \quad (3.36)$$

where \bar{J}_l , \bar{J}_b , and \bar{J}_r are the inertia matrices about their own centers of mass, respectively. Note that $[\mathbf{r}]$ is a skew-symmetric matrix associated with $\mathbf{r} = [x \ y \ z]^T$ as

$$[\mathbf{r}] = \begin{bmatrix} 0 & -z & y \\ z & 0 & -x \\ -y & x & 0 \end{bmatrix} \quad (3.37)$$

The following equation can be useful.

$$-[\mathbf{r}]^2 = \begin{bmatrix} y^2 + z^2 & -xy & -xz \\ -yx & x^2 + z^2 & -yz \\ -zx & -xy & x^2 + y^2 \end{bmatrix} = \text{tr}(\mathbf{r}\mathbf{r}^T)I_3 - \mathbf{r}\mathbf{r}^T \quad (3.38)$$

Finally, the inertia matrix variation due to morphing can be obtained by subtracting Eq. (3.35) from Eq. (3.36) as

$$\begin{aligned} \Delta J = & m_l[\bar{\mathbf{r}}_l - \bar{\mathbf{r}}_{cm}]^2 + m_b[\bar{\mathbf{r}}_b - \bar{\mathbf{r}}_{cm}]^2 + m_r[\bar{\mathbf{r}}_r - \bar{\mathbf{r}}_{cm}]^2 \\ & - m_l[\mathbf{r}_l - \mathbf{r}_{cm}]^2 - m_b[\mathbf{r}_b - \mathbf{r}_{cm}]^2 - m_r[\mathbf{r}_r - \mathbf{r}_{cm}]^2 \end{aligned} \quad (3.39)$$

The parameter variation due to η_l and η_s are shown in Figs. 3.2 and 3.3. The x-axis moment of inertia can be varied up to 23%, which means that the roll rate

can be increased up to 30% by retracting the span due to angular momentum conservation. The CM can be shifted up to 1.3% MAC off the plane of symmetry by asymmetric morphing. Note that the CM moving back and forth up to 0.23% MAC due to nonzero sweep may affect the longitudinal stability where the nominal static margin is 3.01% MAC.

Aerodynamic Model

In the variable-span morphing wing, the lift coefficient is almost linearly proportional to the span [129] due to the fact that the area of the lifting surface is linearly proportional to the span. The total drag in the subsonic flow consists of the profile drag and the induced drag. The drag coefficient for the induced drag of a high-aspect lightly-swept wing, in subsonic flow, can be modeled as follows [130].

$$C_{D_i} = \frac{C_L^2}{\pi e AR} \quad (3.40)$$

where e is the efficiency factor which is close to unity, and AR is the aspect ratio defined as follows.

$$AR = \frac{b^2}{S}$$

Therefore, the induced drag also varies linearly with respect to η_s . When an aircraft's wing is not stalled, the aircraft's parasite drag is almost entirely comprised of skin friction [131]. The quantity of skin friction drag depends on the aircraft's wetted area. Therefore, the parasite drag and, in turn, the total drag can also be assumed to be linearly varying with respect to η_s .

Similarly, the pitching moment coefficient and crosswind force coefficient can be assumed to vary linearly. Unlike the longitudinal and force coefficients, rolling and yawing moment coefficients vary parabolically with span because

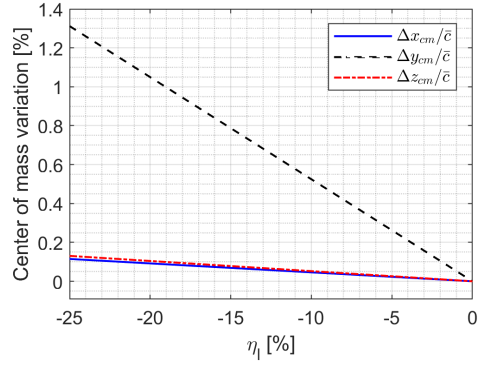
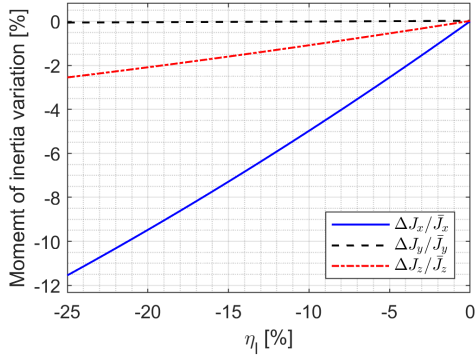


Figure 3.2 Parameter variation due to η_l when $\eta_r = 0\%$.

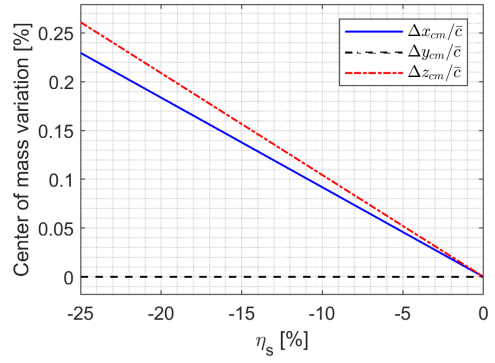
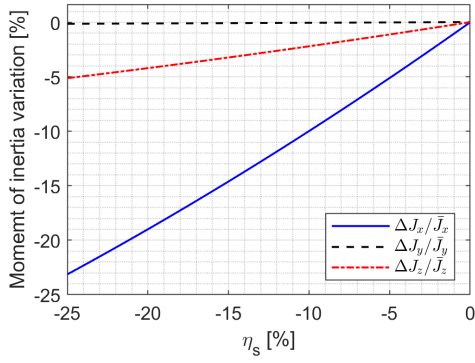


Figure 3.3 Parameter variation due to η_s when $\eta_a = 0\%$.

the moment arm also varies linearly. However, the impact of variation in the moment arm may not be significant if the moving part of the span is relatively short compared to the entire wing. Therefore, the rolling and yawing moment coefficient increment due to morphing can also be assumed to be proportional to the morphing parameter.

The aerodynamic coefficient variation due to left span morphing can be represented as

$$\Delta_l \mathbf{C}(\alpha, \beta) = -\left(\frac{\eta_l}{25}\right) \Delta_d \mathbf{C}(\alpha, \beta) \quad (3.41)$$

Note that

$$\Delta_r \mathbf{C}(\alpha, \beta) = \text{diag}(1, -1, 1, -1, 1, -1) \Delta_l \mathbf{C}(\alpha, -\beta) \quad (3.42)$$

Finally, the aerodynamic coefficient variation in the morphed configuration can be represented as

$$\Delta \mathbf{C}(\alpha, \beta) = \Delta_l \mathbf{C}(\alpha, \beta) + \Delta_r \mathbf{C}(\alpha, \beta) \quad (3.43)$$

When $\beta \approx 0$ in Eq. (3.42),

$$\Delta_r \mathbf{C}_{lon} = \Delta_l \mathbf{C}_{lon} \quad (3.44)$$

$$\Delta_r \mathbf{C}_{lat} = -\Delta_l \mathbf{C}_{lat} \quad (3.45)$$

where $\mathbf{C}_{lon} = [C_X \ C_Z \ C_m]^T$ and $\mathbf{C}_{lat} = [C_Y \ C_l \ C_n]^T$. Then,

$$\Delta \mathbf{C}_{lon} = -2 \left(\frac{\eta_s}{25}\right) \Delta_d \mathbf{C} \quad (3.46)$$

$$\Delta \mathbf{C}_{lat} = -2 \left(\frac{\eta_a}{25}\right) \Delta_d \mathbf{C} \quad (3.47)$$

Note that the longitudinal motion is affected by symmetric morphing, while the lateral-directional motion is affected by asymmetric morphing. If the configuration where $\eta_l = \eta_r = -12.5\%$ is selected as a nominal configuration,

the maximum variation in the aerodynamic coefficients becomes $\pm\Delta_d\mathbf{C}$ which are shown in Fig. 3.4. The morphing parameters are suitable for control input because they appear affinely in the forces and moments. It is shown in Fig. 3.4 that the increments are almost linearly proportional in the pre-stall region where $\alpha \in [-5, 10]$ deg, while the conventional control surface increments are only lightly affected by the AOA as shown in Fig. 3.5. As a result, the control effectiveness of asymmetric morphing in the roll axis is low when the AOA is small. However, the effectiveness of asymmetric morphing becomes even greater than the ailerons in the post-stall region ($\alpha > 10$ deg), as shown in Fig. 3.5. Furthermore, symmetric morphing can be used to delay stall in the low-speed flights or the high-g maneuvers by increasing the lift coefficient, which in turn has the effect of decreasing the AOA toward the pre-stall region while generating the same lift.

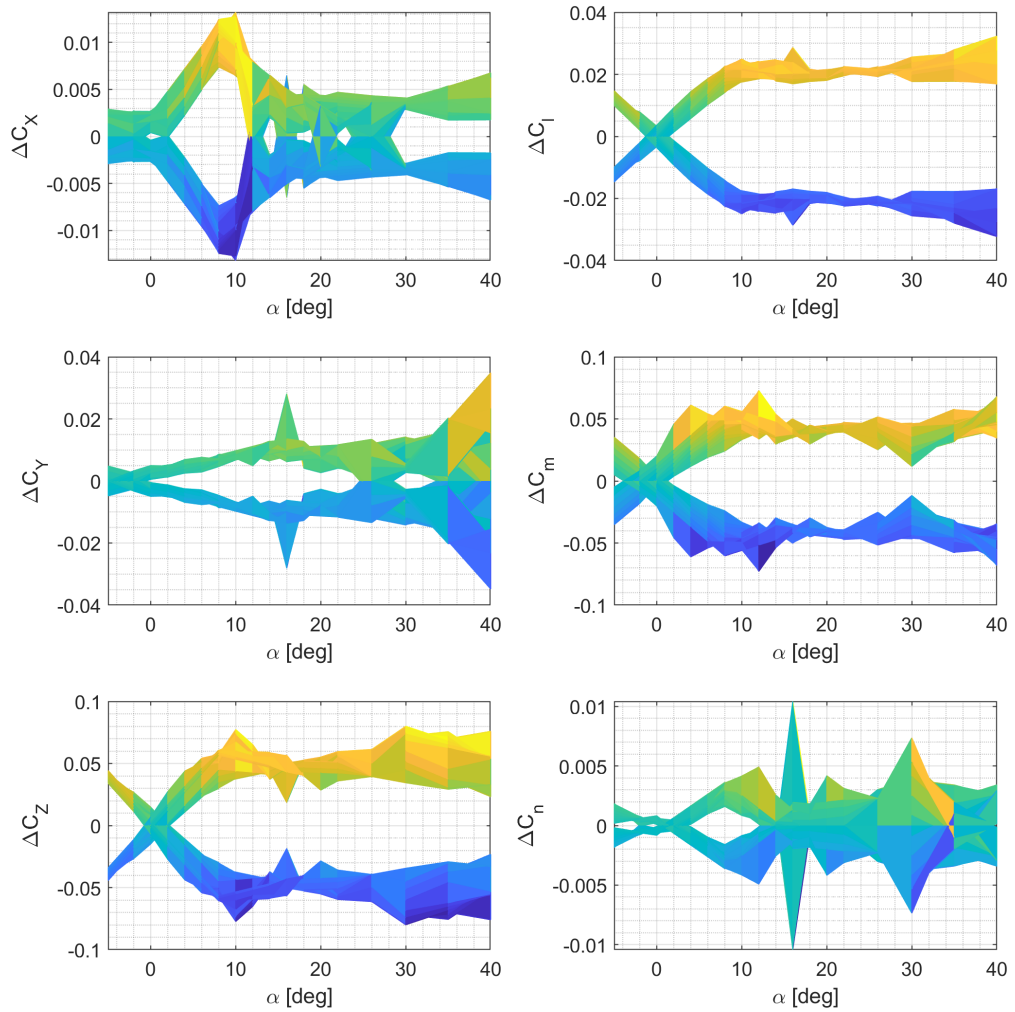


Figure 3.4 Maximum variation of the aerodynamic coefficients from the nominal configuration due to morphing when $\beta \in [-20, 20]$ deg.

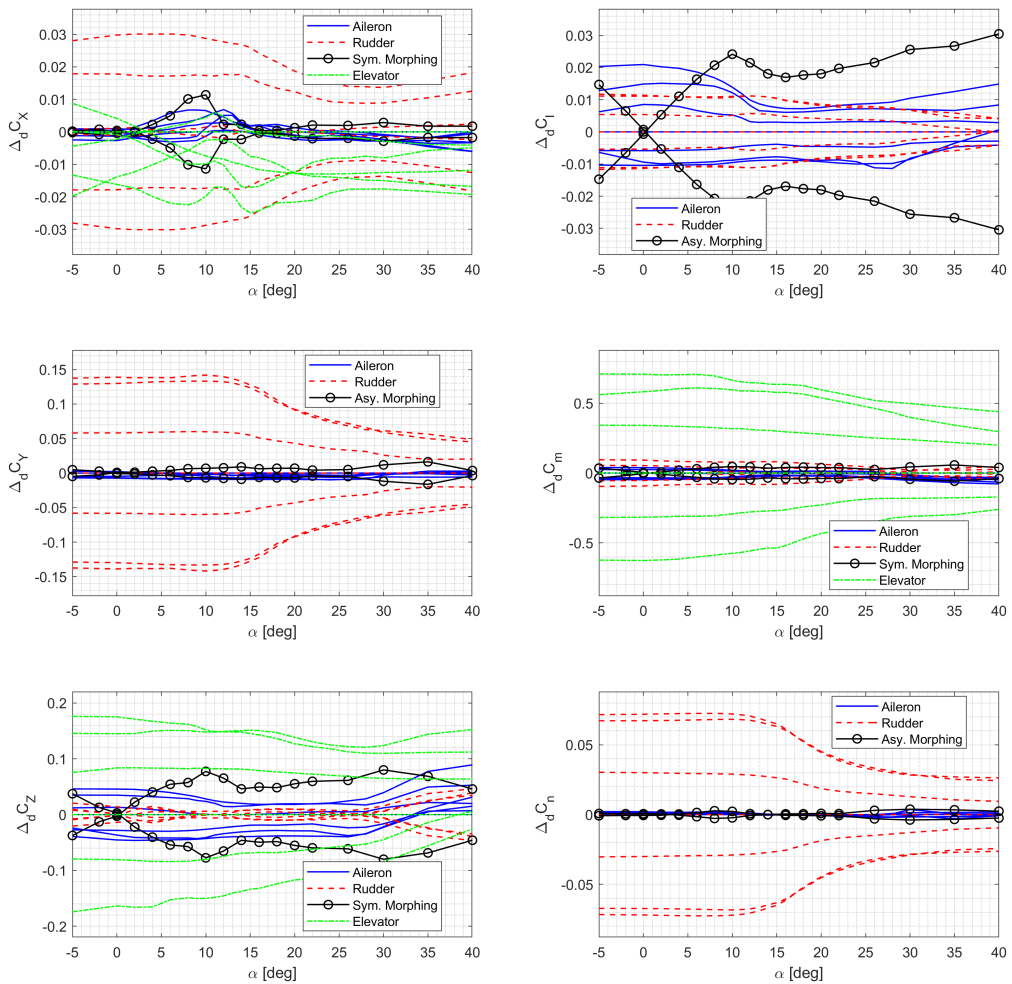


Figure 3.5 Control surface increment to the aerodynamic coefficients when $\beta = 0$ deg.

3.2 Derivation of an LPV Model of a Morphing UAV

In this section, the LPV model of morphing UAVs is derived.

3.2.1 Trim Analysis and Scheduling Parameter Selection

In this study, airspeed and altitude are adopted as the scheduling parameters. In addition, the symmetric morphing parameter is included in the scheduling parameters because it has significant impacts on longitudinal aerodynamics, which influences the overall flight performance. The asymmetric morphing parameter has little impact on the longitudinal motion but can be useful as a control input in the lateral-directional motion.

Note that a rectangular parameter grid is required for the design of the LPV controller. However, the trimmable region of the GTM in the TAS versus altitude diagram appears to be a triangular shape as shown in Fig. 3.6. The service ceiling is approximately 30,000 ft, where the trimmable TAS converges to approximately 100 kt. Therefore, it is required to introduce a new speed-related parameter such that the parameter grid becomes rectangular shape. In this study, the following synthetic airspeed is introduced.

$$V_S = V_0 - \frac{h_0}{h_0 - h}(V_0 - V_T), \quad h < h_0 \quad (3.48)$$

where $V_0 = 100$ kt and $h_0 = 30,000$ ft. Note that Eq. (3.48) becomes singular when $h = h_0$. However, the normal operating altitude of medium-size UAVs such as GTM is much lower than 30,000 ft. Then, the flight envelope becomes a rectangle, as shown in Fig. 3.7. Now, the scheduling parameter vector $\boldsymbol{\rho} \triangleq [V h \eta_s]^T$ with three parameters is considered. The considered parameter grid is

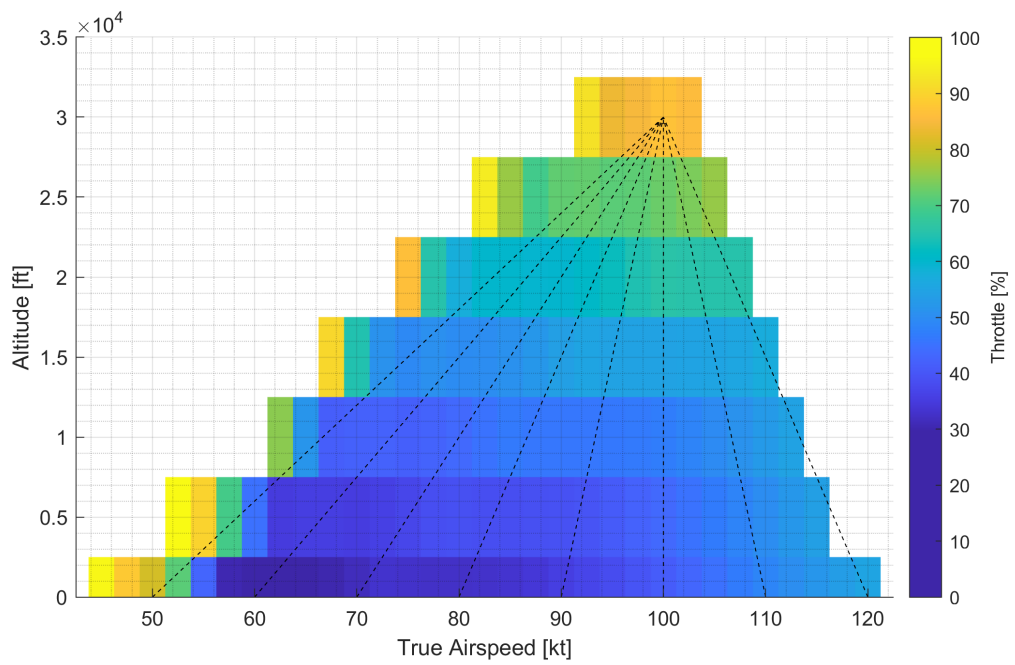


Figure 3.6 Trimmable region of the nominal GTM.

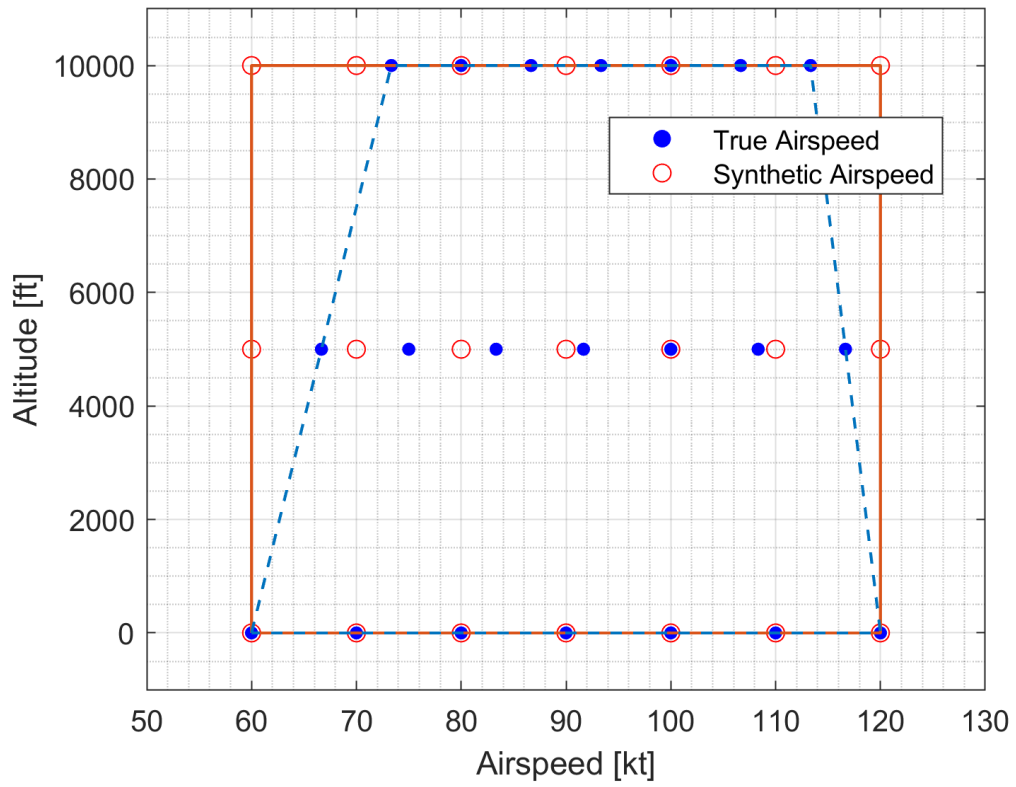


Figure 3.7 Rectangular scheduling parameter domain.

- $V_S \in [60, 70, 80, 90, 100, 110, 120]$ in kt
- $h \in [0, 5,000, 10,000]$ in ft
- $\eta_s \in [-25, -12.5, 0]$ in %

It is shown in Fig. 3.8 that trim throttle increase as the wingspan decrease, but the tendency can be reversed in the high-speed regime.

3.2.2 Pointwise Linearization of a Nonlinear Model

The equations of motion can be decoupled into equations describing the longitudinal motion and the lateral-directional motion. The LTI models for the decoupled motions can be obtained at each parameter grid through Jacobian linearization. The wind axis is chosen in this study because it has advantages in decoupling.

The wind-axis longitudinal equations of motion can be described as

$$\begin{aligned}
 \begin{bmatrix} \dot{V}_T \\ \dot{\alpha} \\ \dot{q} \\ \dot{\theta} \end{bmatrix} &= \begin{bmatrix} X_V + X_{T_V} \cos(\alpha_0 + \alpha_T) & X_\alpha & 0 & -g \cos \gamma_0 \\ \frac{Z_V - Z_{T_V} \sin(\alpha_0 + \alpha_T)}{V_0} & \frac{Z_\alpha}{V_0} & 1 + \frac{Z_q}{V_0} & -\frac{g \sin \gamma_0}{V_0} \\ M_V + M_{T_V} & M_\alpha + M_{T_\alpha} & M_q & 0 \\ 0 & 0 & 1 & 0 \end{bmatrix} \begin{bmatrix} V_T \\ \alpha \\ q \\ \theta \end{bmatrix} \\
 &+ \begin{bmatrix} X_{\delta_t} \cos(\alpha_0 + \alpha_T) & X_{\delta_e} \\ -\frac{X_{\delta_t} \sin(\alpha_0 + \alpha_T)}{V_0} & \frac{Z_{\delta_e}}{V_0} \\ M_{\delta_t} & M_{\delta_e} \\ 0 & 0 \end{bmatrix} \begin{bmatrix} \delta_t \\ \delta_e \end{bmatrix} \quad (3.49)
 \end{aligned}$$

The short-period mode dynamics can be extracted by eliminating the phugoid

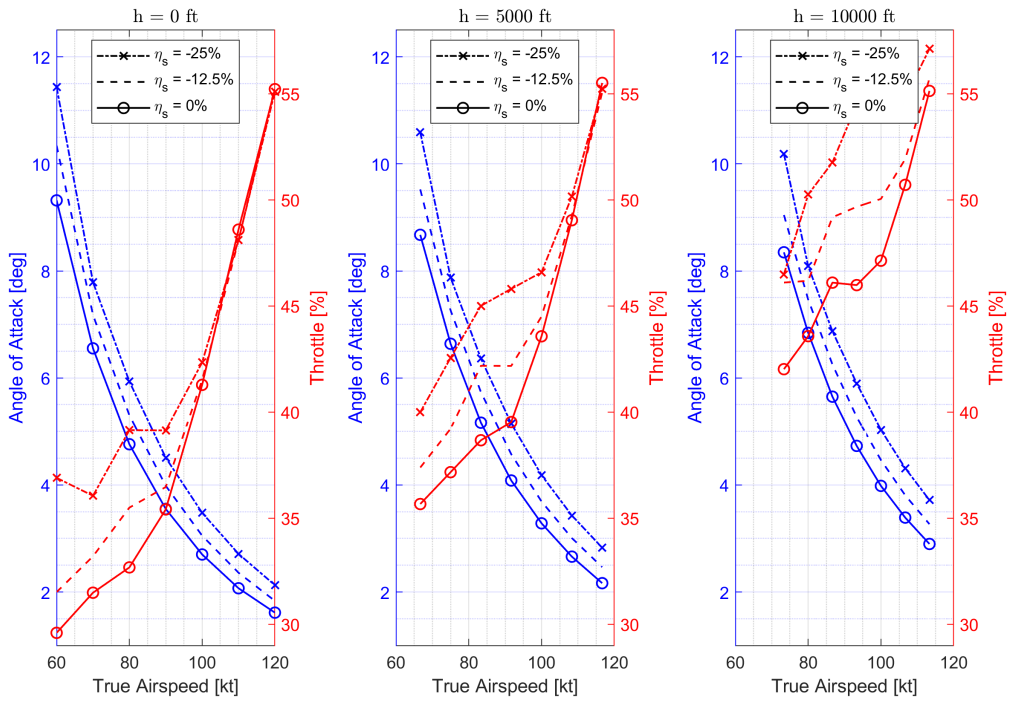


Figure 3.8 Trim angle of attack and throttle.

mode dynamics as

$$\begin{bmatrix} \dot{\alpha} \\ \dot{q} \end{bmatrix} = \begin{bmatrix} \frac{Z_\alpha}{V_0} & 1 + \frac{Z_q}{V_0} \\ M_\alpha + M_{T_\alpha} & M_q \end{bmatrix} \begin{bmatrix} \alpha \\ q \end{bmatrix} + \begin{bmatrix} X_{\delta_e} \\ \frac{Z_{\delta_e}}{V_0} \end{bmatrix} \delta_e \quad (3.50)$$

The short-period mode dynamic is used for a longitudinal CAS design. The z-axis acceleration can be augmented to the measurement equation as

$$\begin{bmatrix} \alpha \\ q \\ a_z \end{bmatrix} = \begin{bmatrix} 1 & 0 \\ 0 & 1 \\ Z_\alpha & 0 \end{bmatrix} \begin{bmatrix} \alpha \\ q \end{bmatrix} + \begin{bmatrix} 0 \\ 0 \\ Z_{\delta_e} \end{bmatrix} \delta_e \quad (3.51)$$

Note that the transfer function from δ_e to the a_z has a non-minimum phase (NMP) zero. In this case, the initial response to a step input may have the opposite sign to the final response. The altitude dynamics can be augmented to the longitudinal dynamics as

$$\begin{bmatrix} \dot{V}_T \\ \dot{\alpha} \\ \dot{q} \\ \dot{\theta} \\ \dot{h} \end{bmatrix} = \begin{bmatrix} X_V + X_{T_V} \cos(\alpha_0 + \alpha_T) & X_\alpha & 0 & -g \cos \gamma_0 & 0 \\ \frac{Z_V - Z_{T_V} \sin(\alpha_0 + \alpha_T)}{V_0} & \frac{Z_\alpha}{V_0} & 1 + \frac{Z_q}{V_0} & -\frac{g \sin \gamma_0}{V_0} & 0 \\ M_V + M_{T_V} & M_\alpha + M_{T_\alpha} & M_q & 0 & 0 \\ 0 & 0 & 1 & 0 & 0 \\ 0 & -V_0 & 0 & V_0 & 0 \end{bmatrix} \begin{bmatrix} V_T \\ \alpha \\ q \\ \theta \\ h \end{bmatrix} \quad (3.52)$$

$$+ \begin{bmatrix} X_{\delta_t} \cos(\alpha_0 + \alpha_T) & X_{\delta_e} \\ -\frac{X_{\delta_t} \sin(\alpha_0 + \alpha_T)}{V_0} & \frac{Z_{\delta_e}}{V_0} \\ M_{\delta_t} & M_{\delta_e} \\ 0 & 0 \\ 0 & 0 \end{bmatrix} \begin{bmatrix} \delta_t \\ \delta_e \end{bmatrix}$$

The augmented dynamics is used for longitudinal autopilot design.

For the control of the lateral-directional motion, the asymmetric morphing parameter is included in the control input. The lateral-directional dynamics, where the differential thrust is not considered, can be represented as

$$\begin{bmatrix} \dot{\beta} \\ \dot{p} \\ \dot{r} \\ \dot{\phi} \end{bmatrix} = \begin{bmatrix} \frac{Y_\beta}{V_0} & \frac{Y_p}{V_0} & \frac{Y_r}{V_0} - 1 & \frac{g \cos \theta_0}{V_0} \\ L_\beta & L_p & L_r & 0 \\ N_\beta & N_p & N_r & 0 \\ 0 & \frac{\cos \gamma_0}{\cos \theta_0} & \frac{\sin \gamma_0}{\cos \theta_0} & 0 \end{bmatrix} \begin{bmatrix} \beta \\ p \\ r \\ \phi \end{bmatrix} + \begin{bmatrix} \frac{Y_{\delta_a}}{V_0} & \frac{Y_{\delta_r}}{V_0} & \frac{Y_{\eta_a}}{V_0} \\ L_{\delta_a} & L_{\delta_r} & L_{\eta_a} \\ N_{\delta_a} & N_{\delta_r} & N_{\eta_a} \\ 0 & 0 & 0 \end{bmatrix} \begin{bmatrix} \delta_a \\ \delta_r \\ \eta_a \end{bmatrix} \quad (3.53)$$

Equation (3.53) is used for lateral-directional autopilot design. When the air-speed is sufficiently high, the roll angle dynamics becomes negligible. In this case, the roll angle dynamics can be eliminated as

$$\begin{bmatrix} \dot{\beta} \\ \dot{p} \\ \dot{r} \end{bmatrix} = \begin{bmatrix} \frac{Y_\beta}{V_0} & \frac{Y_p}{V_0} & \frac{Y_r}{V_0} - 1 \\ L_\beta & L_p & L_r \\ N_\beta & N_p & N_r \end{bmatrix} \begin{bmatrix} \beta \\ p \\ r \end{bmatrix} + \begin{bmatrix} \frac{Y_{\delta_a}}{V_0} & \frac{Y_{\delta_r}}{V_0} & \frac{Y_{\eta_a}}{V_0} \\ L_{\delta_a} & L_{\delta_r} & L_{\eta_a} \\ N_{\delta_a} & N_{\delta_r} & N_{\eta_a} \end{bmatrix} \begin{bmatrix} \delta_a \\ \delta_r \\ \eta_a \end{bmatrix} \quad (3.54)$$

Equation (3.54) is used for lateral-directional CAS design.

3.2.3 Linear Parameter-Varying Modeling and Analysis

By applying interpolation to the family of LTI models, an LPV model can be obtained. The open-loop pole-zero maps for longitudinal and lateral-directional dynamics are shown in Figs. 3.9 and 3.10. Note that the pole locations can be significantly changed by morphing. It is observed that the spiral mode becomes unstable in a certain configuration.

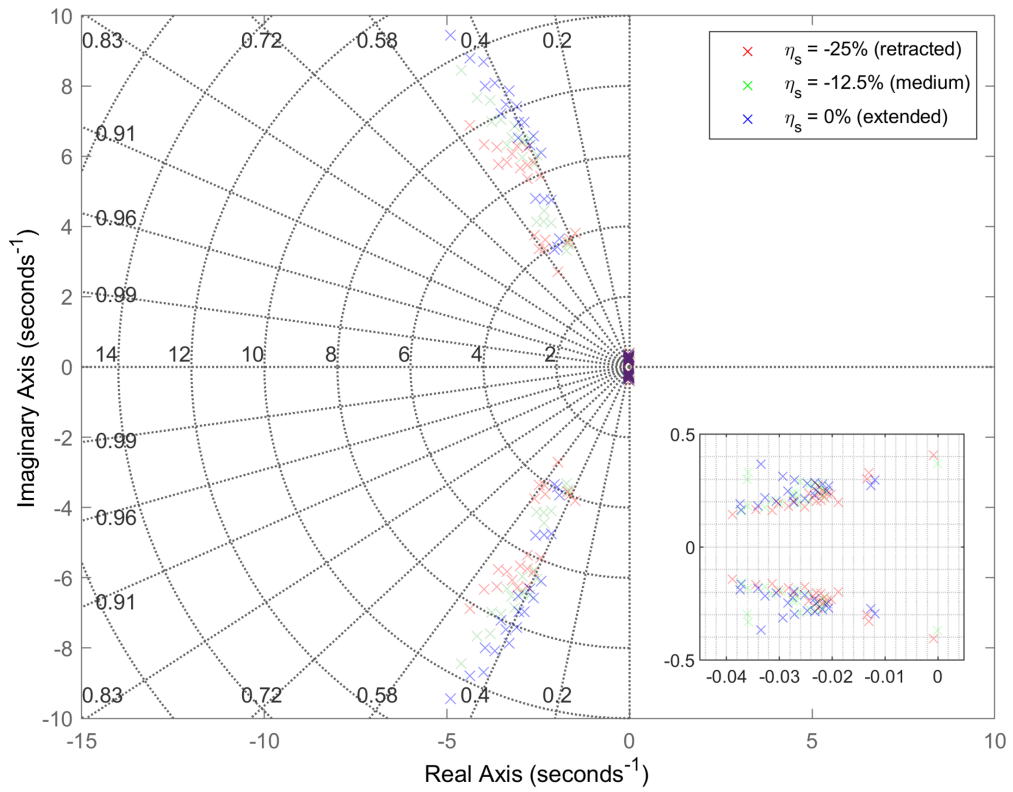


Figure 3.9 Longitudinal open-loop poles in various configurations.

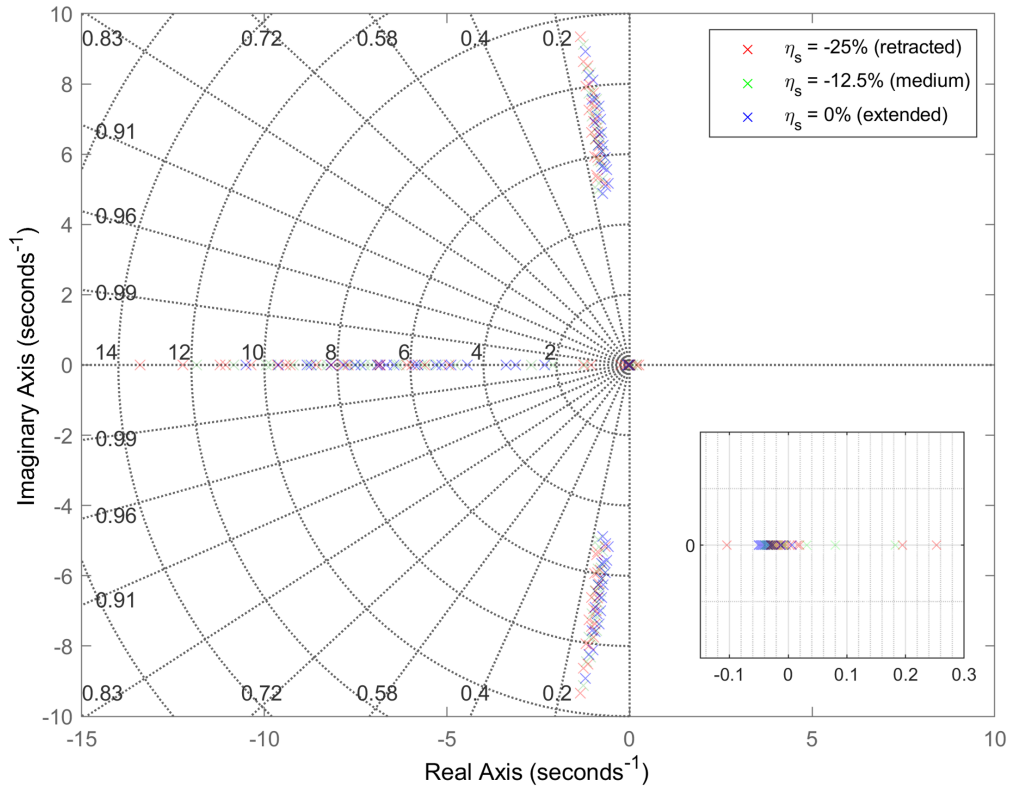


Figure 3.10 Lateral-directional open-loop poles in various configurations.

Chapter 4

CAS Design Based on LPV Method for Morphing-Assisted Maneuvers

Depending on the degree of autonomy of the UAV, a human pilot is involved to some extent in controlling the UAV. In general, the speed of the rotation modes determines the responsiveness of a UAV to maneuvering commands. Typically, the rotation modes are so fast that it is difficult for a human pilot to manually operate the UAV if the modes are unstable or lightly damped. Therefore, a stability augmentation system (SAS) is required to ensure desired dynamic characteristics for these modes. A control augmentation system is designed to not only govern the mode but also offer a specific form of response to the command. Even though slow modes such as phugoid and spiral modes can be manually controlled, an automatic control system is required to relieve the pilot from hand flying because it is undesirable for a pilot to pay constant attention. An autopilot is an automatic control system that provides both pilot relief and specialized functions such as path following and automatic landing. The typical types of SASs, CASs, and autopilots are shown in Table 4.1 [131].

In this study, a control system design framework shown in Fig. 4.1 is considered. The flight control system (FCS) depends on the control mode, guidance commands, and scheduling parameters. The CAS modes and autopilot

Table 4.1 Typical types of automatic control systems.

SAS	CAS	Autopilot
Roll damper	Normal acceleration	Speed (Mach)
Pitch damper	Pitch rate	Altitude
Yaw damper	Roll rate	Roll
	Lateral-directional	Turn coordination
		Pitch
		Heading
		Landing

modes for the longitudinal and lateral-directional channels are considered for the control modes. The guidance command is determined in accordance with the intended form of flight. The controller gains of the FCS are scheduled on the morphing parameters and the flight conditions in a manner that ensures stability, and the actuator commands are computed where the morphing actuator is also included in control inputs. The morphing system governs the morphing configuration in a manner that satisfies the control command, aids the commanded maneuver, and provides the desired dynamic characteristics based on the flight conditions. The conventional control surfaces are usually designed to provide aerodynamic forces and moments primarily for the intended channel with minimal cross-coupling effects and impacts on the mass properties. However, the morphing configuration change affects the characteristics of the airframe dynamics in a different way than the conventional control surfaces.

In this chapter, CASs are designed for morphing-assisted maneuvers of morphing UAVs based on the LPV methods to provide a rigorous stability guarantee under arbitrary morphing. A longitudinal CAS is designed to track the normal acceleration command in Sec. 4.1. A lateral-directional CAS is designed to track the AOS and roll rate commands in Sec. 4.2. The CASs utilize the symmetric morphing parameter for improved performance and the asymmetric morphing parameter for flight control, respectively. The symmetric morphing strategy is discussed in Sec. 4.3. In Sec. 4.4, numerical simulation is performed for the push-over and pull-up and the high-g turn to demonstrate the effectiveness of the proposed scheme. The proposed gain self-scheduled flight control system is compared with the gain-scheduled \mathcal{H}_∞ controller.

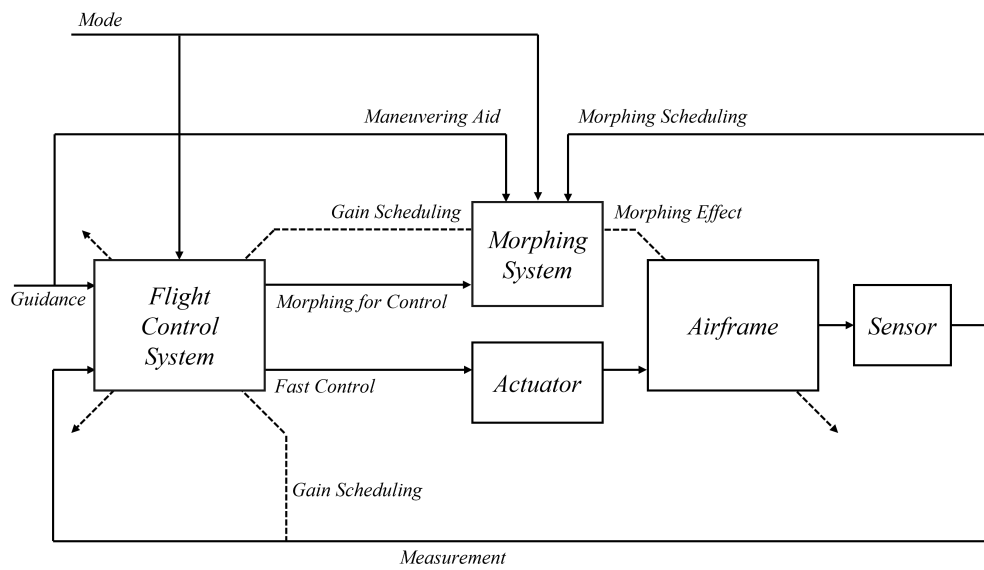


Figure 4.1 Control system design framework for morphing UAV

4.1 Longitudinal CAS Design for Normal Acceleration Control

In this section, a normal acceleration CAS is designed based on LPV methods for the control of longitudinal motion. A specialized CAS is required for high-performance UAVs when the pilot has to maneuver the UAV to its performance limits. The normal acceleration is an appropriate variable for controlling the pitch axis in this situation, which is the component of acceleration in the direction opposing the body-fixed z-axis. The accelerometer output has a component that is proportional to the AOA, and the unstable short-period mode can be stabilized. Furthermore, the accelerometer is generally less noisy and more reliable than the AOA sensor.

Note that the transfer function from the elevator deflection to the normal acceleration has a non-minimum phase (NMP) zero. The initial normal acceleration response to a negative step elevator deflection will be negative, followed by the expected positive normal acceleration. When the elevator is deflected upward to produce a positive normal acceleration, the downward force on the tail increases. As a result, the center of mass may drop momentarily, causing normal acceleration to become negative before increasing again. Therefore, it is important to consider the NMP behavior when designing the normal acceleration control system. The remaining degree of freedom in the throttle setting can be controlled manually, or an autothrottle can be applied.

4.1.1 Performance Specifications

The closed-loop interconnection structure shown in Fig. 4.2 is considered for the design of the longitudinal CAS. The 1-degree-of-freedom controller is consid-

ered. The open-loop plant P is composed of the state equation, Eq. (3.50), and the output equation, Eq. (3.51). The control design problem is cast in the model-matching framework. The control objective is to minimize the weighted normal acceleration model matching error and the weighted control effort against the command, noise, and disturbance.

The external input vector w is assumed to be broadband \mathcal{L}_2 signal. For design convenience, the \mathcal{L}_2 -norm of the external inputs can be regarded as unity. In this case, the control objective becomes making the performance output less than unity, and the weighting filters are designed accordingly. Note that the frequency-dependent weights can be designed as real, rational, and proper transfer matrices whose elements are possibly dependent on the scheduling parameter. That is, the performance objectives themselves can also be scheduled on the scheduling parameter. The open-loop plant P is the LPV model obtained in Sec. 3.2. The actuator model P_a is designed to reflect the realistic responses of the control surfaces to the control input commands. The reference weight W_r corresponds to the maximum expected guidance command. The model weight W_m corresponds to the ideal model response to the unit step guidance command. The performance weight W_p shapes the relative importance of the model matching error throughout the frequency range. The noise weight W_n corresponds to the expected sensor noise level across the frequency range. The control weight W_c shapes the control effort penalty to the actuator command in the undesirable frequency range. The disturbance weight D_a corresponds to the expected disturbance to the actuator output. The time delay T_d corresponds to the expected transport delay.

The elevator is modeled as a first-order system with a bandwidth of 5 Hz.

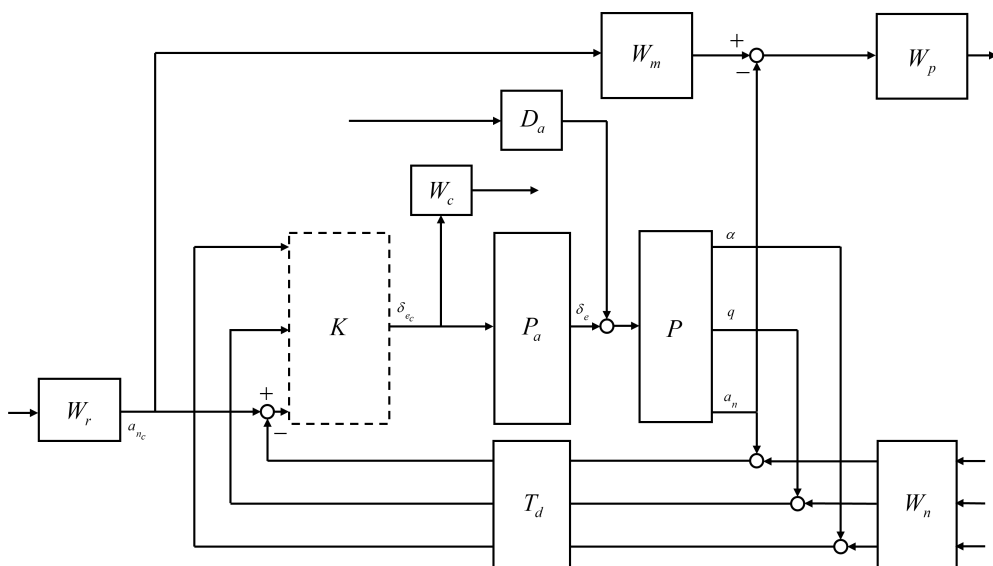


Figure 4.2 Closed-loop interconnection structure of the longitudinal CAS.

Except for some highly agile maneuvers, in most cases, the vertical acceleration command does not exceed 2g, and therefore the reference weight is set to 2g. The ideal model for the normal acceleration response to the command is set to have a natural frequency of 2.5 rad/s and a damping ratio of 0.8 to allow for some overshoot. Performance weights are set such that the model matching error does not exceed five times the normal acceleration measurement noise level at low frequencies. The sensor measurement error is modeled as white Gaussian noise, and the standard deviation is set to match the sensor specifications of the GTM. In the elevator model, a disturbance of 0.01 deg is added below 0.5 rad/s to account for errors due to dead zone, saturation, and rate limit. A first-order Padé approximant corresponding to a transport delay of 30 ms is applied to all sensor measurements. Note that the Laplace transform of a time delay of T is e^{-sT} , and the exponential transfer function can be approximated by a rational transfer function using Padé approximation formulas. Given the order of a rational function, Padé approximant is known as the best approximation. High-order Padé approximations produce transfer functions with clustered poles. In general, Padé approximations with high order ($N > 10$) are not preferred because their poles are sensitive to perturbations. The weighting filters are summarized in Table 4.2.

4.1.2 Controller Synthesis and Analysis

The generalized open-loop plant has 11 states and depends on three scheduling parameters. The LPV controller is synthesized to satisfy the performance objectives according to the performance specifications defined in the generalized open-loop plant. The synthesized LPV controller guarantees that the

Table 4.2 Weighting filters for the longitudinal CAS design.

Weighting Filter	Value
P_a	$\frac{31.42}{s+31.42}$
W_r	$3 \cdot 32.174$
W_m	$\frac{2.5^2}{s^2+2 \cdot 0.8 \cdot 2.5s+2.5^2}$
W_p	$\frac{5 \cdot 0.0082 \cdot 32.174(s/2.5+1)}{s/0.04+1}$
W_{n_α}	$0.031 \cdot 0.1745$
W_{n_q}	$0.3857 \cdot 0.1745$
$W_{n_{an}}$	$0.0082 \cdot 32.174$
W_c	$\frac{0.0001(s/0.5+1)}{s/120+1}$
D_a	$\frac{0.01}{s/0.5+1}$
T_d	$\left(\frac{-s+66.67}{s+66.67} \right) I_3$

closed-loop system is quadratically stable and the \mathcal{L}_2 gain from the external input $\mathbf{w} \in \mathcal{L}_2$ to the performance output \mathbf{z} is less than $\gamma \geq 0$ under arbitrary time-varying scheduling parameter $\boldsymbol{\rho} \in \mathcal{P}$. The LPV synthesis problem is solved twice. In the first iteration, an optimal solution that minimizes the induced \mathcal{L}_2 -norm of $F_l(G, K)$ is obtained. In the second iteration, a suboptimal solution whose γ is at most 20% greater than the γ obtained in the first iteration for better numerical conditioning. As a result of LPV synthesis, suboptimal $\gamma = 2.1505$ is obtained, which is 10.9% greater than the optimal $\gamma = 1.9387$. The \mathcal{H}_∞ controller is synthesized with respect to the point-wise LTI models whose γ ranges from 0.2006 to 0.2258. Note that the \mathcal{H}_2 controller can also be synthesized in the same way. The synthesis time is the largest in the LPV controller and the smallest in the \mathcal{H}_2 controller.

The performance of the LPV controller and the \mathcal{H}_∞ controller can be compared in a point-wise LTI manner. Note that this comparison favors the \mathcal{H}_∞ controller because the time variation of the scheduling parameter is not considered. The open-loop and closed-loop Bode gain plot is shown in Fig. 4.3. It is observed that the performance of the LPV controller can be better or worse according to the scheduling parameter. The step response is shown in Fig. 4.4. From this result, it can be seen that the LPV controller is scheduled according to the scheduling parameter, while the \mathcal{H}_∞ controller is forced to show almost the same response even if the scheduling parameter is changed.

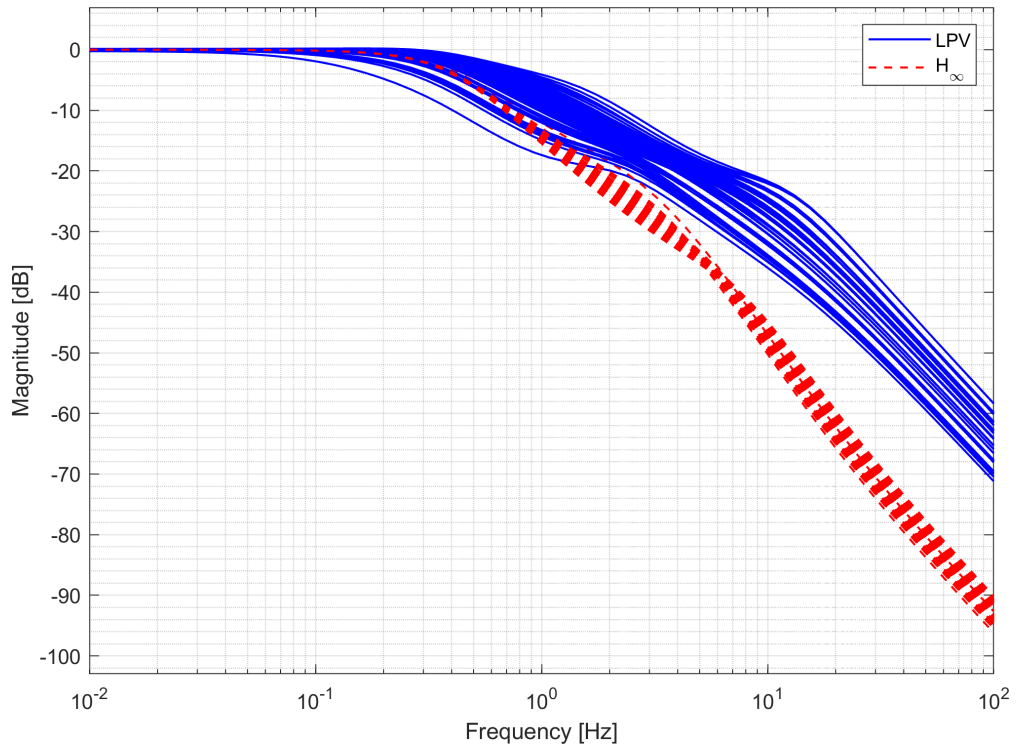


Figure 4.3 Bode magnitude plot of the normal acceleration CAS.

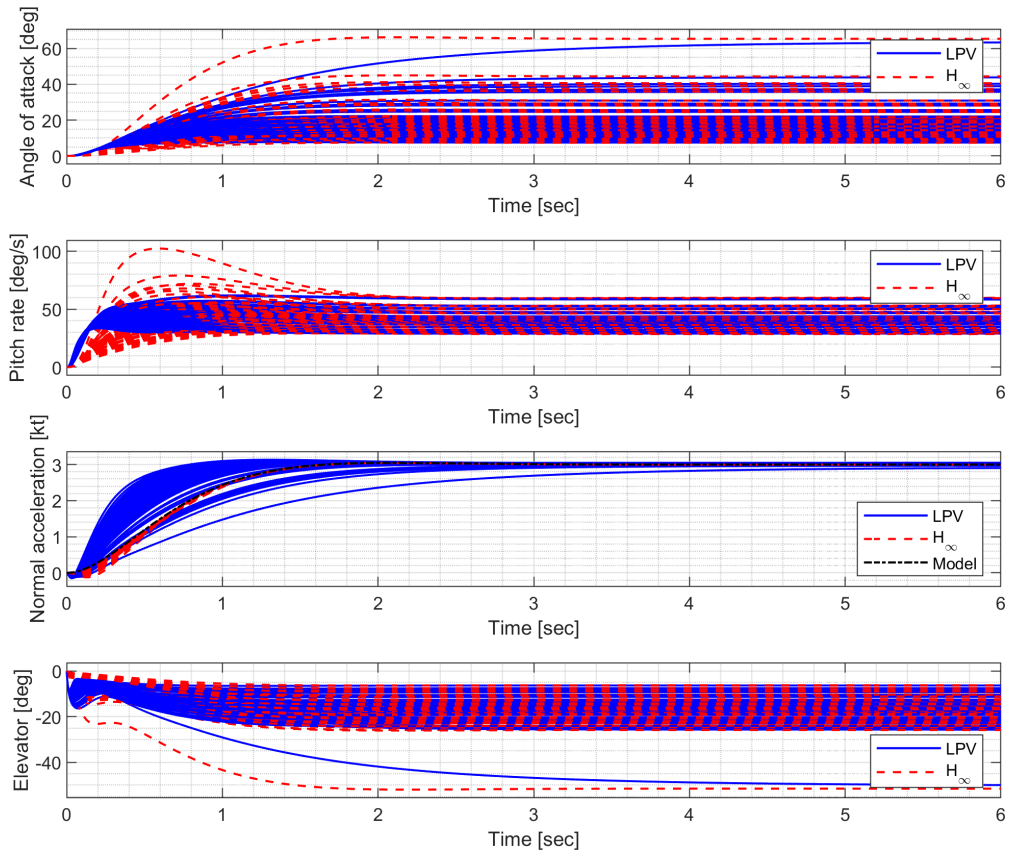


Figure 4.4 Step response of the normal acceleration CAS.

4.2 Lateral-Directional CAS Design for Turn Coordination and Roll Rate Control

In this section, a roll rate CAS is designed based on LPV methods for the control of lateral-directional motion. Regarding lateral-direction control, the roll-rate command system is the most prevalent control augmentation system. This mechanism may be constructed to roll the aircraft about its own velocity vector, as opposed to the body axis. The roll-yaw stability augmentation system is sufficient for the majority of aircraft, but a more refined lateral-directional control augmentation system is necessary for the aircraft that must maneuver swiftly at high AOA. At high alpha, the lateral aerodynamic control surfaces have a tendency to induce the aircraft to roll about its longitudinal axis, which may result in extremely unfavorable phenomena such as the kinematic coupling of alpha and beta. The primary function of a roll is to initiate a turn, which is accomplished by utilizing the AOA to generate the lift that will eventually produce the necessary centripetal acceleration. Kinematic coupling creates a sideslip, known as an unfavorable sideslip, because it tends to counter the roll. Large AOS are undesirable for numerous important reasons. Therefore, the effectiveness of the aerodynamic control surfaces may be drastically diminished, and directional stability may be lost. Even if directional stability is maintained, a substantial side force may be generated, which may cause the vertical tail to break. During a roll, inertia coupling is another significant consequence.

4.2.1 Performance Specifications

The interconnection shown in Fig. 4.5 is considered for control design. The aileron, rudder, and morphing actuator are modeled as first-order systems,

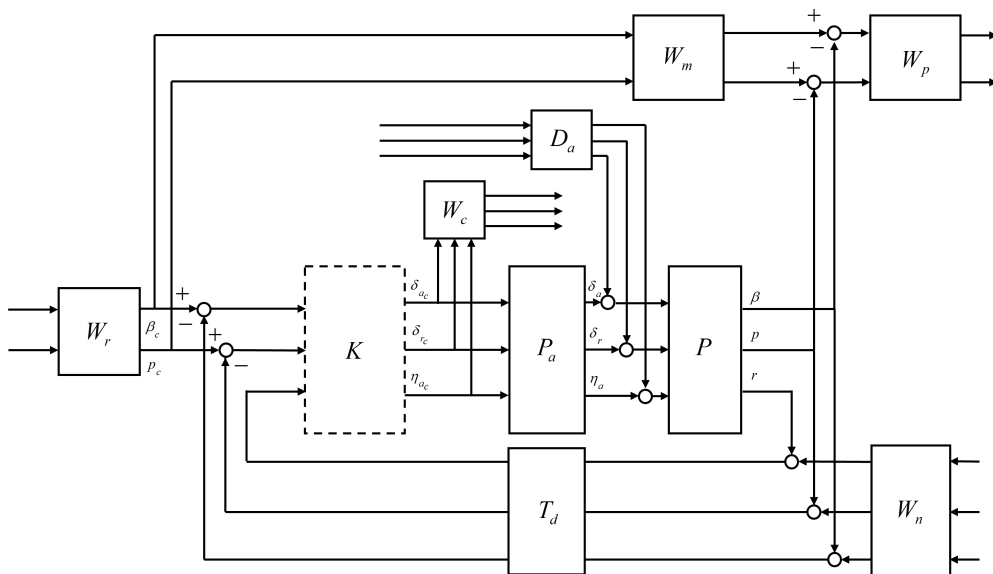


Figure 4.5 Closed-loop interconnection of the lateral-directional CAS.

where the bandwidth is set to 5 Hz for the conventional control surfaces and 0.5 Hz for the morphing actuator to address a relatively slow response of the morphing actuators. Except for some highly agile maneuvers, in most cases, the AOS and the roll rate command do not exceed 3 deg and 10 deg/s, respectively. The ideal model for the AOS response to the command is set to have a natural frequency of 2 rad/s and a damping ratio of 0.8 to allow for some overshoot. The ideal model for the roll rate response to the command is set to have a natural frequency of 10 rad/s and a damping ratio of 0.8 to allow for faster convergence. Performance weights are set such that the model matching error does not exceed two times the corresponding measurement noise level at low frequencies. The sensor measurement error is modeled as white Gaussian noise, and the standard deviation is set to match the sensor specifications of the GTM. In the actuator models, disturbance of 0.01 deg is added below 0.5 rad/s to account for errors due to dead zone, saturation, rate limit, and additional uncertainties arising from complex morphing mechanisms. A first-order Padé approximant corresponding to a transport delay of 30 ms is applied to all sensor measurements. The weighting filters are summarized in Table 4.3.

4.2.2 Controller Synthesis and Analysis

The LPV controller and the \mathcal{H}_∞ controller are synthesized. The open-loop and closed-loop Bode gain plot is shown in Fig. 4.6. It is noted that the AOS performance of the two controllers is similar, while the \mathcal{H}_∞ controller exhibits a faster roll rate response. The step response shown in Figs. 4.8-4.11 confirms the observation.

Table 4.3 Weighting filters for the lateral-directional CAS design.

Weighting Filter	Value
P_{a_a}	$\frac{31.42}{s+31.42}$
P_{a_r}	$\frac{31.42}{s+31.42}$
P_{a_m}	$\frac{3.142}{s+3.142}$
W_{r_β}	$3 \cdot 0.1745$
W_{r_p}	$10 \cdot 0.1745$
W_{m_β}	$\frac{2^2}{s^2+2 \cdot 0.8 \cdot 2s+2^2}$
W_{m_p}	$\frac{10^2}{s^2+2 \cdot 0.8 \cdot 10s+10^2}$
W_{p_β}	$\frac{2 \cdot 0.033 \cdot 0.1745 \cdot (s/120+1)}{s/0.1+1}$
W_{p_p}	$\frac{2 \cdot 0.5220 \cdot 0.1745 \cdot (s/120+1)}{s/0.1+1}$
W_{n_β}	$0.033 \cdot 0.1745$
W_{n_p}	$0.5220 \cdot 0.1745$
W_{n_r}	$0.3330 \cdot 0.1745$
W_{c_a}	$\frac{0.0001(s/0.1+1)}{s/120+1}$
W_{c_r}	$\frac{0.0005(s/0.1+1)}{s/120+1}$
W_{c_m}	$\frac{0.01(s/0.1+1)}{s/120+1}$
D_a	$\left(\frac{0.01}{s/0.5+1} \right) I_3$
T_d	$\left(\frac{-s+66.67}{s+66.67} \right) I_3$

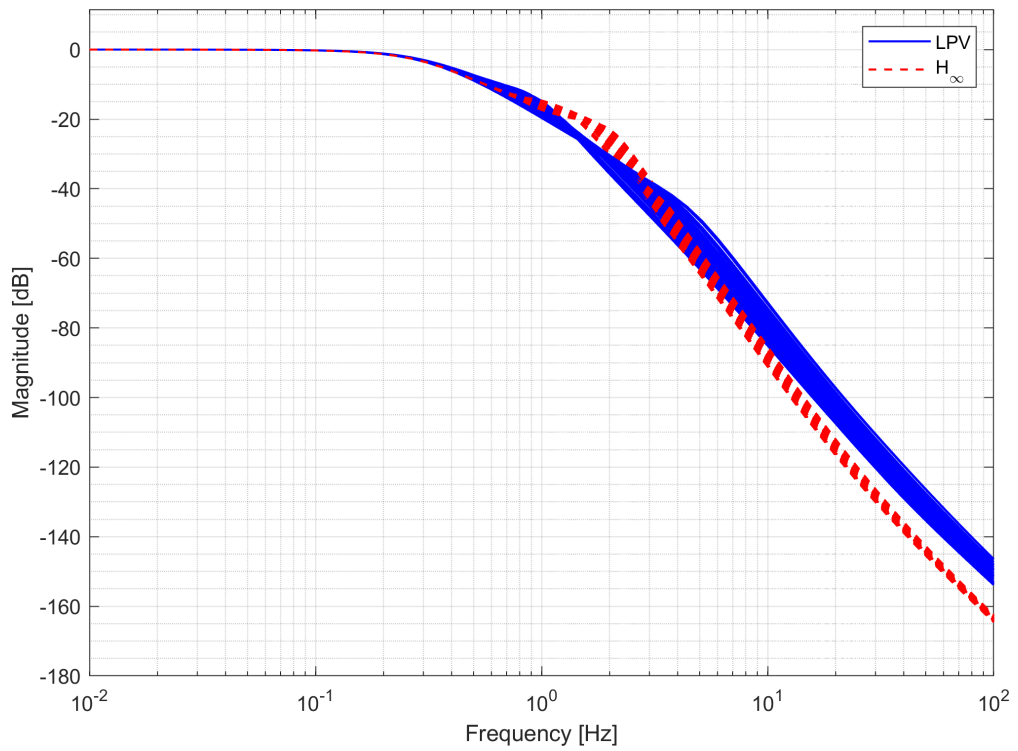


Figure 4.6 Bode magnitude plot of the lateral-directional CAS - angle of sideslip.

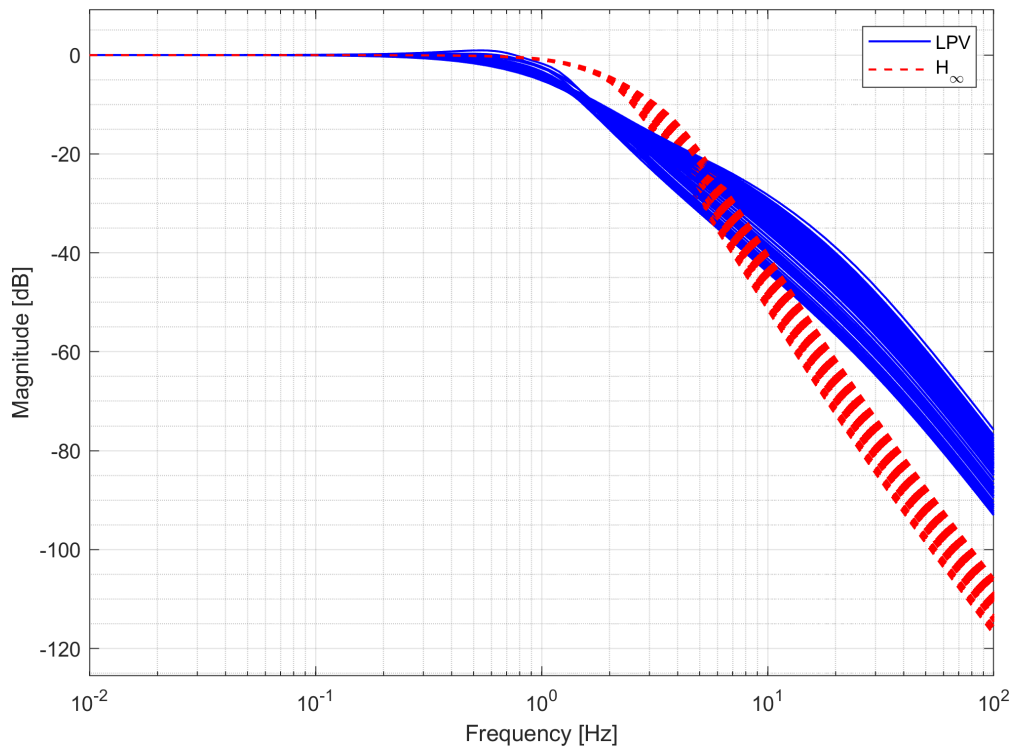


Figure 4.7 Bode magnitude plot of the lateral-directional CAS - roll rate.

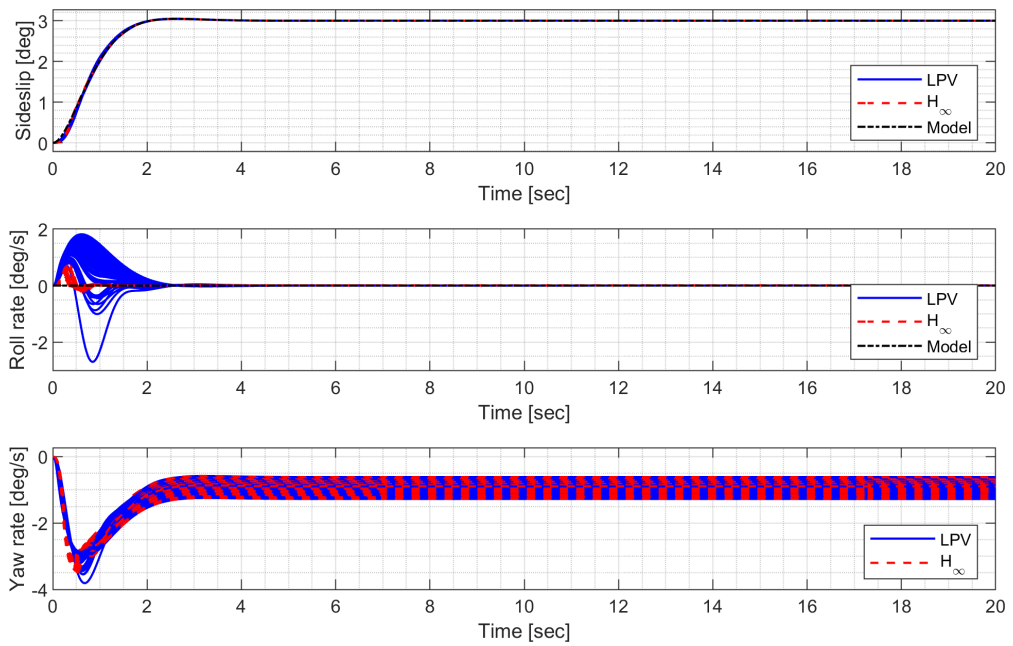


Figure 4.8 State response to the angle of sideslip step command.

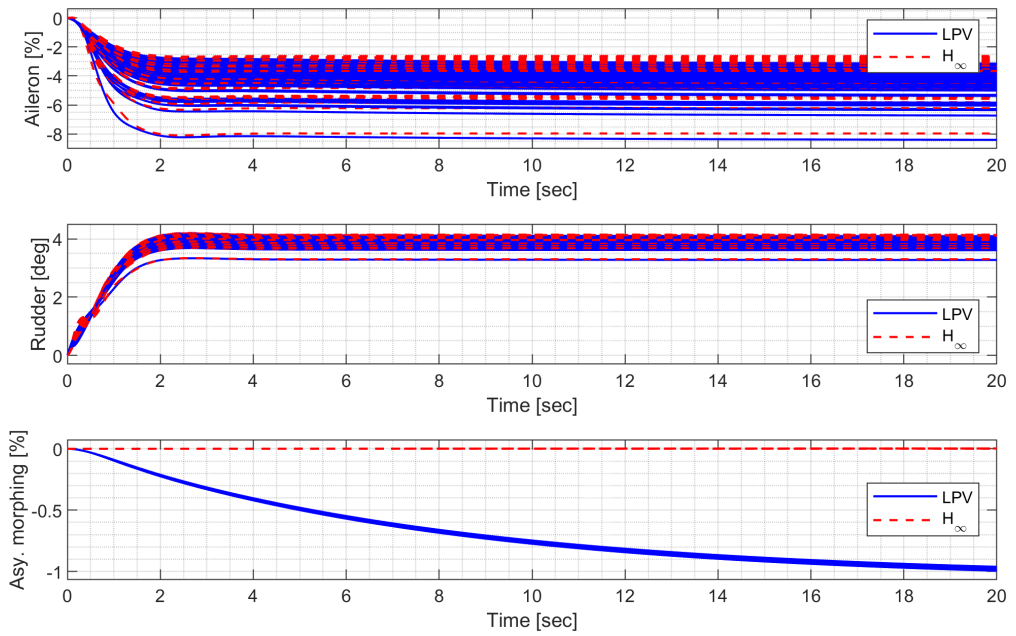


Figure 4.9 Input response to the angle of sideslip step command.

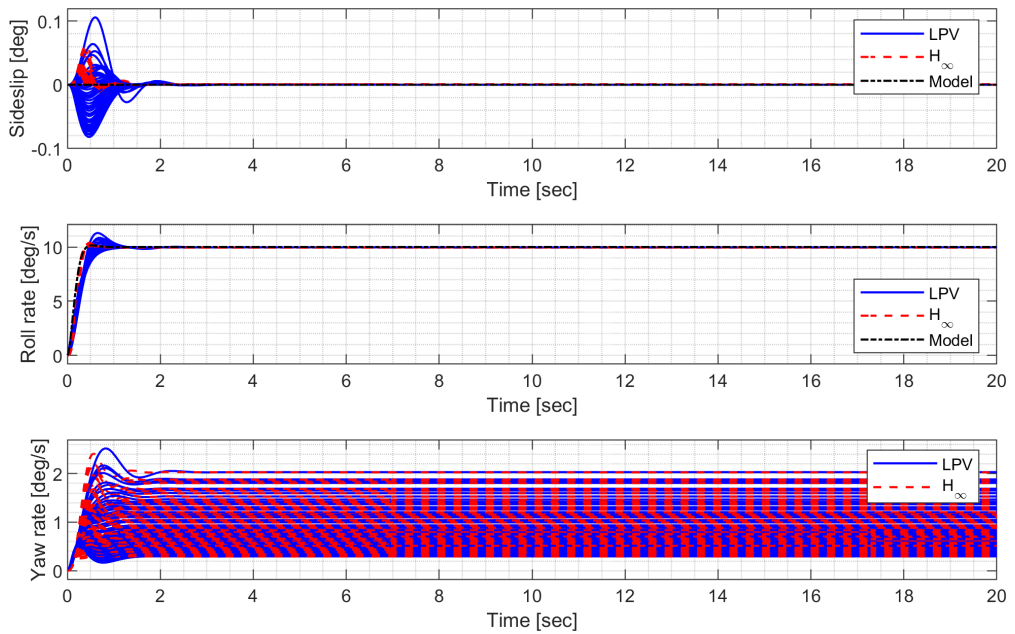


Figure 4.10 State response to the roll rate step command.

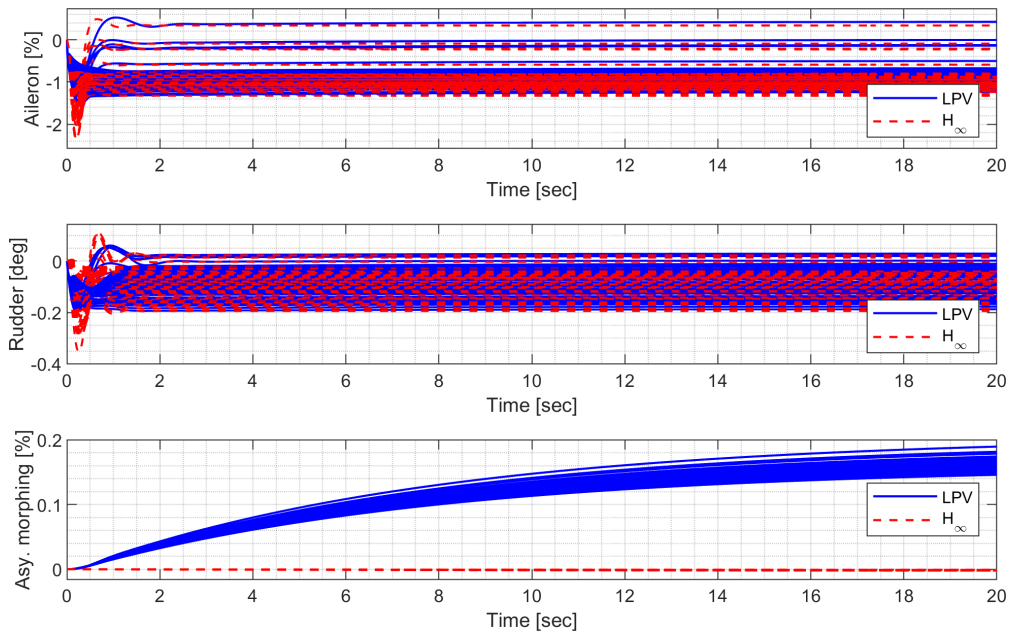


Figure 4.11 Input response to the roll rate step command.

4.3 Span Morphing Strategy

The remaining degree of freedom in the morphing parameter can be used for morphing-assisted maneuvers. In this section, the impacts of span morphing on various aspects are discussed.

4.3.1 Effects of Span Morphing

Wing span is one of the most important geometrical elements in airplane design. It is directly related to the lift-induced drag of the wing; as an increasing fraction of the inboard wing, airfoils behave as though in two-dimensional flow conditions as the span grows. Due to the increased distance between the vortices and the wing sections at the root, the downwash caused by the wing tip vortices in the inboard area of the wing is reduced. Additionally, the influence on maneuverability must be considered. If the lift near the wing tips can be adjusted, increasing the span causes a rise in rolling MOI and rolling moment production. Significant variations in the lift pitching moment and position of the aircraft's center of mass can be anticipated if the wing is swept, altering trim conditions and stability. With span morphing, both the span and lifting area of the wing are changed. Therefore, the wing varies not only AR, which affects the induced drag, but also the wetted area, which affects the profile drag. For increasing C_L values, setups with a larger span may not only offer more lift but also less drag due to lower AOA requirements and less induced drag. An increase in wing span reduces the MAC for the same wing area, hence improving the AR. Increasing AR has an effect on the coefficient of produced drag. Reducing the MAC decreases the local Reynolds number of the wing's airfoils, hence increasing their local base drag coefficient. At low Reynolds numbers, the

significance of this effect increases. While the local base drag coefficient may increase, the actual local drag lowers because of the shorter wing chord and length for boundary layer growth. This small reduction in base drag is counterbalanced by the need for a longer span to maintain wing area, rendering the effect of the span increase on the base drag virtually null, at least for sufficiently high Reynolds numbers. Therefore, wing span predominantly affects total wing drag because of its effect on induced drag. To maximize the lift-to-drag ratio of the wing throughout the flight envelope, one can expect more aerodynamic gains from expanding the wing span for operating at high C_L values, i.e., at slower flying speeds.

An increase in span has further effects on stability and control. The first and most obvious result is an increase in rolling MOI. Due to the fact that the rolling MOI is proportional to the square of the distance between the mass elements and the longitudinal axis of the aircraft, there is a quadratic rise with a span. Therefore, if it is not possible to reduce the wing's structural mass toward the tips, even if the device generating the rolling moment stays close to the wing tip, large reductions in the achievable roll rate can be anticipated. Unless the device's span is expanded, the rolling moment varies linearly with the distance from the aircraft's longitudinal axis, which results in less maneuverability. Increased aerodynamic damping of the rolling motion due to higher wingtip speed also contributes to the loss of maneuverability, which in turn increases rolling stability. If the wing is swept, an increase in the span is likely to induce a change in the aircraft's center of gravity, which will become more noticeable as the wing's structure mass grows in relation to the aircraft's mass. The position of the wing's aerodynamic center is also modified. In turn, trim drag and

static stability margin are affected by the changes in center of gravity (CG) and aerodynamic center (AC). Similarly, if the span is raised asymmetrically, the CG and AC will move off of the symmetry plane of the airplane, and there will be a stronger coupling between the longitudinal and lateral movements as the aircraft becomes more asymmetric.

When the span is increased while the wing area is maintained (i.e., by increasing the AR), two primary structural effects are observed: The chord reduction increases the wing root bending moment and decreases the airfoil sections' maximum thickness along the span.

4.3.2 Criteria for Span Variation

For improved agility and maneuverability, the symmetric morphing parameter should be increased when the normal acceleration command is large, and the symmetric morphing parameter should be decreased when the roll rate command is large.

4.4 Nonlinear Simulation of Morphing-Assisted Maneuvers

In this section, numerical simulation results are presented.

4.4.1 High-Fidelity Flight Dynamics Simulator

The GTM program shown in Fig. 4.12 is used to simulate a transport aircraft's flight dynamics. It implements general equations of motion for rigid bodies for the vehicle dynamics and derives aerodynamic forces using a standard coefficient expansion performed as table lookups. The dynamics of actuator servos and sensor bandwidth and errors are also included as shown in Fig. 4.13.

4.4.2 Push-over and Pull-up

Push-over and pull-up is considered. Normal acceleration command $0g$ is engaged for the first 5 seconds; then, the $4g$ command is engaged. The throttle is fixed to 90% throughout the flight. Figures 4.14-4.17 show the result using LPV controller, and Figs. 4.18-4.21 show the result using \mathcal{H}_∞ controller. In case 1, the aircraft performs push over with the span shortened, then pulls up with the span extended, and in case 2, the span is controlled in the opposite way. It is shown that both aircraft perform well before going into the stall, but the configuration profile in case 1 is superior in maintaining pull-up longer. It is also noted that the normal acceleration tracking performance of the \mathcal{H}_∞ controller degrades when the morphing configuration changes rapidly while the LPV controller shows faster convergence to the command. However, the LPV-based CAS results in a larger roll angle because the CAS only tries to control the roll rate instead of the roll angle, which can be improved by implementing

GTM Design-Simulation Model
 Release 13-08
 Last modified by decox on Fri Aug 02 06:39:05 2019
 Copyright 2009
 United States Government as represented by the
 Administrator of the National and Aeronautics and Space Administration.
 No copyright is claimed in the United States under Title 17, U.S. Code.
 All Other Rights Reserved.

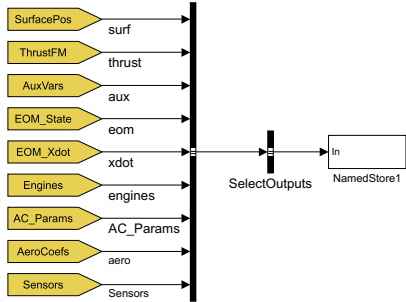
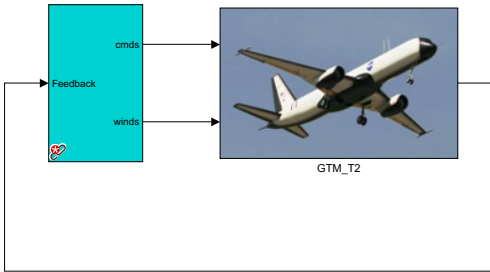


Figure 4.12 GTM flight dynamics simulator.

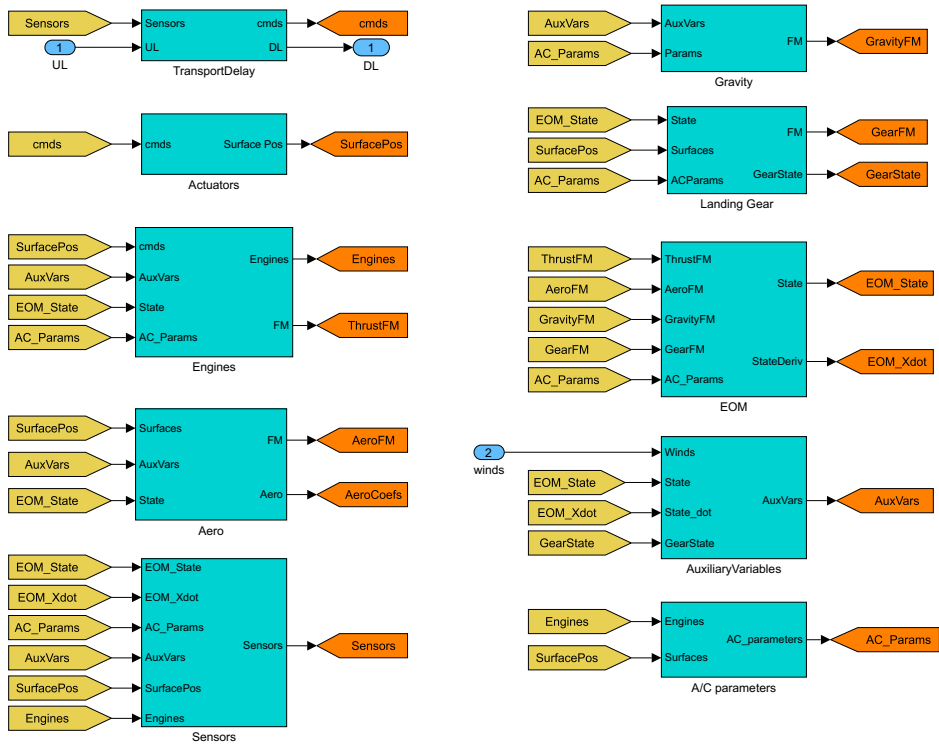


Figure 4.13 Building blocks of GTM.

a roll angle autopilot. The simulation results for the \mathcal{H}_2 controller are omitted because the results are very similar to those for the \mathcal{H}_∞ controller.

4.4.3 High-g Turn

High-g turn is considered. Roll rate command 10 deg/s is engaged for the first 8 seconds to reach 80 deg roll angle; then 0 deg/s commands is engaged. Normal acceleration command 1g is engaged for the first 8 seconds; then the 5g command is engaged. The throttle is fixed to the maximum throughout the flight. In case 1, the aircraft rotates on the roll axis with the span shortened, then increases the span and increases the normal acceleration to make a high-g turn. In case 2, the span is controlled in the opposite way. It is shown in Figs. 4.22-4.31 that both aircraft perform well before going into the stall, but one configuration profile in case 1 is superior in maintaining turn longer. Note that the LPV controller is quicker in convergence, but the \mathcal{H}_∞ controller is better at maintaining the command longer where the configuration is not changed.

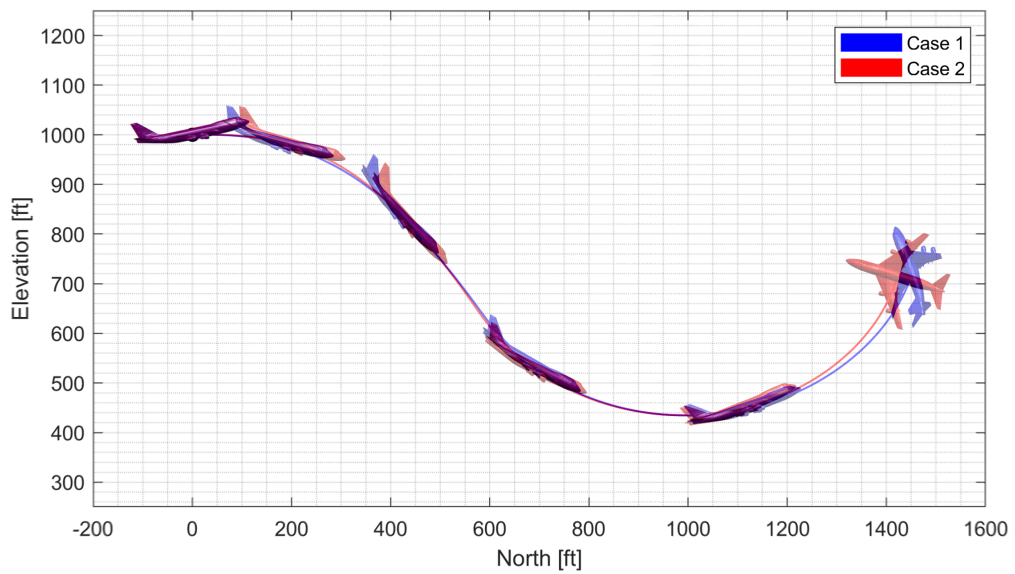


Figure 4.14 Flight trajectory of the push-over and pull-up - LPV.

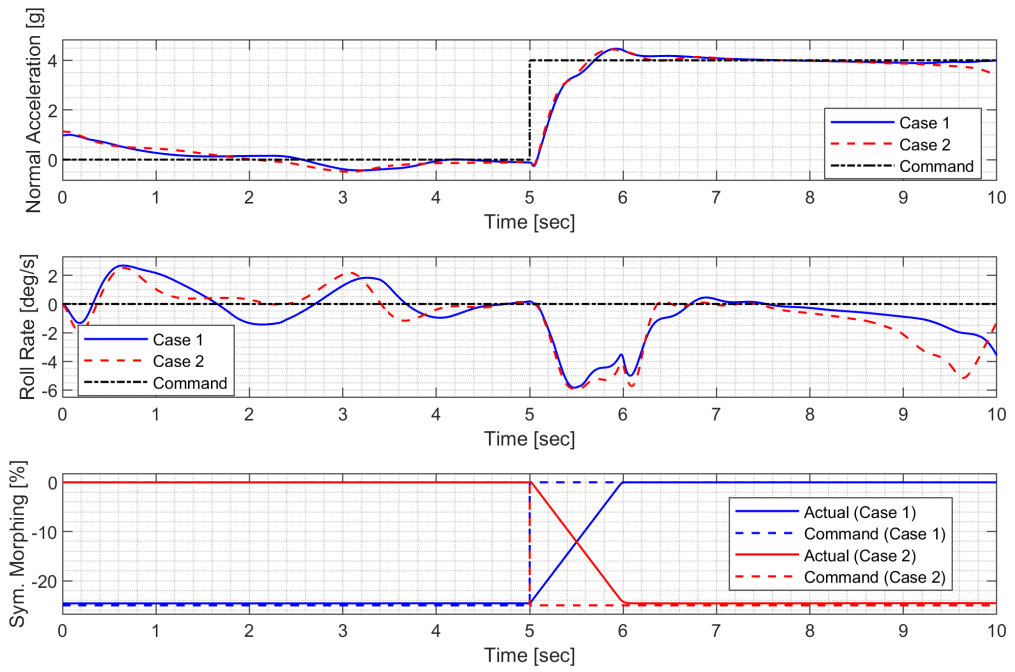


Figure 4.15 Controlled states and symmetric morphing parameter history for the push-over and pull-up - LPV.

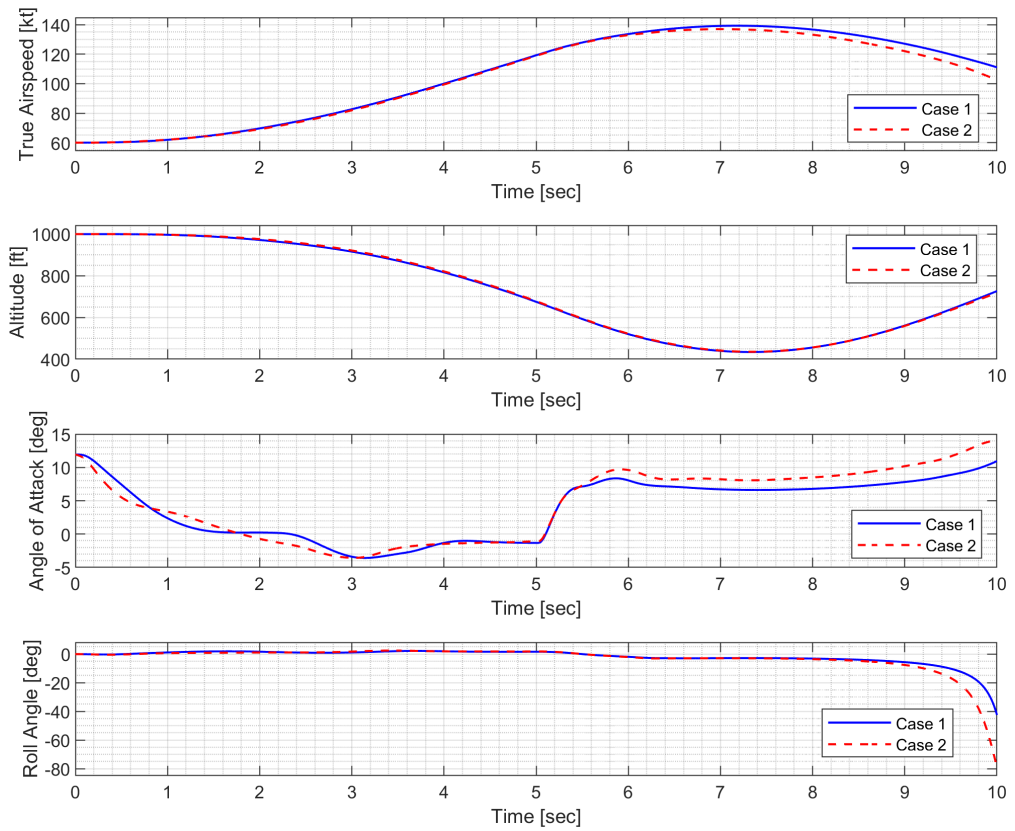


Figure 4.16 State history for the push-over and pull-up - LPV.

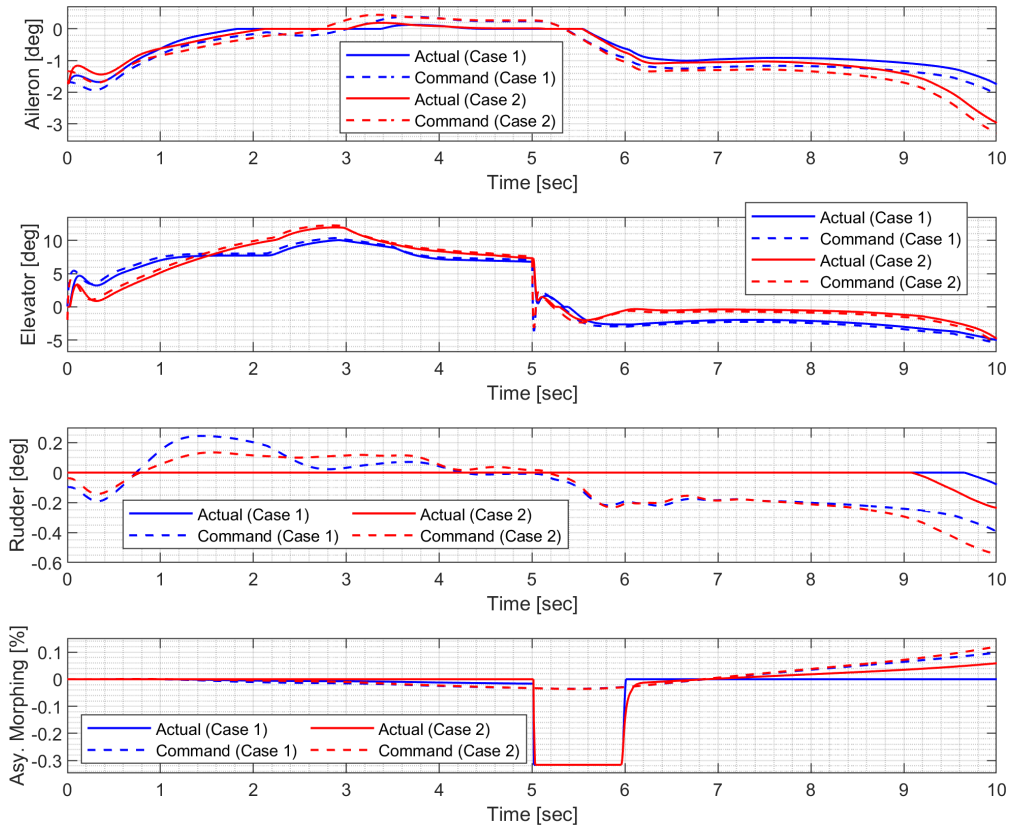


Figure 4.17 Input history of the push-over and pull-up - LPV.

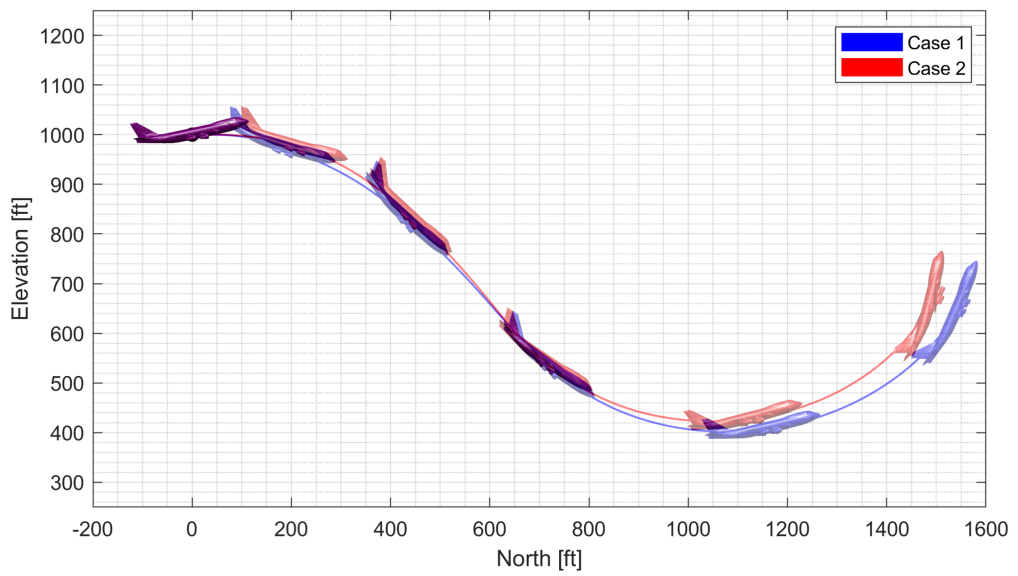


Figure 4.18 Flight trajectory of the push-over and pull-up - \mathcal{H}_∞ .

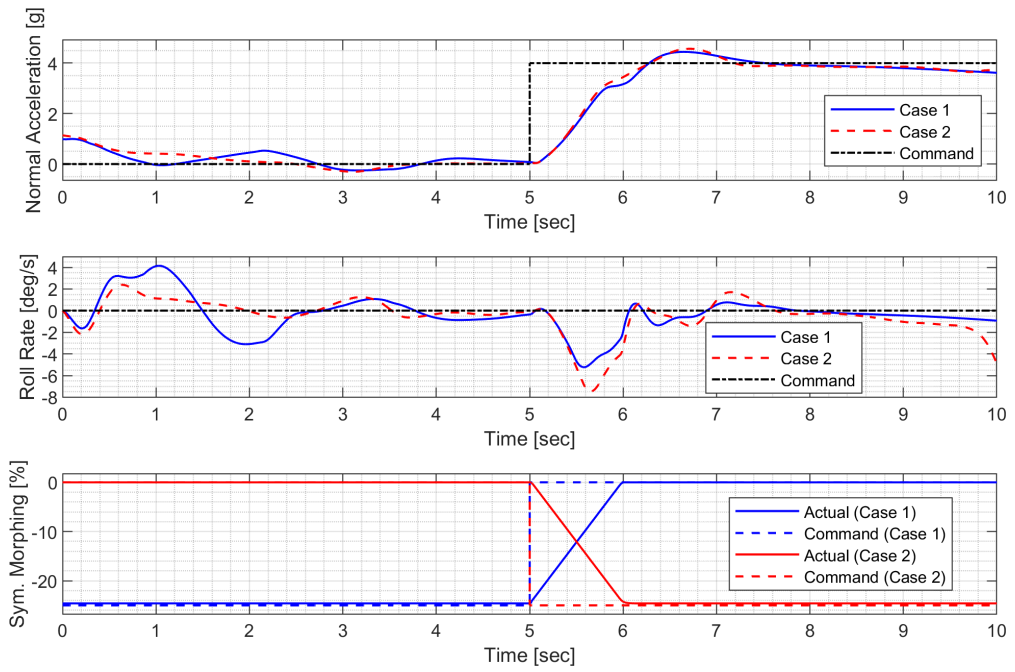


Figure 4.19 Controlled states and symmetric morphing parameter history for the push-over and pull-up - \mathcal{H}_∞ .

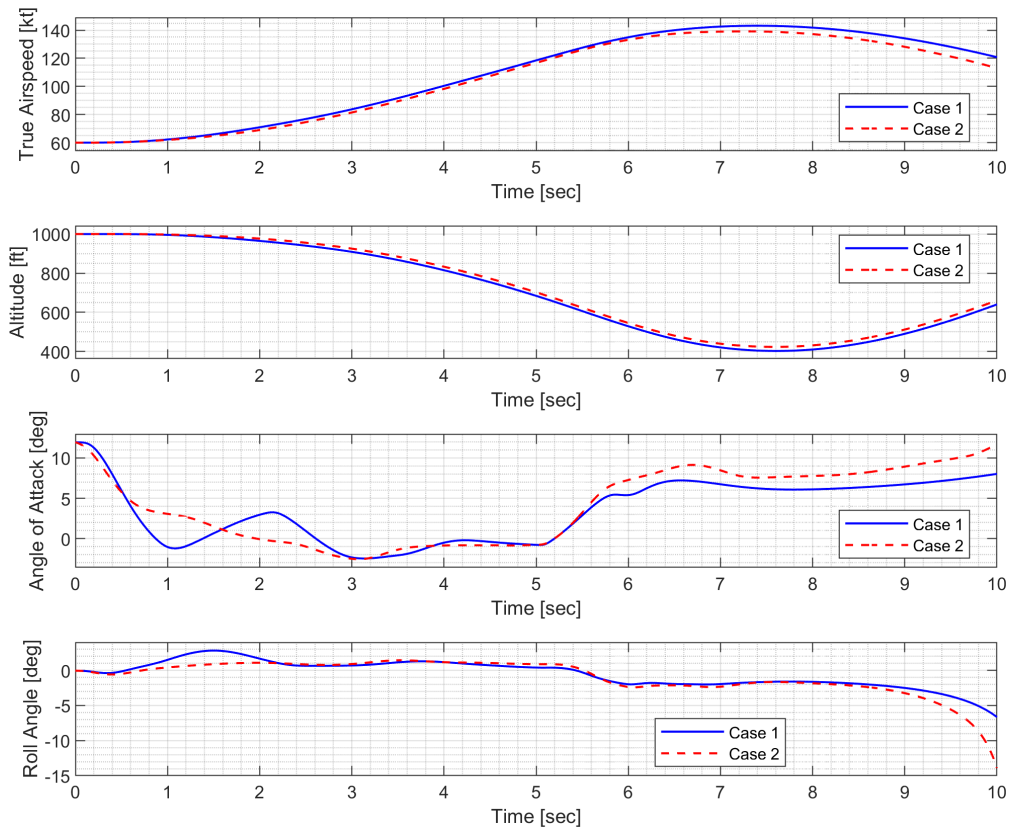


Figure 4.20 State history for the push-over and pull-up - \mathcal{H}_∞ .

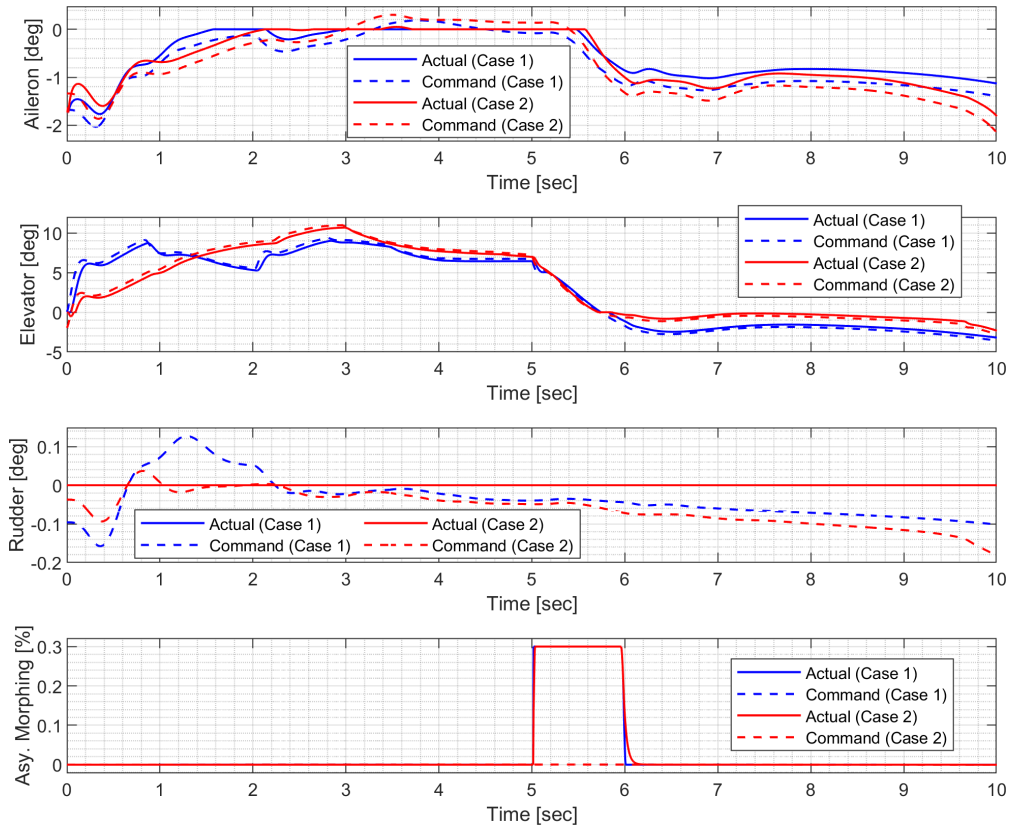


Figure 4.21 Input history of the push-over and pull-up - \mathcal{H}_∞ .

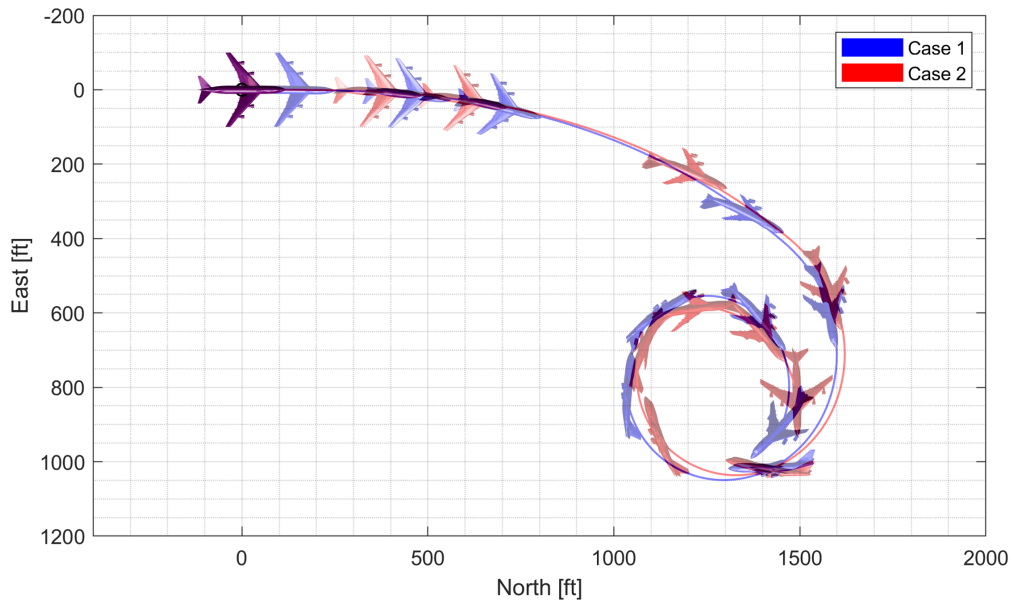


Figure 4.22 Flight trajectory of the high-g turn (top view) - LPV.

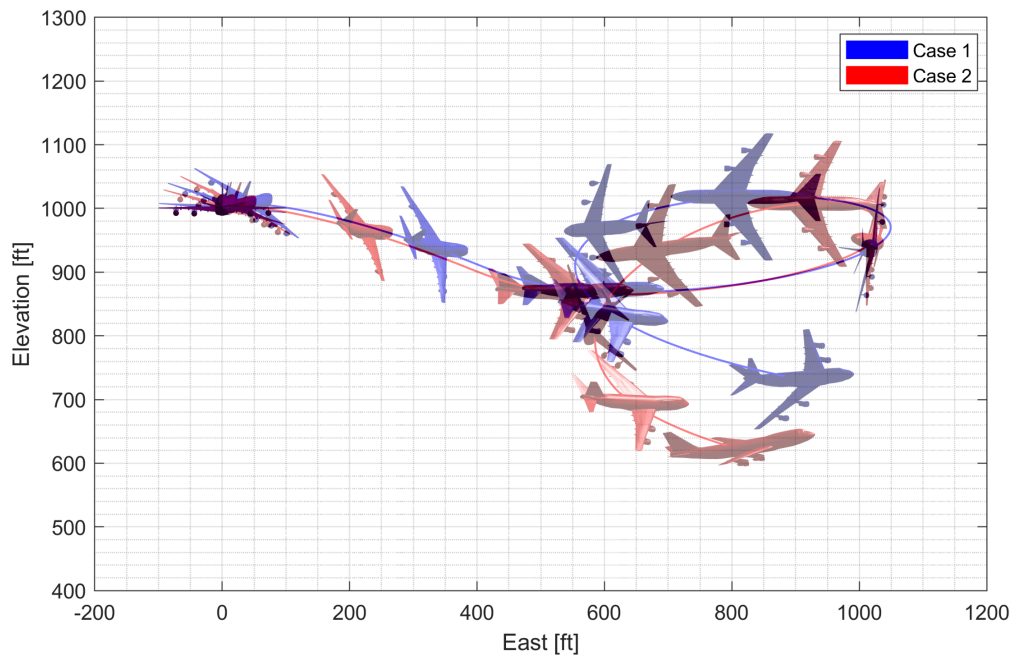


Figure 4.23 Flight trajectory of the high-g turn (side view) - LPV.

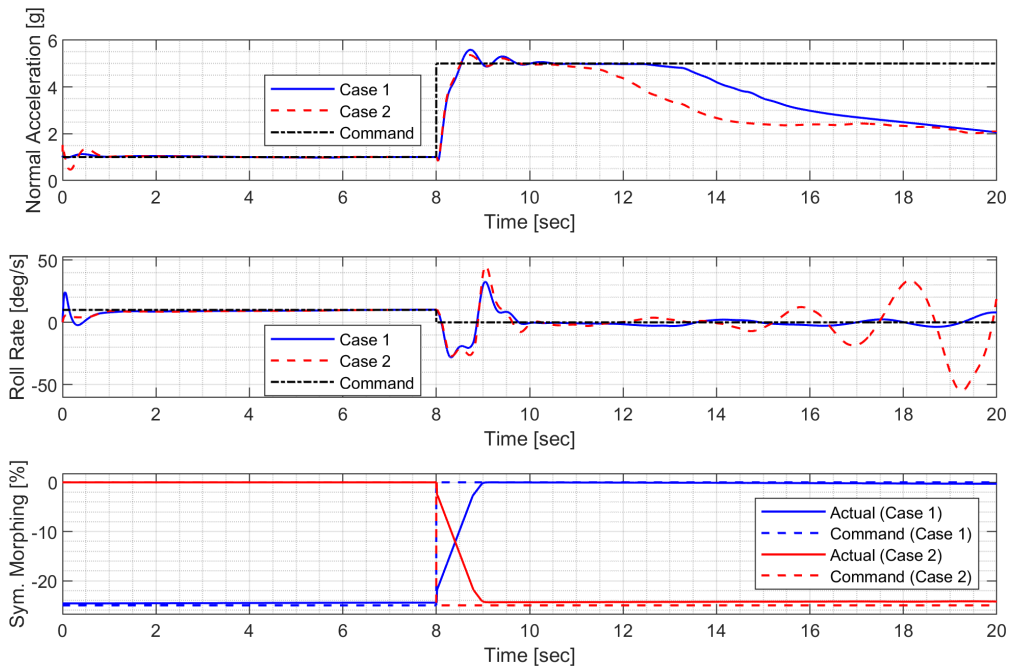


Figure 4.24 Controlled states and symmetric morphing parameter history for the high-g turn - LPV.

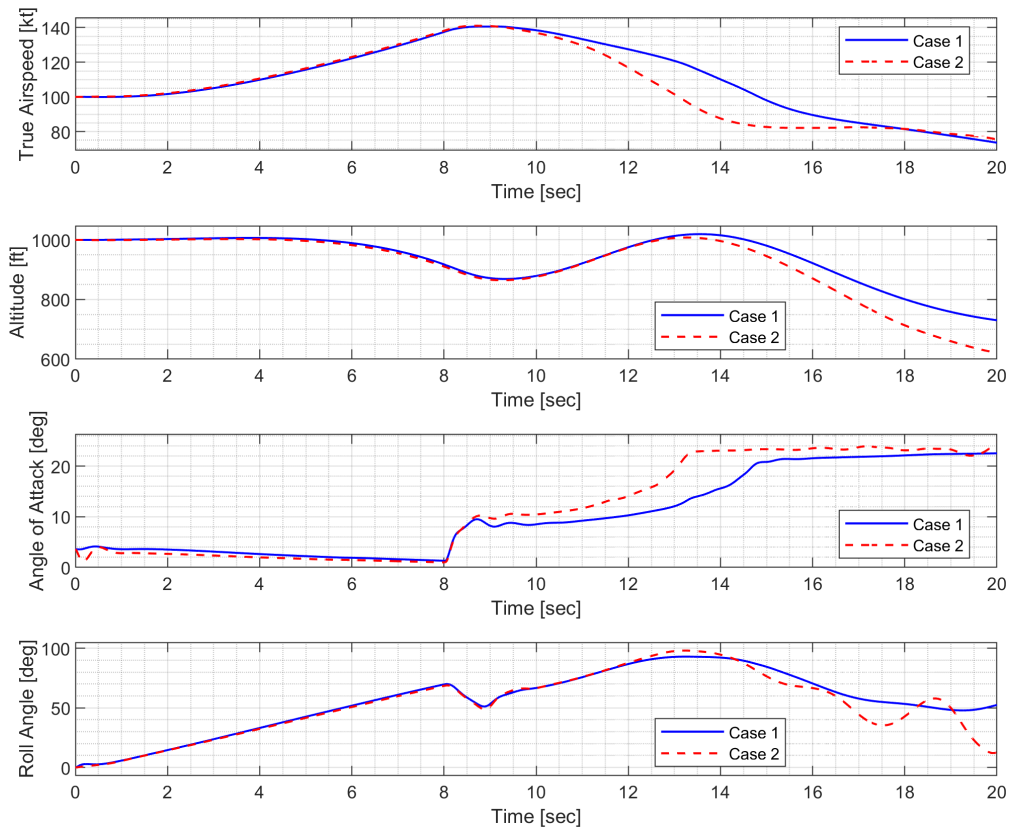


Figure 4.25 State history of the high-g turn - LPV.

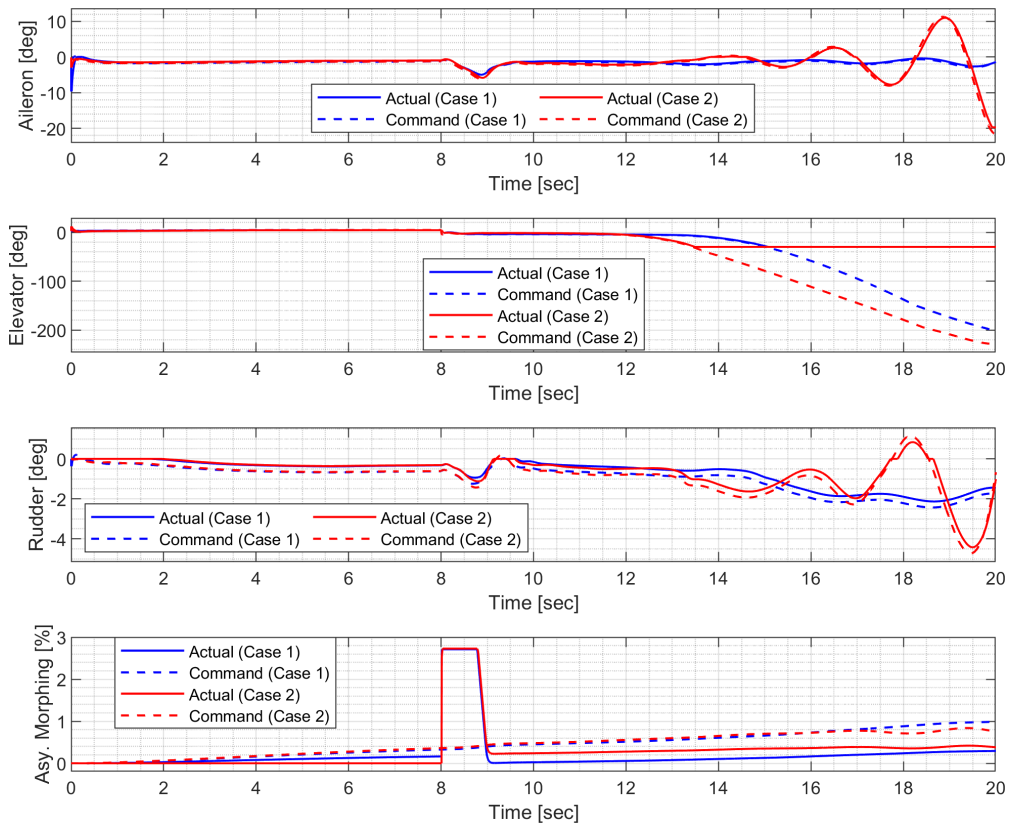


Figure 4.26 Input history of the high-g turn - LPV.

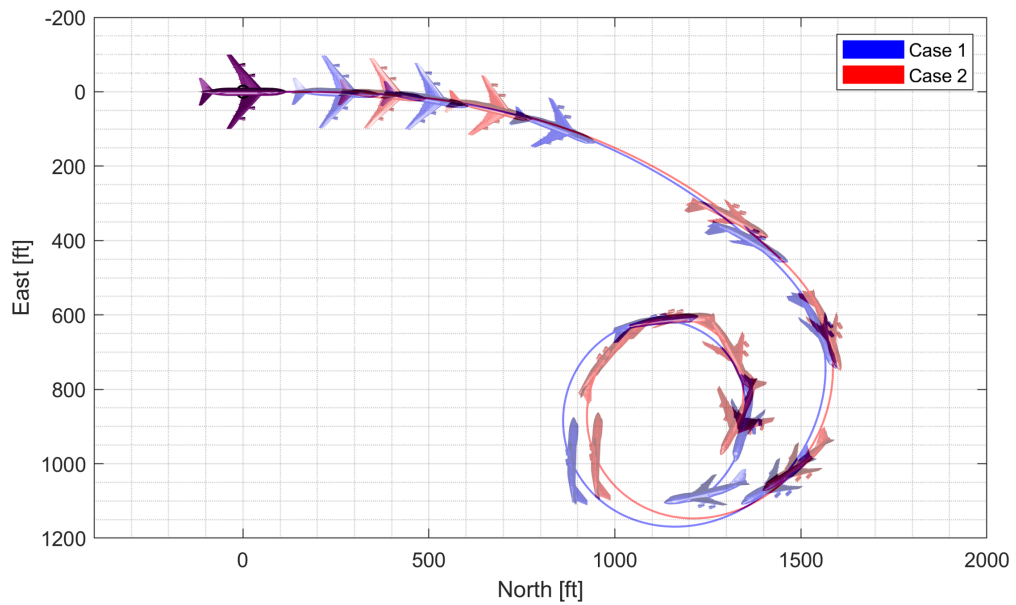


Figure 4.27 Flight trajectory of the high-g turn (top view) - \mathcal{H}_∞ .

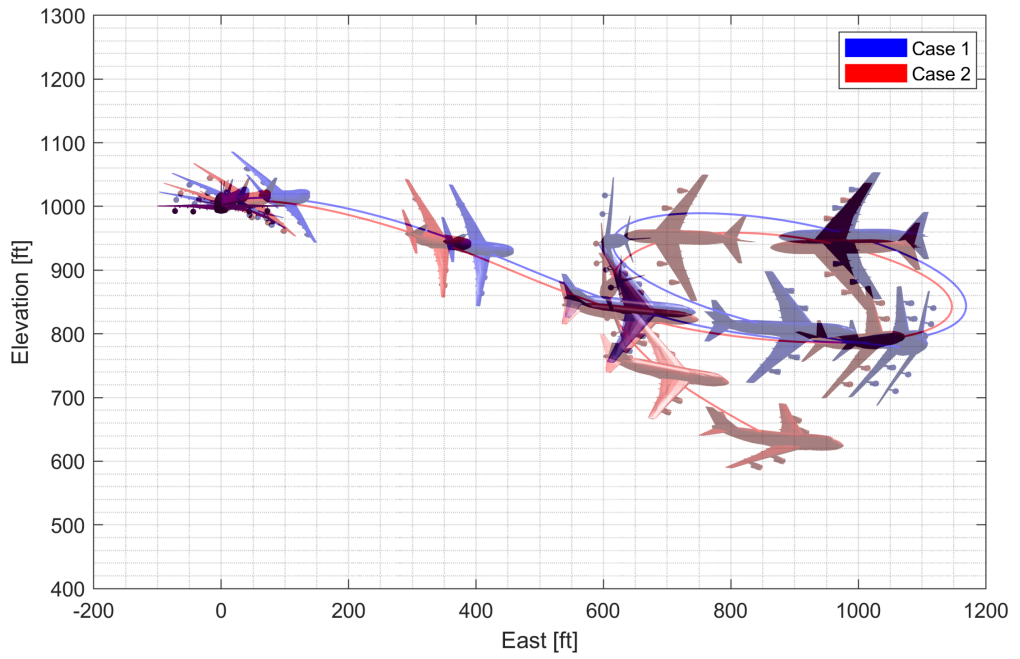


Figure 4.28 Flight trajectory of the high-g turn (side view) - \mathcal{H}_∞ .

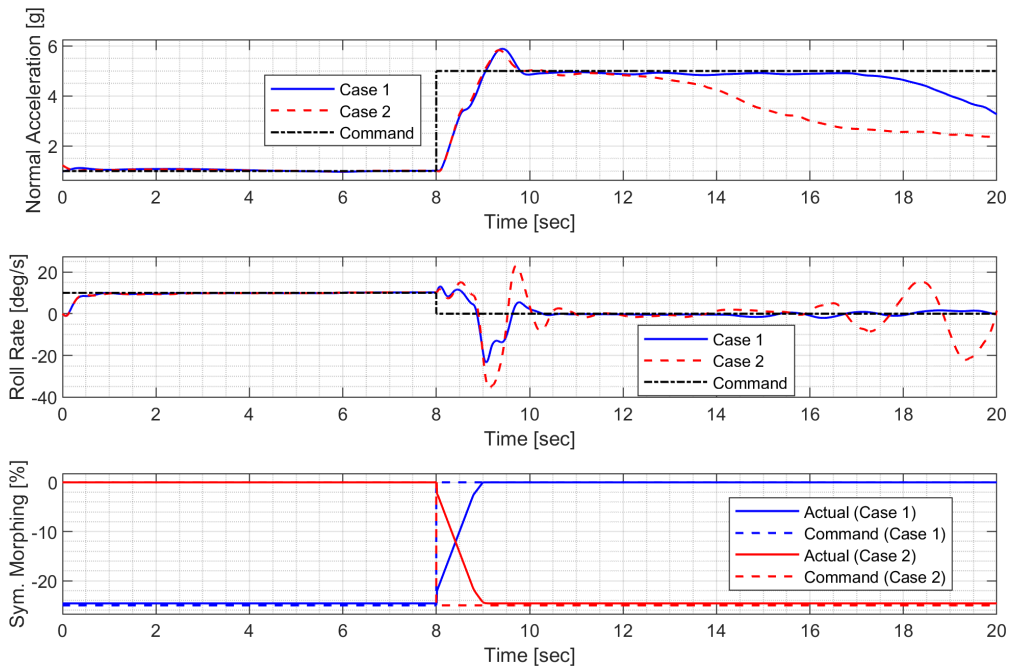


Figure 4.29 Controlled states and symmetric morphing parameter history for the high-g turn - \mathcal{H}_∞ .

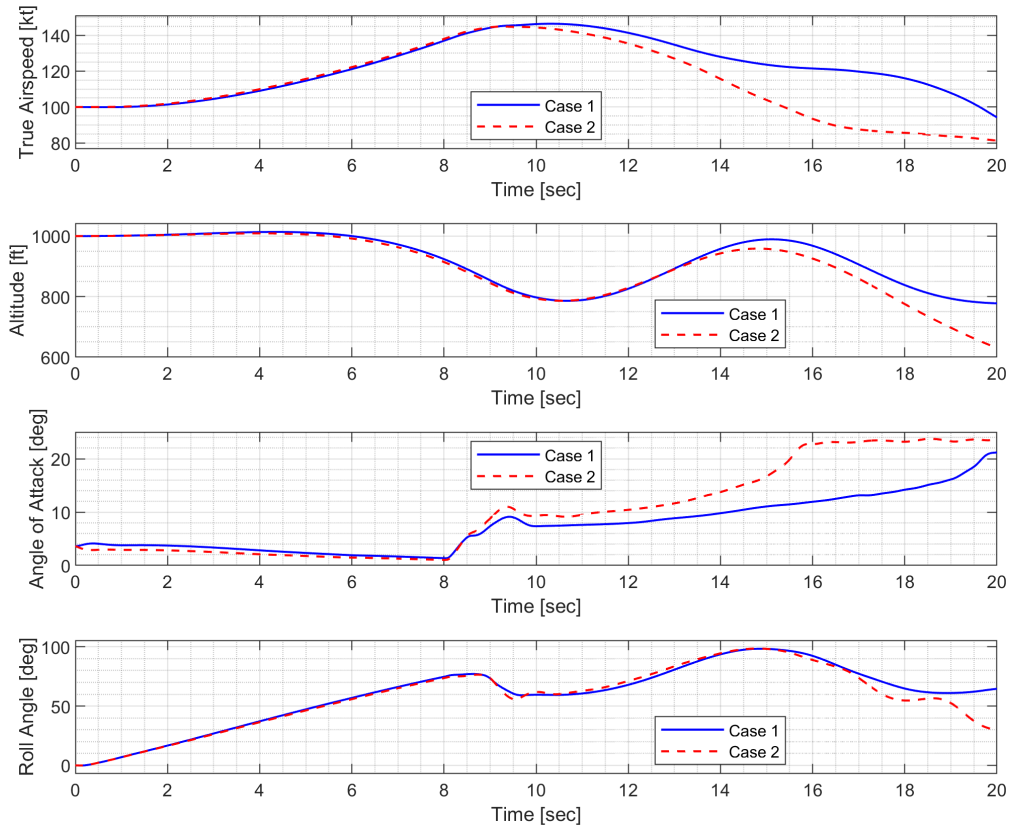


Figure 4.30 State history of the high-g turn - \mathcal{H}_∞ .

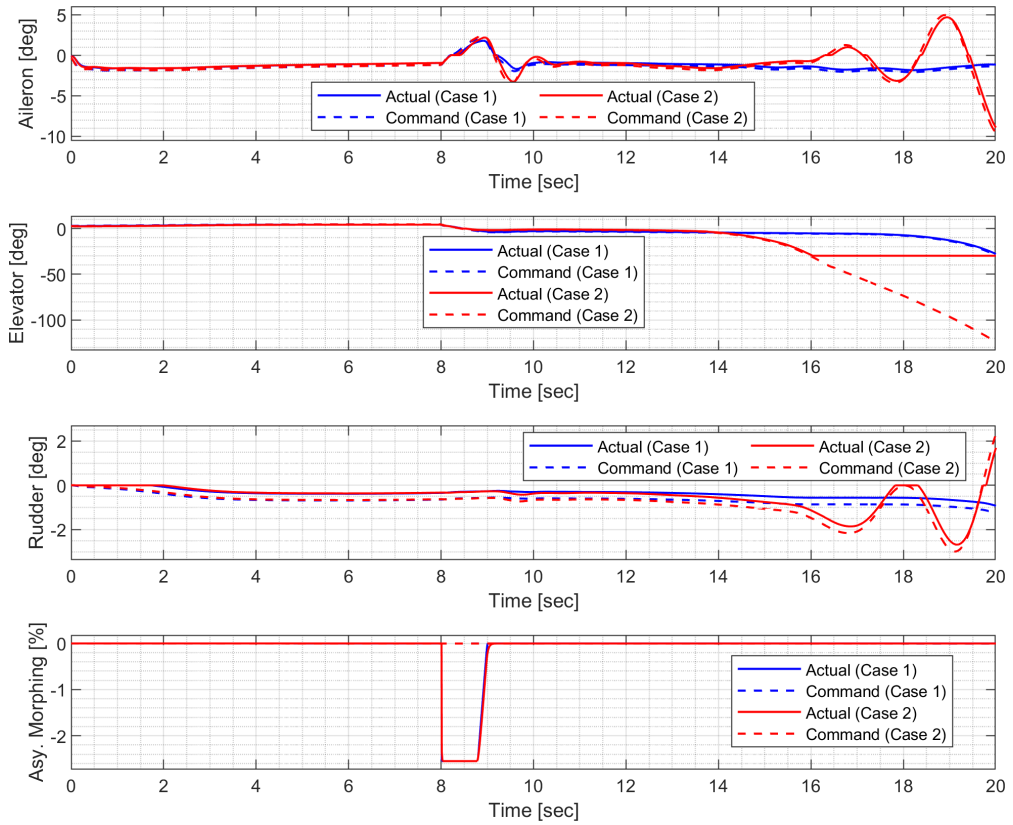


Figure 4.31 Input history of the high-g turn - \mathcal{H}_∞ .

Chapter 5

Autopilot Design Based on LPV Methods for Morphing-Assisted Flights

UAV may complete an entire mission without manual remote control when flight management system including autopilots are engaged. Most flying quality requirements do not directly relate to the way that autopilots are designed. While placing less emphasis on dynamic response, pilot relief autopilot modes require that the autopilot meet standards for steady-state error and disturbance rejection. In order to prevent distracting or potentially dangerous transient motions, careful attention must also be paid to how the autopilot is turned on and off. For instance, a few hundred feet below the planned altitude, the altitude-hold autopilot cannot be used. An overly steep rise might happen if the engine's force was not increased, possibly resulting in a stall. Alternatively, it is necessary to build navigation-coupled autopilot modes with the proper dynamic reaction for their purpose. A wide-bandwidth random input must be tracked by an autopilot in autonomous terrain-following mode, for example, without experiencing considerable overshoot.

In this chapter, an autopilot is designed for a morphing-assisted flight of morphing UAVs based on LPV methods. A longitudinal autopilot is designed to

track the true airspeed and altitude commands. A lateral-directional autopilot is designed to track the AOS and the roll angle commands. The autopilot utilizes symmetric and asymmetric morphing for improved agility and maneuverability, respectively. Numerical simulation is performed to demonstrate the effectiveness of the proposed scheme.

5.1 Longitudinal Autopilot Design for Airspeed and Altitude Control

In this section, airspeed and altitude autopilot is designed for the control of longitudinal motion. Altitude hold is a vital pilot relief option that enables an aircraft to be maintained in accordance with air traffic control requirements in an air route corridor at a predetermined altitude. The pressure altitude, which is the altitude computed by the air data computer based on measurements of the external pressure, is typically what is meant by the term “perceived altitude.” A warning will be given if the deviation exceeds 100 feet in a modern passenger aircraft’s altitude hold, which typically keeps the aircraft well inside 200 feet. The speed-hold autopilot is typically used during ascent and descent. The throttles can be set to a rather high level of power during a climb, and the elevator will receive speed input to maintain a steady speed. While the speed will fluctuate depending on altitude, maintaining a constant speed will maximize fuel efficiency. Additionally, the descent will be performed at a steady speed, with the throttles set to almost idle. Both the throttle and the elevator will be utilized to maintain speed and height at the cruising altitude for effective cruising.

5.1.1 Performance Specifications

In longitudinal aircraft dynamics, there is a significant coupling between the two control inputs (engine throttle, elevator deflection angle) and the two main outputs (speed and altitude). The interconnection shown in Fig. 5.1 is considered for control design.

The engine lag is modeled as a second-order system with an NMP zero. The

reference weight is set to 4 kt for the true airspeed and 10 ft for the altitude. The ideal models for the true airspeed and altitude response to the command are set to have a natural frequency of 2 rad/s and a damping ratio of 0.8 for a gentle response. Performance weights are set such that the model matching error does not exceed two times the measurement noise levels at low frequencies. The sensor measurement error is modeled as white Gaussian noise, and the standard deviation is set to match the sensor specifications of the GTM. In the actuator model, a disturbance of 0.01 deg is added below 0.5 rad/s to account for various errors. The weighting filters are summarized in Table 5.1.

5.1.2 Controller Synthesis and Analysis

The LPV controller and the \mathcal{H}_∞ controller are synthesized. The open-loop and closed-loop Bode magnitude plots are shown in Figs. 5.2 and 5.3. It is noted that the true airspeed response of the \mathcal{H}_∞ is somewhat disturbed in the middle-frequency range, while the \mathcal{H}_∞ exhibits unity gains in the altitude response up to much higher frequency. The step responses are shown in Figs. 5.4-5.7. The same observation can be made from the step responses where both controllers show rather large differences from the ideal model.

Table 5.1 Weighting filters for the longitudinal autopilot design

Weighting Filter	Value
P_{at}	$\frac{-0.1474s+0.7314}{s^2+1.336s+0.7314}$
P_{ae}	$\frac{31.42}{s+31.42}$
$W_{r_{VT}}$	$4 \cdot 1.6878$
W_{r_h}	10
$W_{m_{VT}}$	$\frac{2^2}{s^2+2 \cdot 0.8 \cdot 2s+2^2}$
W_{m_h}	$\frac{2^2}{s^2+2 \cdot 0.8 \cdot 2s+2^2}$
$W_{p_{VT}}$	$\frac{2 \cdot 0.06 \cdot 1.6878(s/120+1)}{s/0.005+1}$
W_{p_h}	$\frac{2 \cdot 0.01 \cdot 3.2808(s/2.5+1)}{s/0.04+1}$
$W_{n_{VT}}$	$0.06 \cdot 1.6878$
W_{n_α}	$0.031 \cdot 0.1745$
W_{n_q}	$0.3857 \cdot 0.1745$
W_{n_θ}	$0.02 \cdot 0.1745$
W_{n_h}	$0.01 \cdot 3.2808$
W_{c_t}	$\frac{0.001(s/0.5+1)}{s/120+1}$
W_{c_e}	$\frac{0.001(s/0.5+1)}{s/120+1}$
D_a	$\left(\frac{0.01}{s/0.5+1} \right) I_2$
T_d	$\text{diag}\left(\frac{-s+66.67}{s+66.67}, \frac{-s+66.67}{s+66.67}, \frac{-s+66.67}{s+66.67}, \frac{-s+28.57}{s+28.57}, \frac{-s+28.57}{s+28.57} \right)$

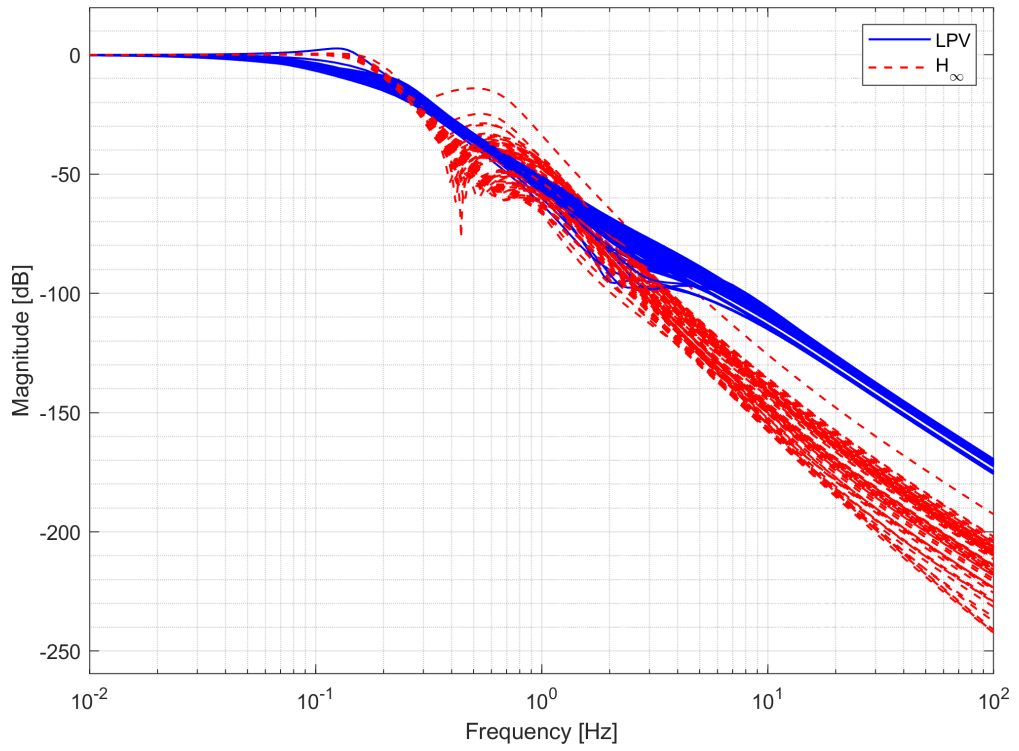


Figure 5.2 Bode magnitude plot for the longitudinal autopilot - true airspeed.

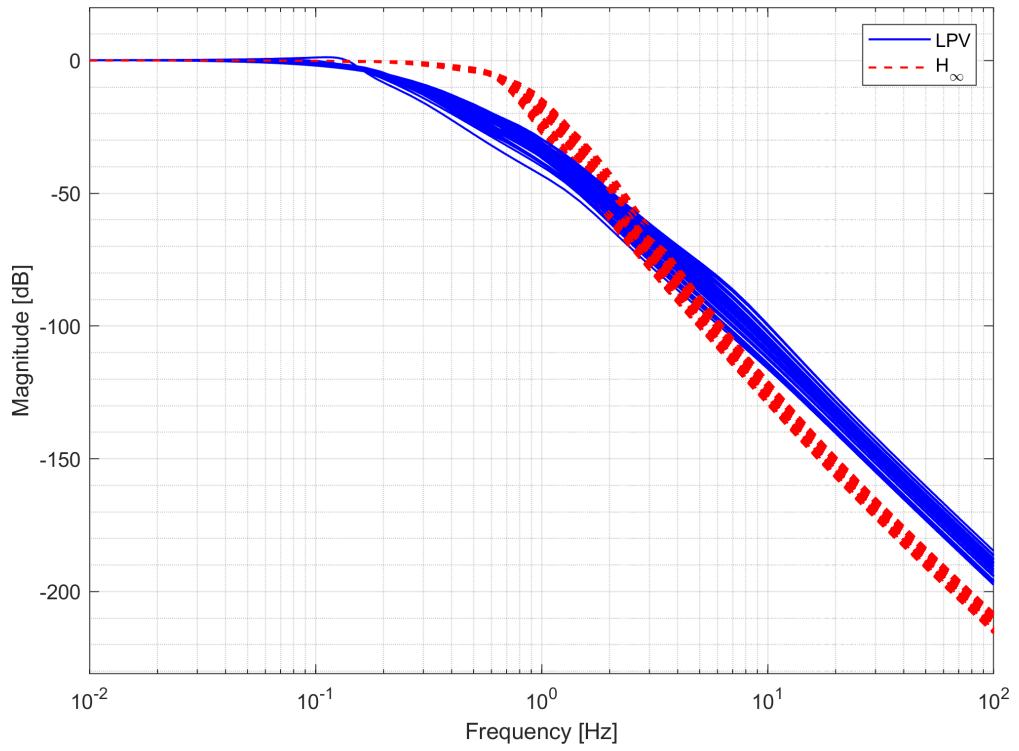


Figure 5.3 Bode magnitude plot for the longitudinal autopilot - altitude.

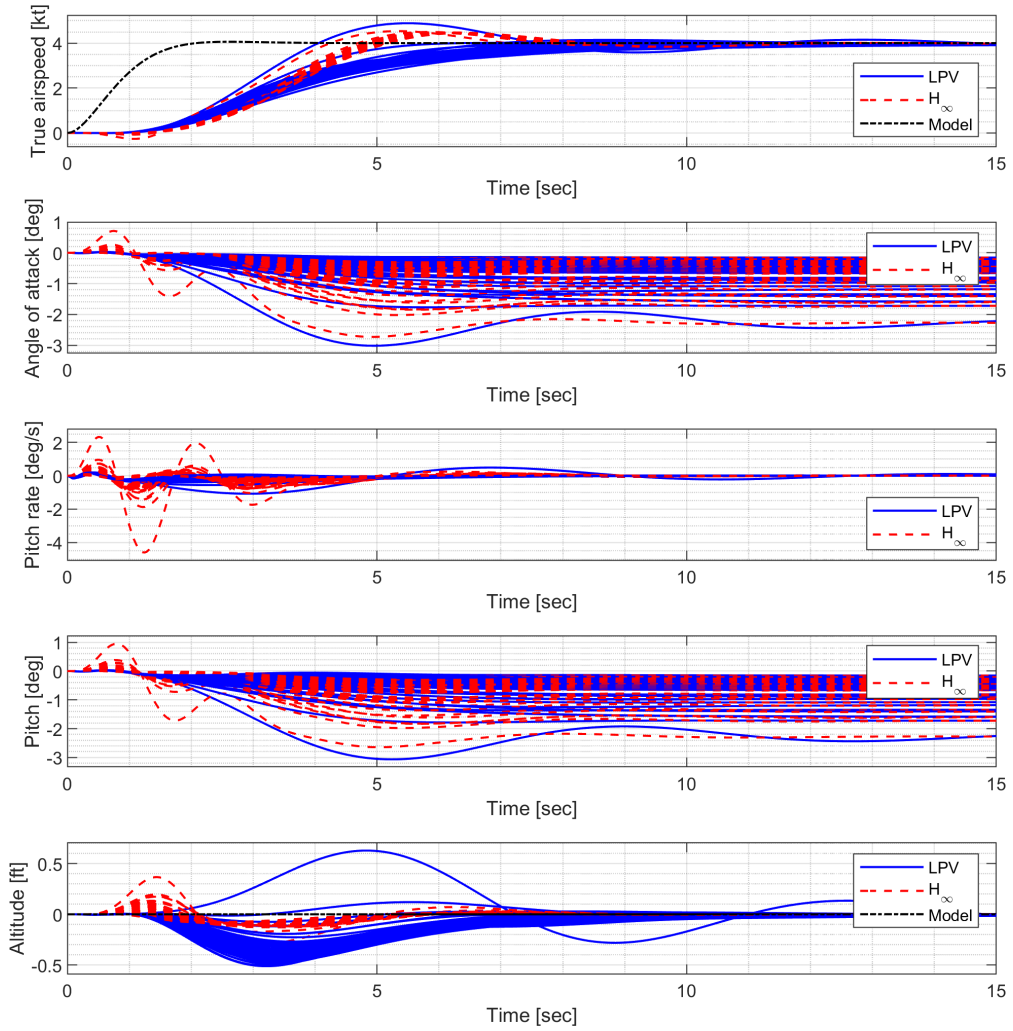


Figure 5.4 State response to the true airspeed step command.

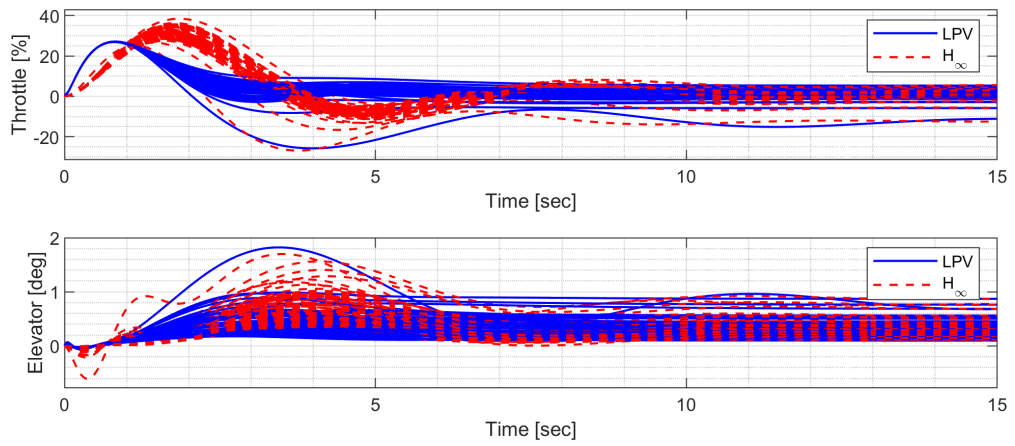


Figure 5.5 Input response to the true airspeed step command.

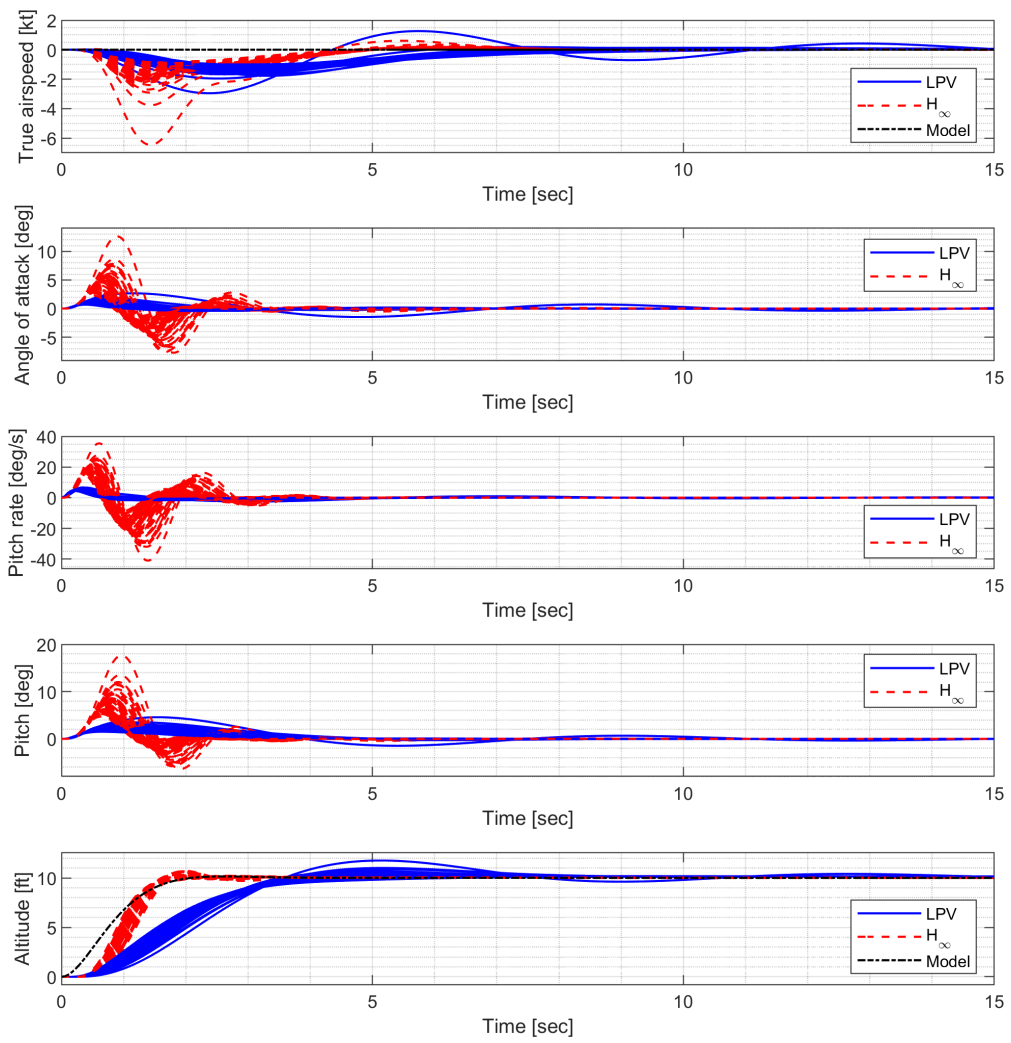


Figure 5.6 State response to the altitude step command.

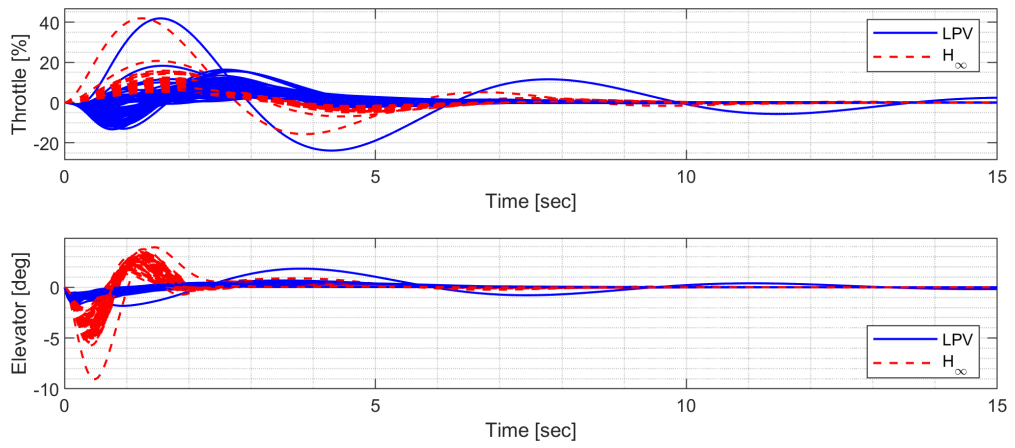


Figure 5.7 Input response to the altitude step command.

5.2 Lateral-Directional Autopilot Design for Turn Coordination and Roll Angle Control

In this section, a roll angle autopilot is designed based on LPV methods for the control of lateral-directional motion. The autopilot serves to keep the wings level. Additional control systems must be used to regulate the sideslip and pitch rate if the aircraft is maintained at an angle other than with the wings level in order to achieve a coordinated turning motion. In turn, the commanded pitch rate will determine whether the airplane gains or loses height. If there is a way to change the roll reference, the aircraft can be directed in any direction using just one control. The inner-loops for various autopilots can be provided by these control systems, enabling an airplane to fly on a constant compass heading or follow a radio navigation beam in spite of crosswinds.

5.2.1 Performance Specifications

There is a significant coupling between the two control inputs (aileron, rudder) and the two main outputs (sideslip angle, roll angle) in the lateral-direction aircraft dynamics. The interconnection shown in Fig. 5.8 is considered for control design.

The aileron, rudder, and morphing actuator are modeled in the same way as in the CAS design. The reference weight is set to 30 deg for the roll angle command, and this condition can be forced in the guidance command. The ideal model for the AOS response to the command is set to have a natural frequency of 2 rad/s and a damping ratio of 0.8 to allow for some overshoot. The ideal model for the roll rate response to the command is set to have a natural frequency of 5 rad/s and a damping ratio of 0.8 to allow for faster

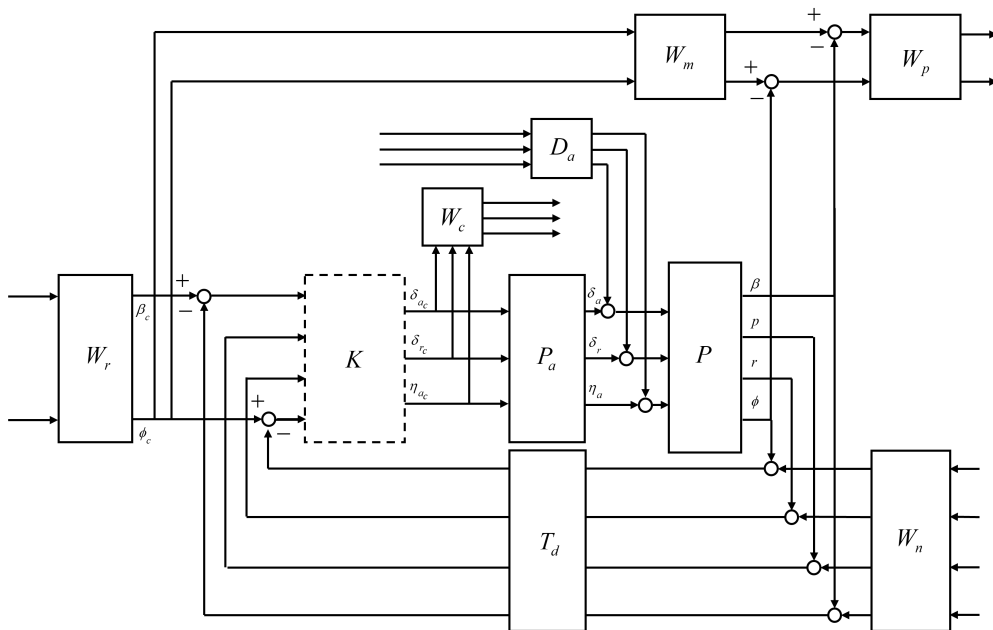


Figure 5.8 Closed-loop interconnection of the lateral-directional autopilot.

convergence. Performance weights are set such that the model matching error does not exceed two times the corresponding measurement noise level at low frequencies. The sensor measurement error is modeled as white Gaussian noise, and the standard deviation is set to match the sensor specifications of the GTM. In the actuator model, disturbance of 0.01 deg is added below 0.5 rad/s to account for errors due to dead zone, saturation, rate limit, and additional uncertainties arising from complex morphing mechanisms.

5.2.2 Controller Synthesis and Analysis

The LPV controller and the \mathcal{H}_∞ controller are synthesized. The open-loop and closed-loop Bode magnitude plots are shown in Figs. 5.9 and 5.10. The trend in magnitude response appears similar to that in CAS. The step responses are shown in Figs. 5.11-5.14. In the case of AOS, it can be seen that both controllers follow the ideal model almost perfectly.

Table 5.2 Weighting filters for the lateral-directional autopilot design.

Weighting Filter	Value
P_{a_a}	$\frac{31.42}{s+31.42}$
P_{a_r}	$\frac{31.42}{s+31.42}$
P_{a_m}	$\frac{3.142}{s+3.142}$
W_{r_β}	$3 \cdot 0.1745$
W_{r_ϕ}	$30 \cdot 0.1745$
W_{m_β}	$\frac{2^2}{s^2+2 \cdot 0.8 \cdot 2s+2^2}$
W_{m_ϕ}	$\frac{5^2}{s^2+2 \cdot 0.8 \cdot 5s+5^2}$
W_{p_β}	$\frac{2 \cdot 0.033 \cdot 0.1745 \cdot (s/120+1)}{s/0.1+1}$
W_{p_ϕ}	$\frac{2 \cdot 0.02 \cdot 0.1745 \cdot (s/120+1)}{s/0.003+1}$
W_{n_β}	$0.033 \cdot 0.1745$
W_{n_p}	$0.5220 \cdot 0.1745$
W_{n_r}	$0.3330 \cdot 0.1745$
W_{n_ϕ}	$0.02 \cdot 0.1745$
W_{c_a}	$\frac{0.0001(s/0.1+1)}{s/120+1}$
W_{c_r}	$\frac{0.0005(s/0.1+1)}{s/120+1}$
W_{c_m}	$\frac{0.01(s/0.1+1)}{s/120+1}$
D_a	$\left(\frac{0.01}{s/0.5+1} \right) I_3$
T_d	$\text{diag}\left(\frac{-s+66.67}{s+66.67}, \frac{-s+66.67}{s+66.67}, \frac{-s+66.67}{s+66.67}, \frac{-s+28.57}{s+28.57} \right)$

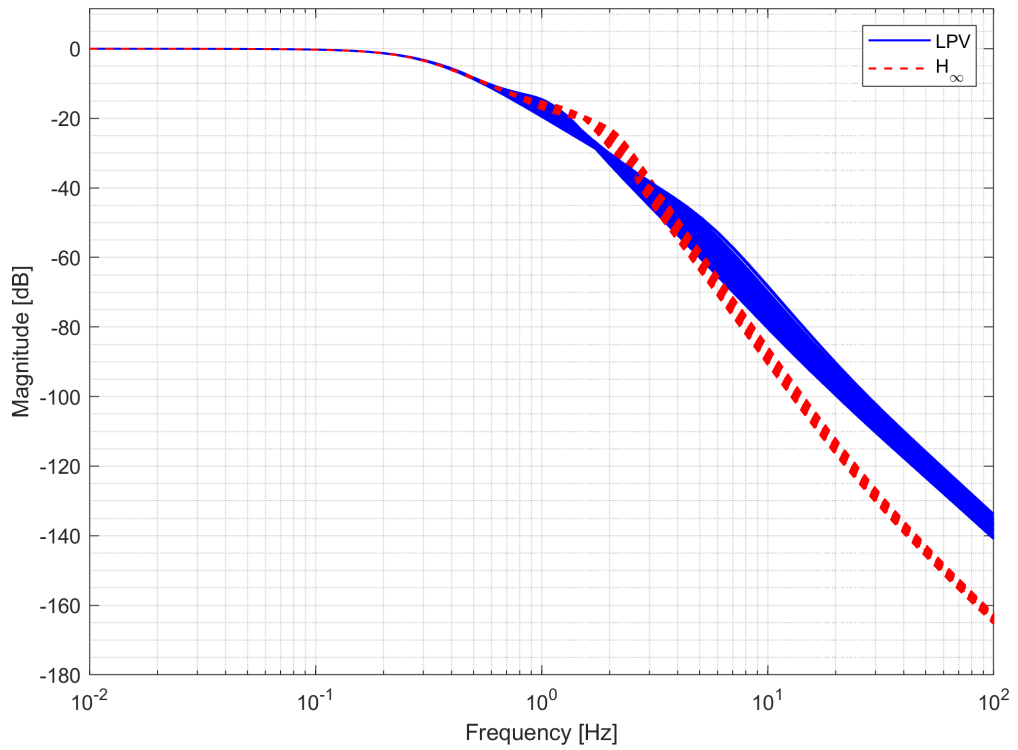


Figure 5.9 Bode magnitude plot for the lateral-directional autopilot - angle of sideslip.

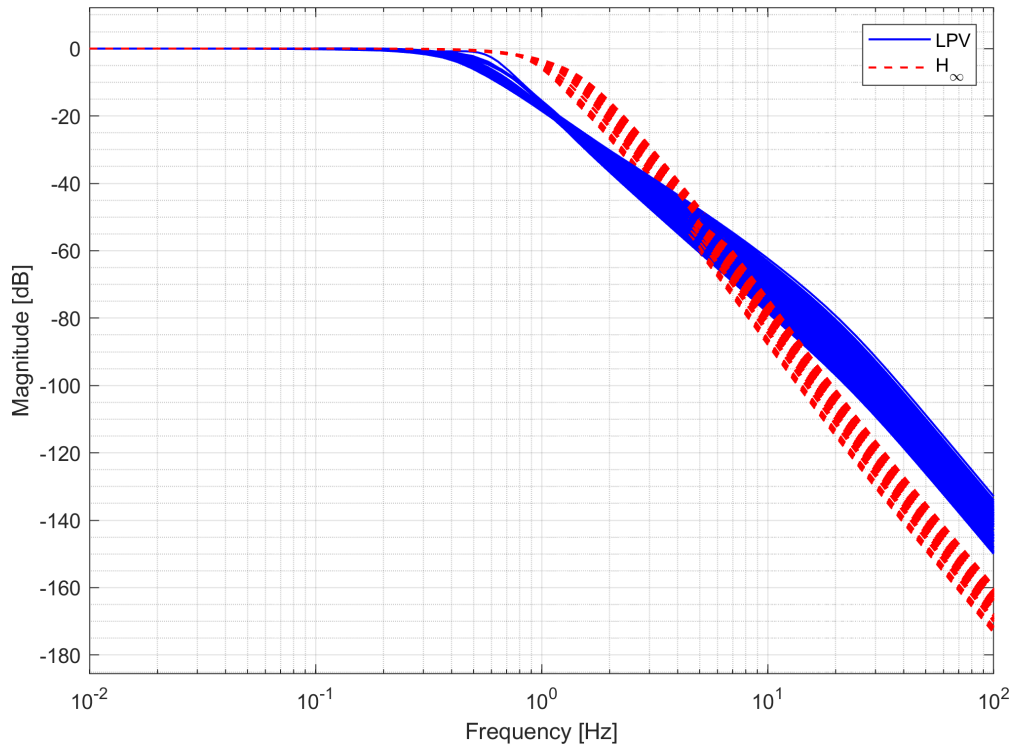


Figure 5.10 Bode magnitude plot for the lateral-directional autopilot - roll angle.

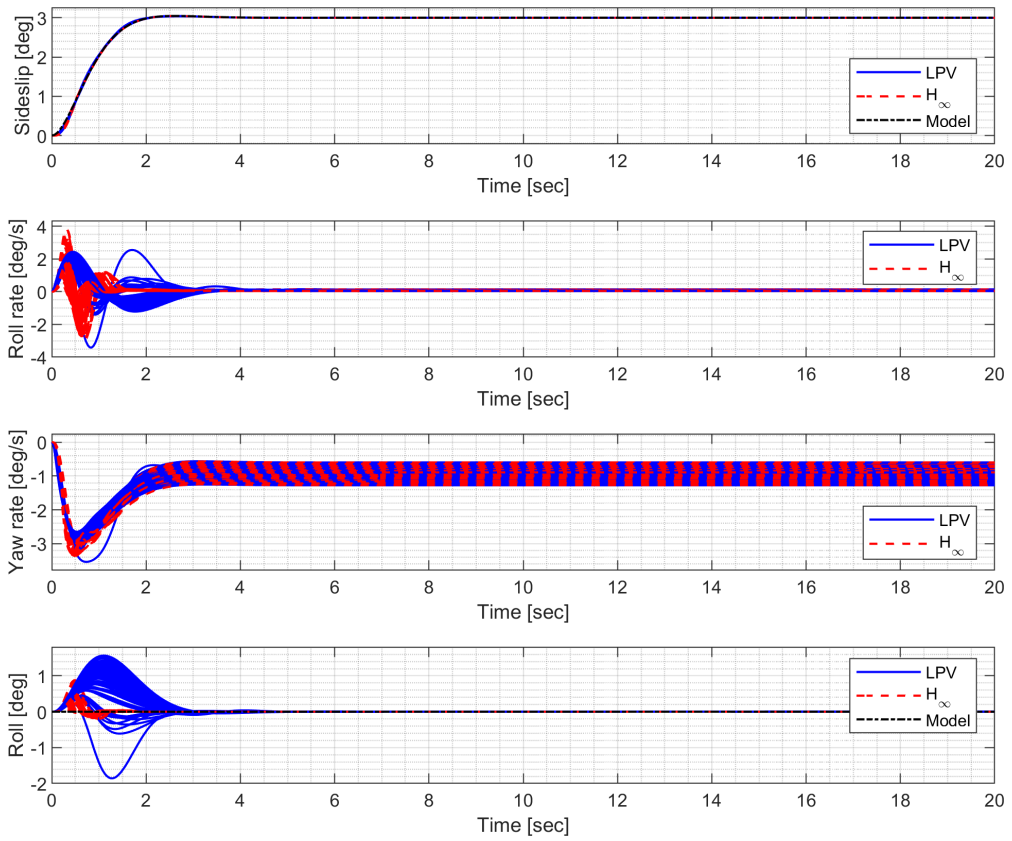


Figure 5.11 State response to the angle of sideslip step command.

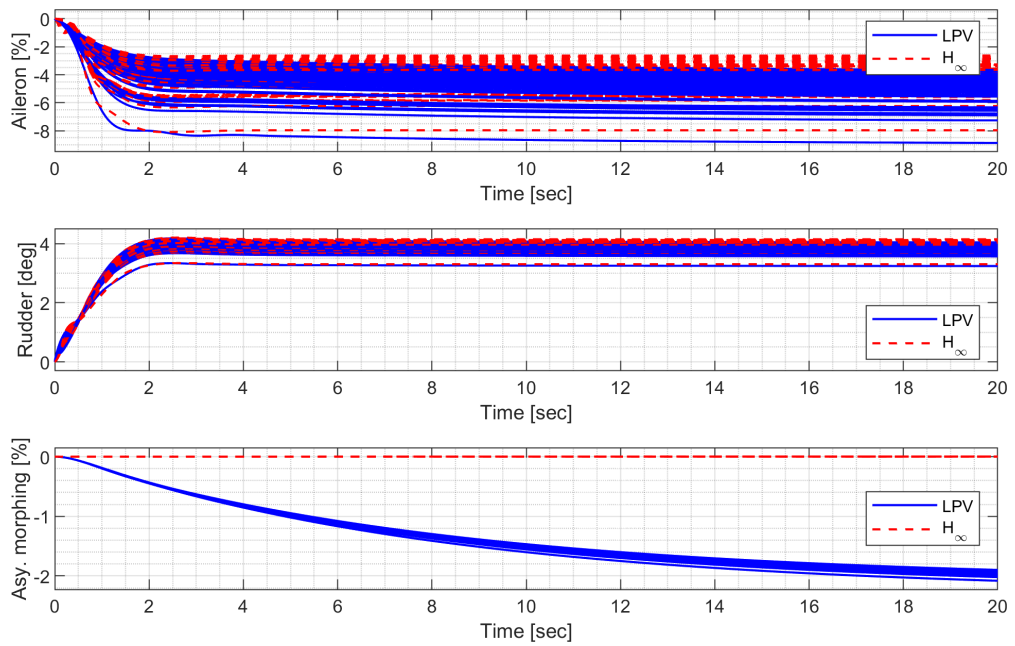


Figure 5.12 Input response to the angle of sideslip step command.

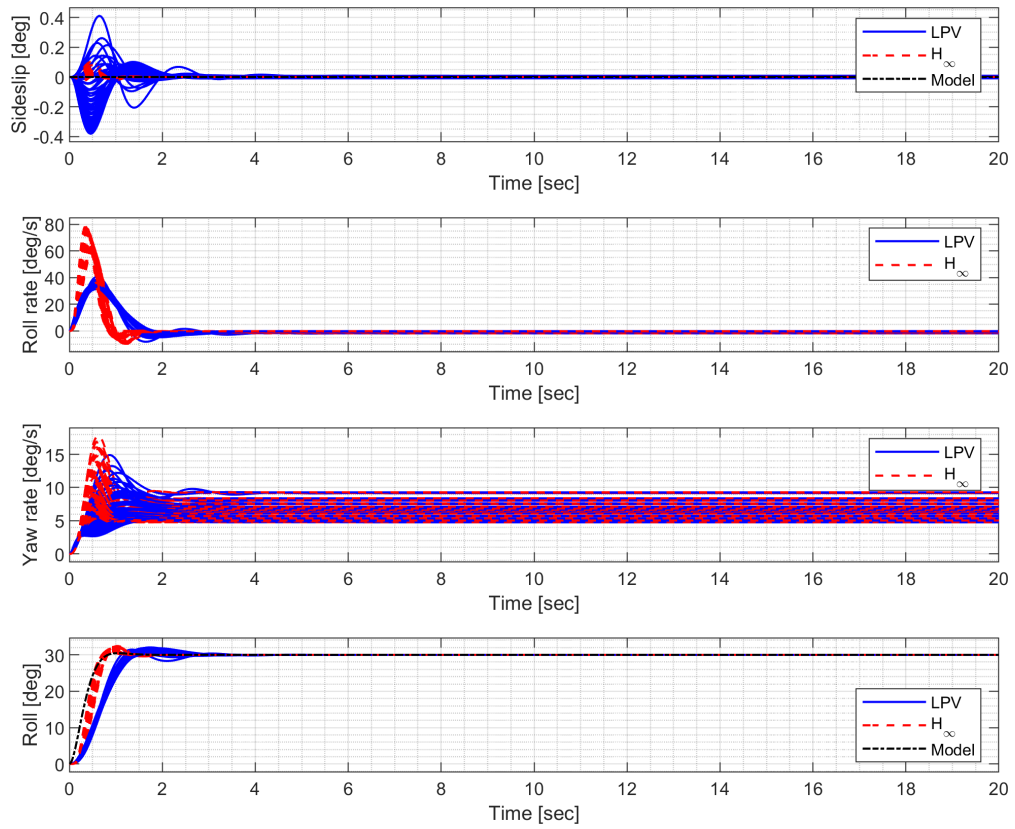


Figure 5.13 State response to the roll angle step command.

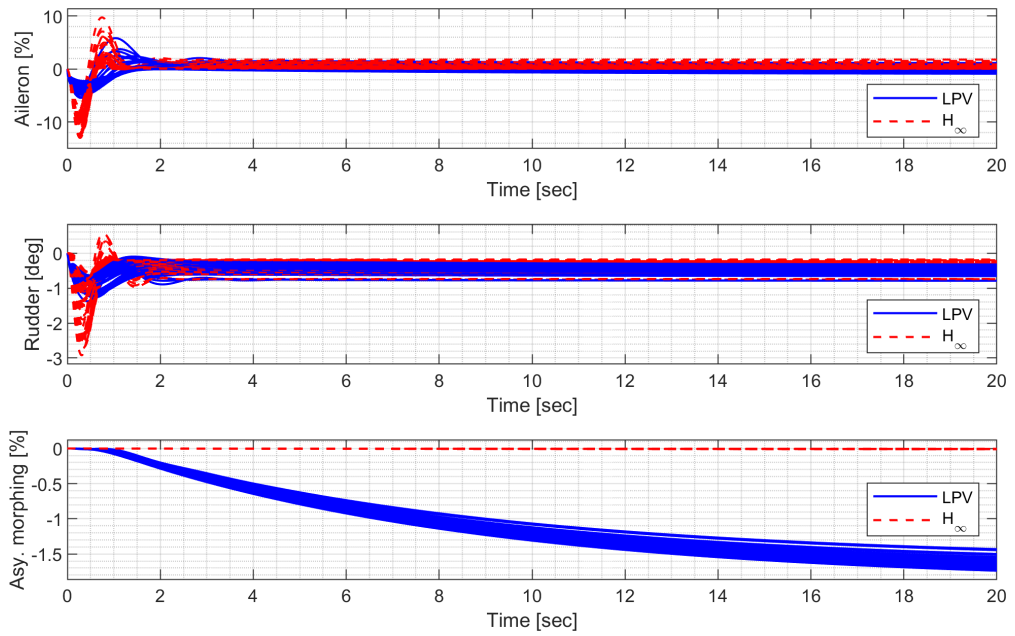


Figure 5.14 Input response to the roll angle step command.

5.3 Nonlinear Guidance Law for Trajectory Tracking

A lookahead distance is used to compute desired course angle. The lateral acceleration command is generated from the guidance law [132].

$$a_{s_{cmd}} = 2 \frac{V^2}{d} \sin \sigma \quad (5.1)$$

To convert the lateral acceleration command into the bank angle command, the relation $a_s \approx g\phi$ derived from aircraft coordinate turn was utilized. A heading controller is used to compute the required roll angle.

$$\phi_c = \tan^{-1} \left(K_\psi \frac{V}{g} (\psi_c - \psi) \right) \quad (5.2)$$

$$\dot{\psi} + K_\psi \psi = K_\psi \psi_c \quad (5.3)$$

$$\frac{\psi(s)}{\psi_c(s)} = \frac{K_\psi}{s + K_\psi} \quad (5.4)$$

Heading controller gain is set to $K_\psi = 3.9$.

The optimal span morphing parameter can be determined as a function of flight conditions (airspeed and altitude). Furthermore, the span morphing parameter can be increased to attenuate altitude drop when large roll angle command is engaged. In this study, the span morphing parameter deviation from the setpoint is obtained in proportion to the roll angle command.

5.4 Nonlinear Simulation of Morphing-Assisted Flights

In this section, numerical simulation for trajectory tracking flight is performed to demonstrate the effectiveness of the proposed scheme.

5.4.1 Waypoint Following at Low Altitude

The morphing UAV is commanded to follow four waypoints placed 3,000 ft apart at the same altitude. The resulting trajectory and state response are shown in Figs. 5.15-5.17. It is noted that the \mathcal{H}_∞ controller exhibits larger oscillation in both the longitudinal and the lateral-directional motions, possibly due to rapid parameter variations.

5.4.2 Circular Trajectory Tracking at High Altitude

The morphing UAV is commanded to follow a horizontal orbit with a radius of 2000 ft. The resulting trajectory and state response are shown in Figs. 5.18-5.20. It is noted that the \mathcal{H}_∞ controller exhibits undesirable chattering phenomena in both the longitudinal and the lateral-directional motions as a result of aggressive high gains.

5.4.3 Helical Ascent under Fast Morphing

The morphing UAV is commanded to follow a helical path with a radius of 2,000 ft and a rate of climb of 30 ft/s, which corresponds to approximately a flight path angle of 9.18 deg. The resulting trajectory and state response are shown in Figs. 5.21-5.23. The extremely fast morphing is engaged to test the marginal performance of the designed controllers. Note that the oscillation of the \mathcal{H}_∞ controller gradually grows and eventually diverges while the LPV

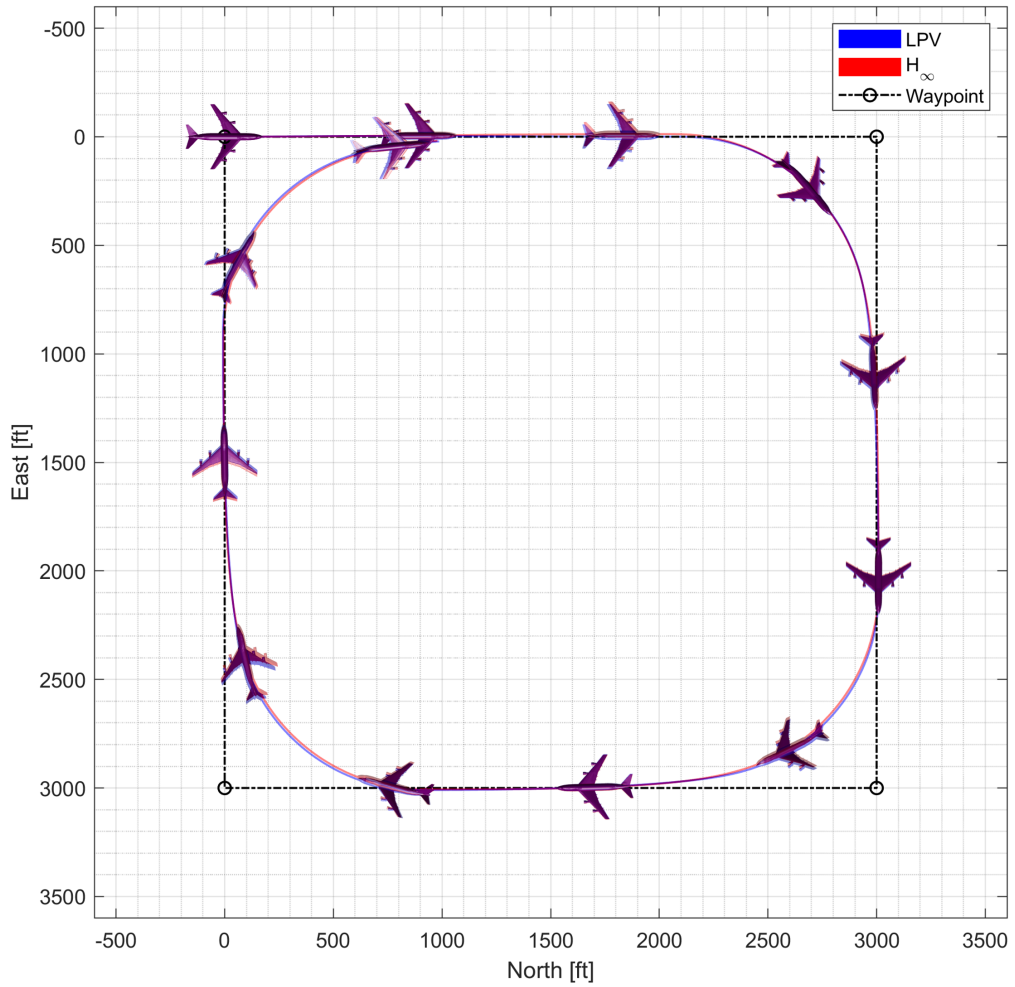


Figure 5.15 Flight trajectory of the waypoint-following flight.

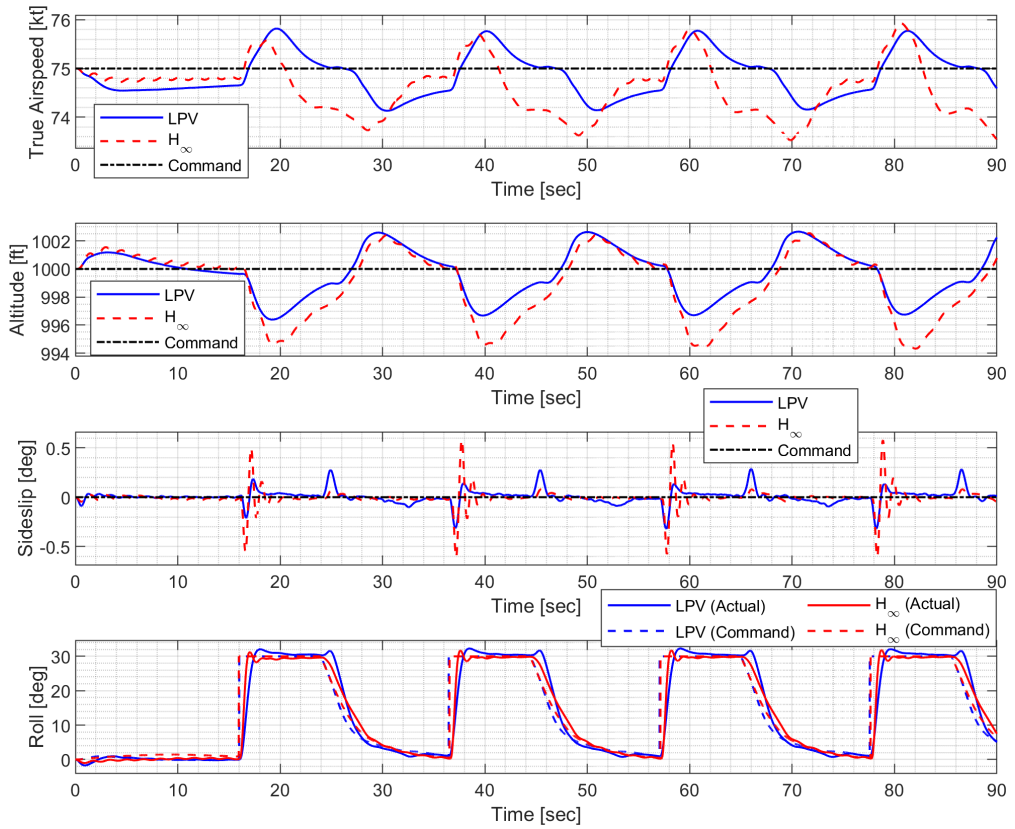


Figure 5.16 State history of the waypoint-following flight.

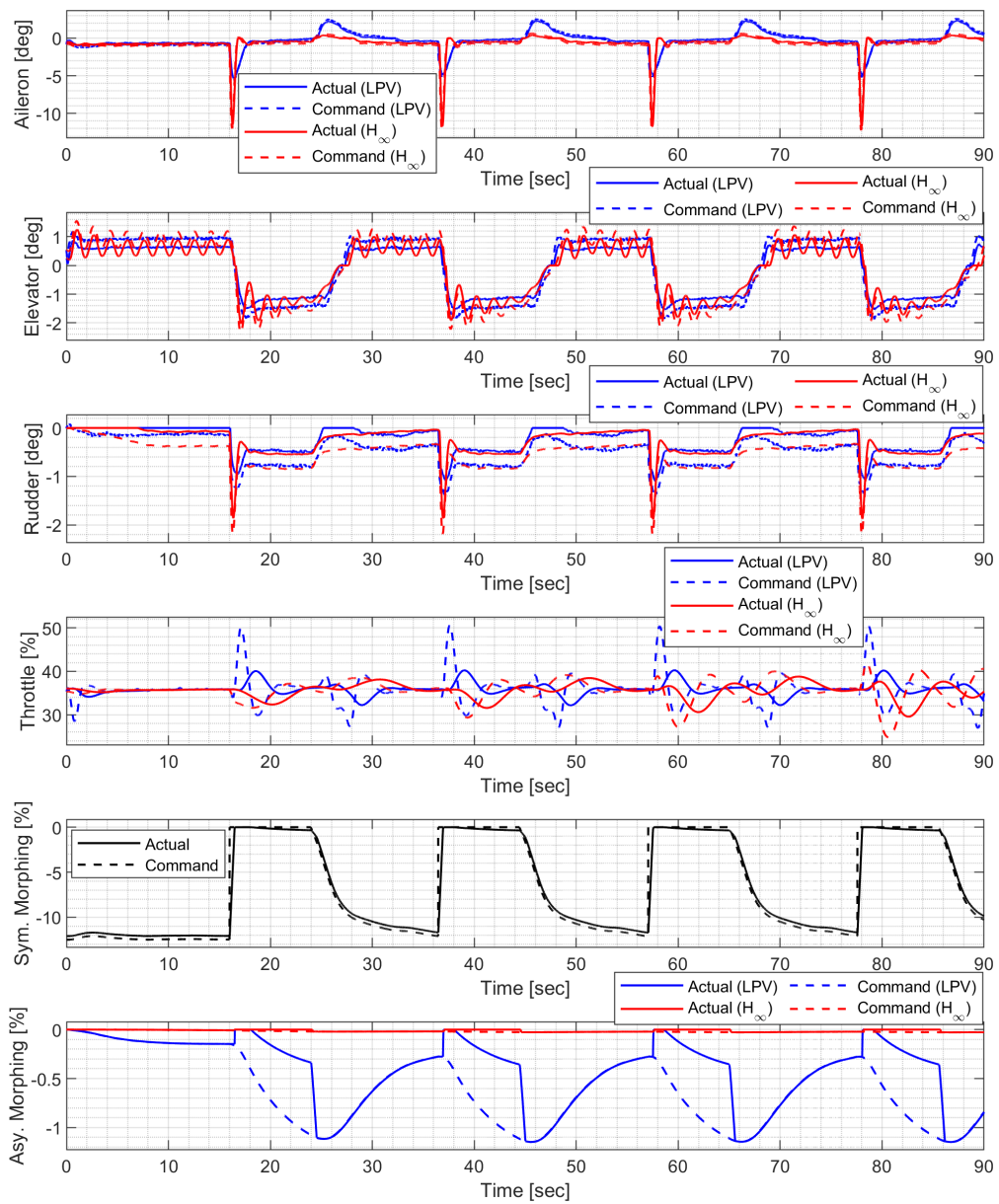


Figure 5.17 Input history of the waypoint-following flight.

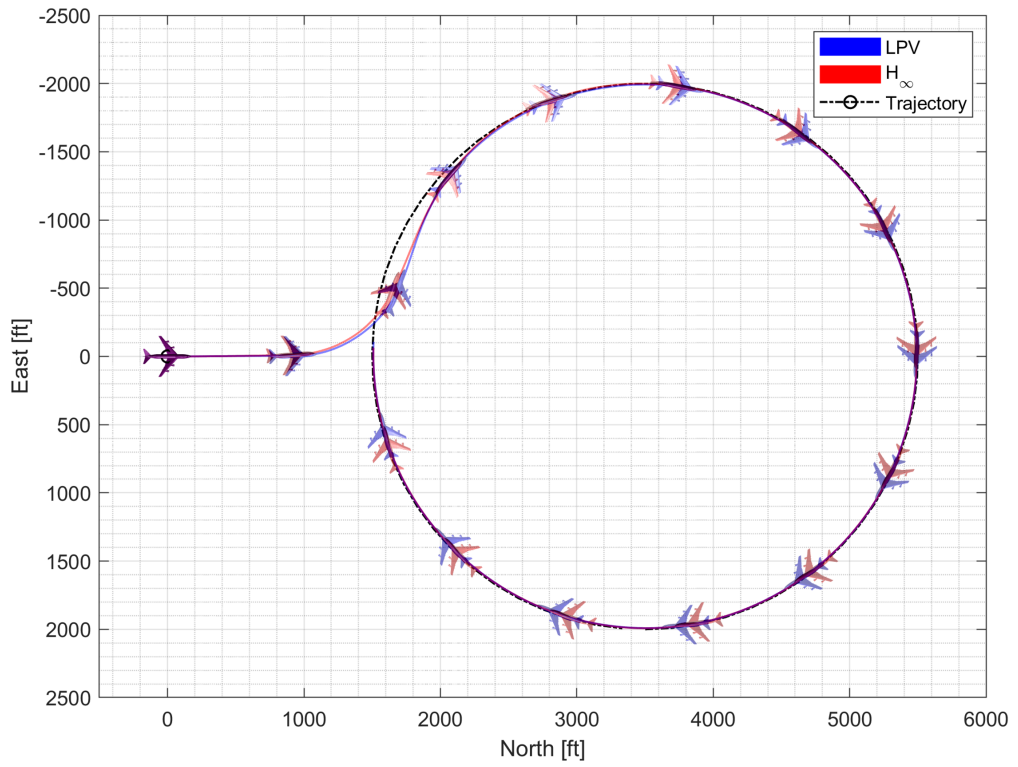


Figure 5.18 Flight trajectory of the circular trajectory-following flight.

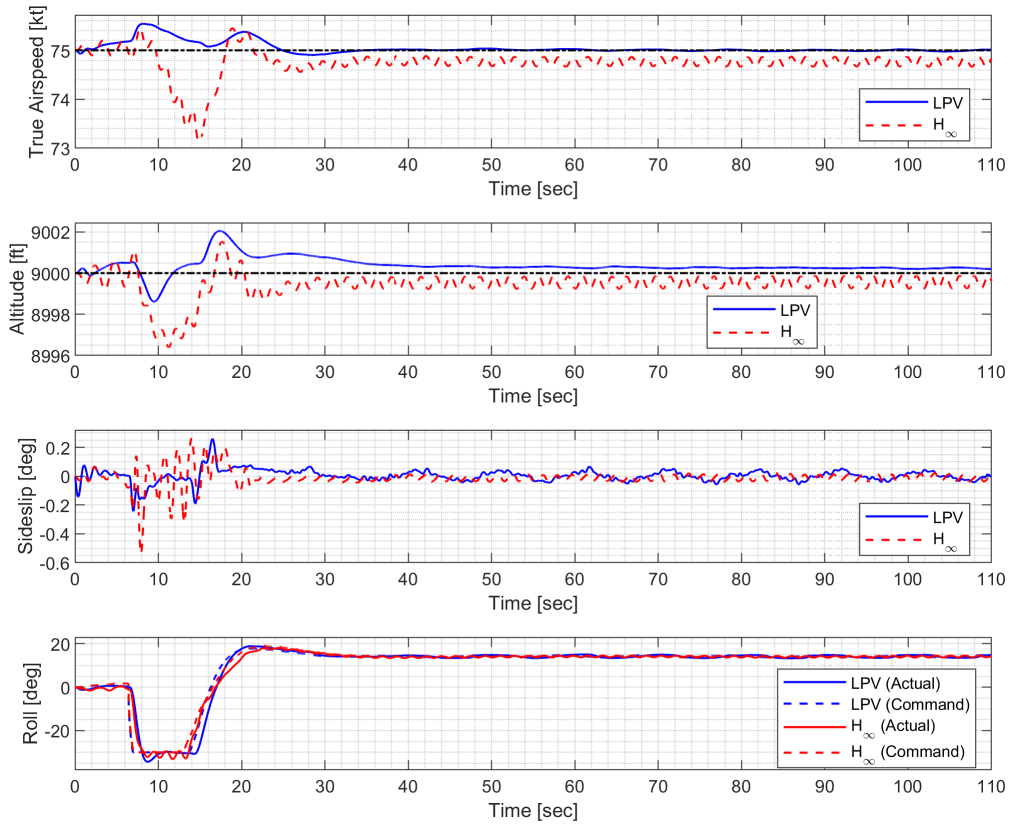


Figure 5.19 State history of the circular trajectory-following flight.

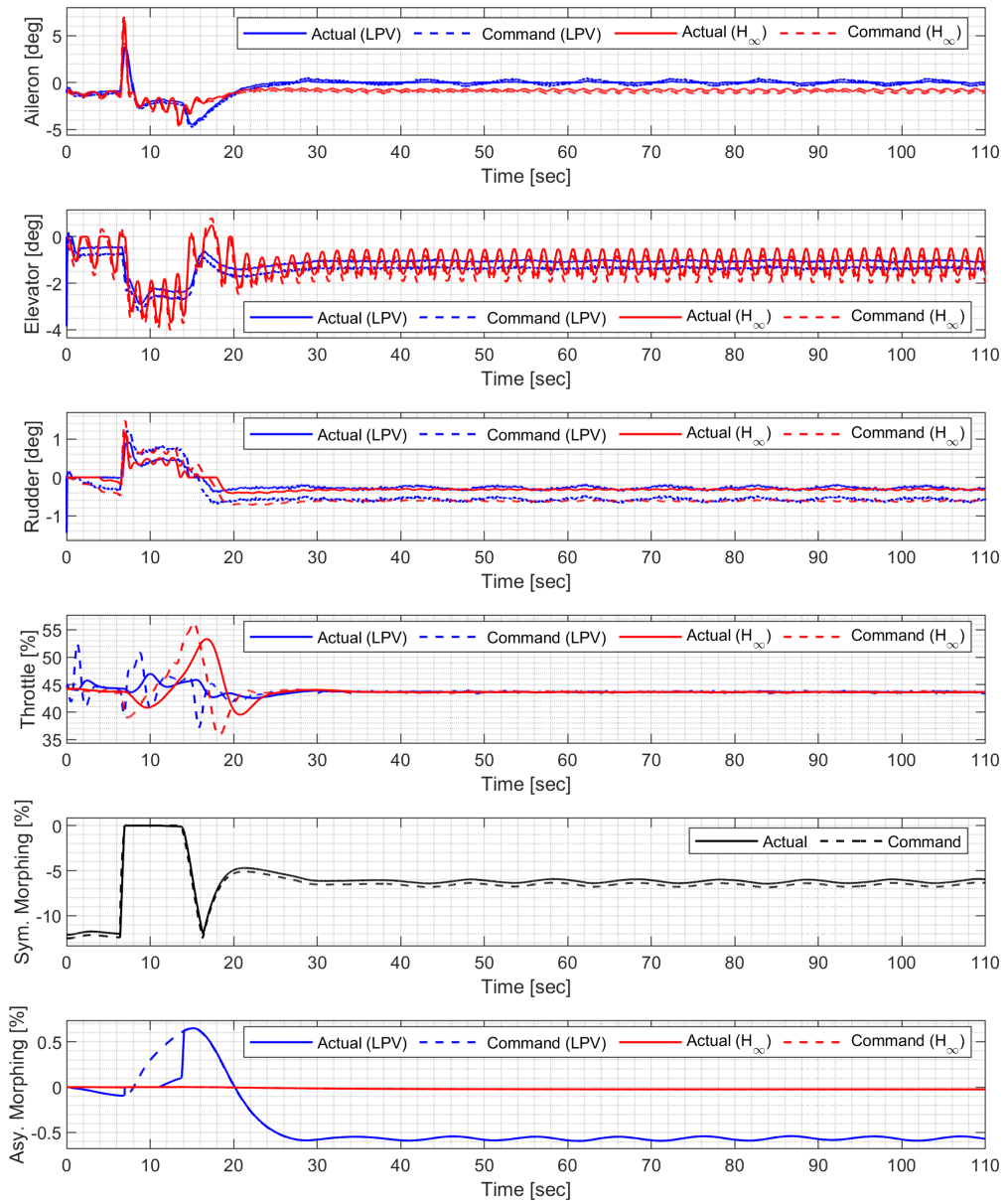


Figure 5.20 Input history of the circular trajectory-following flight.

controller maintains the tracking performance. [p]

5.4.4 Spiral Descent with Morphing Scheduling

The morphing UAV is commanded to follow a helical path with a radius of 2,000 ft and a rate of descent of -20 ft/s, which corresponds to approximately a flight path angle of -8.98 deg. The symmetric morphing configuration is scheduled on the flight conditions so that the aerodynamic performance is improved. The resulting trajectory and state response are shown in Figs. 5.24-5.26. Note that the oscillation of the \mathcal{H}_∞ controller quickly loses stability even when the scheduling parameter undergoes gentle changes while the LPV controller maintains the tracking performance.

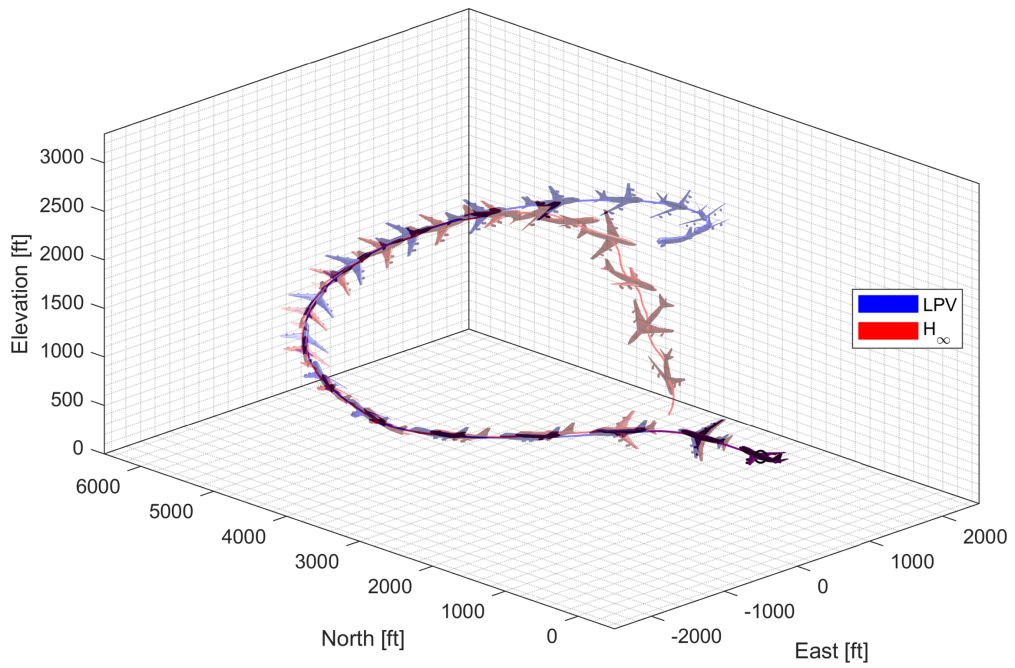


Figure 5.21 Flight trajectory of the helical ascent.

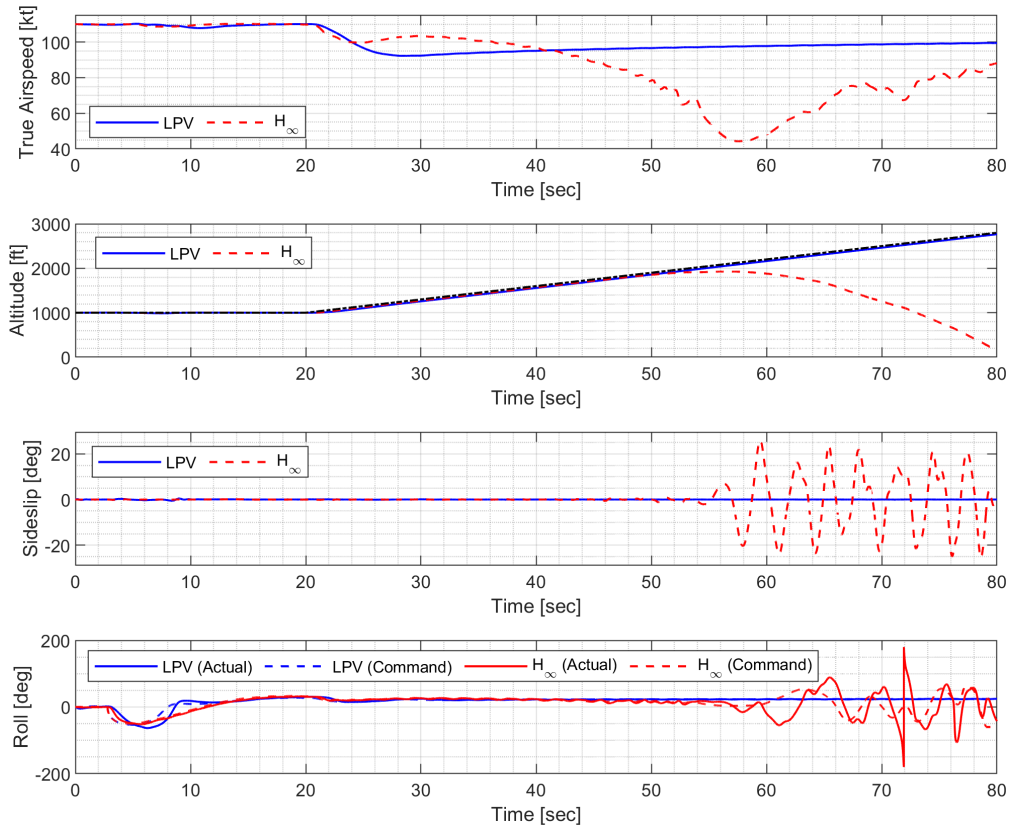


Figure 5.22 State history of the helical ascent.

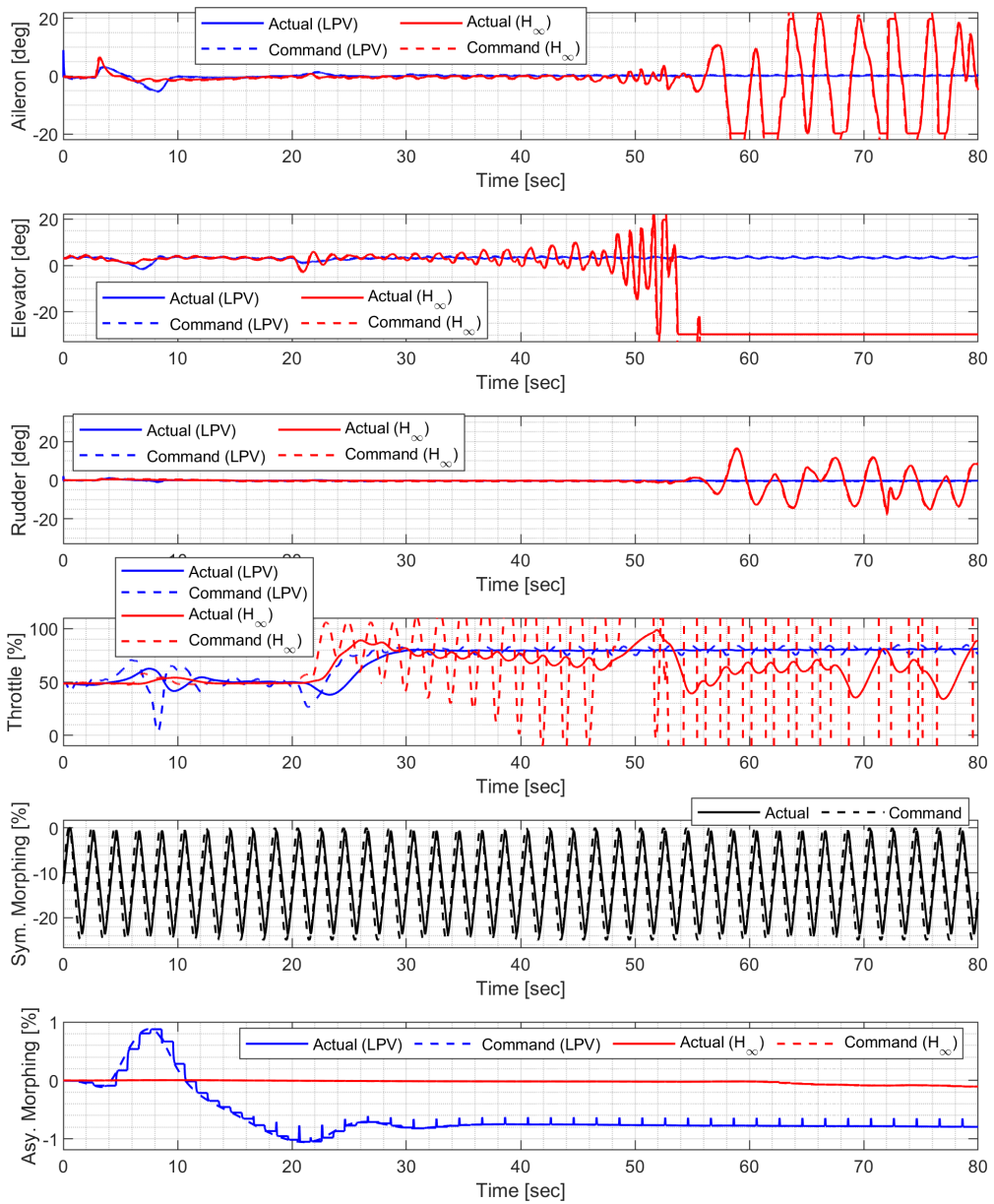


Figure 5.23 Input history of the helical ascent.

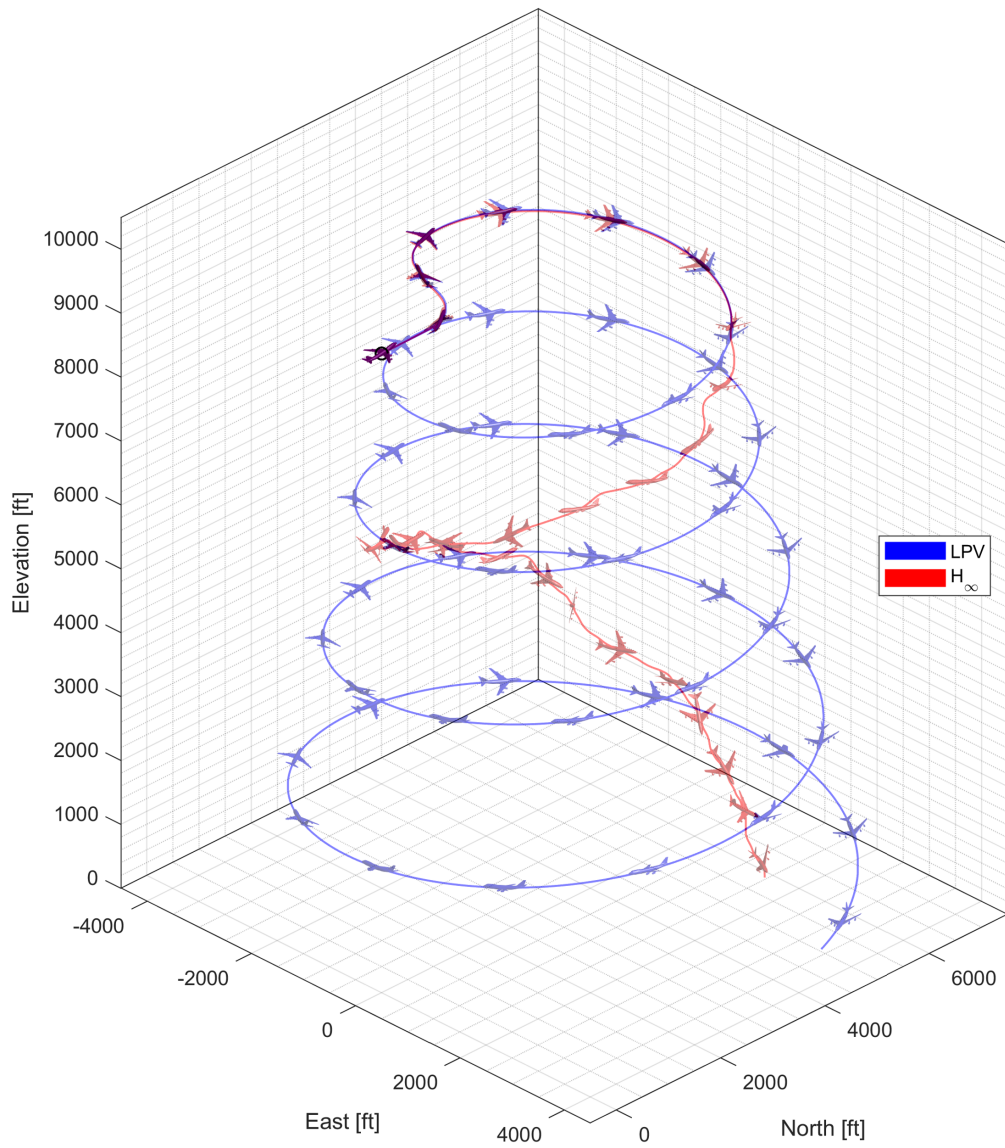


Figure 5.24 Flight trajectory of the helical descent.

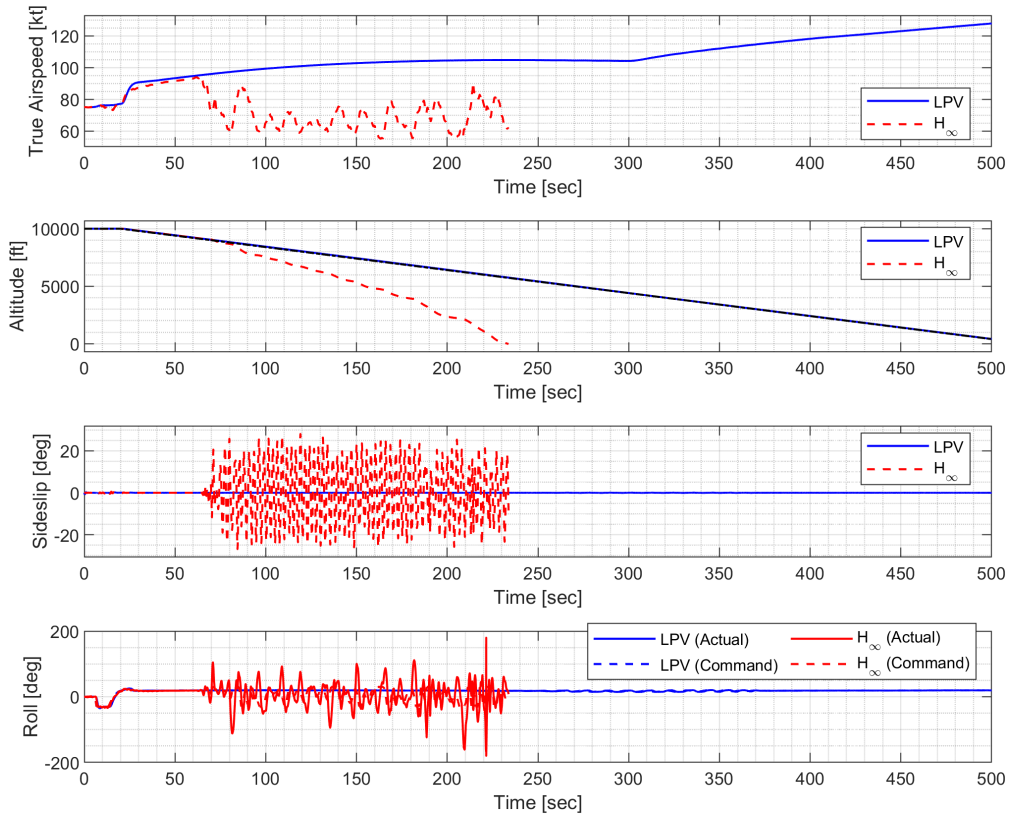


Figure 5.25 State history of the helical descent.

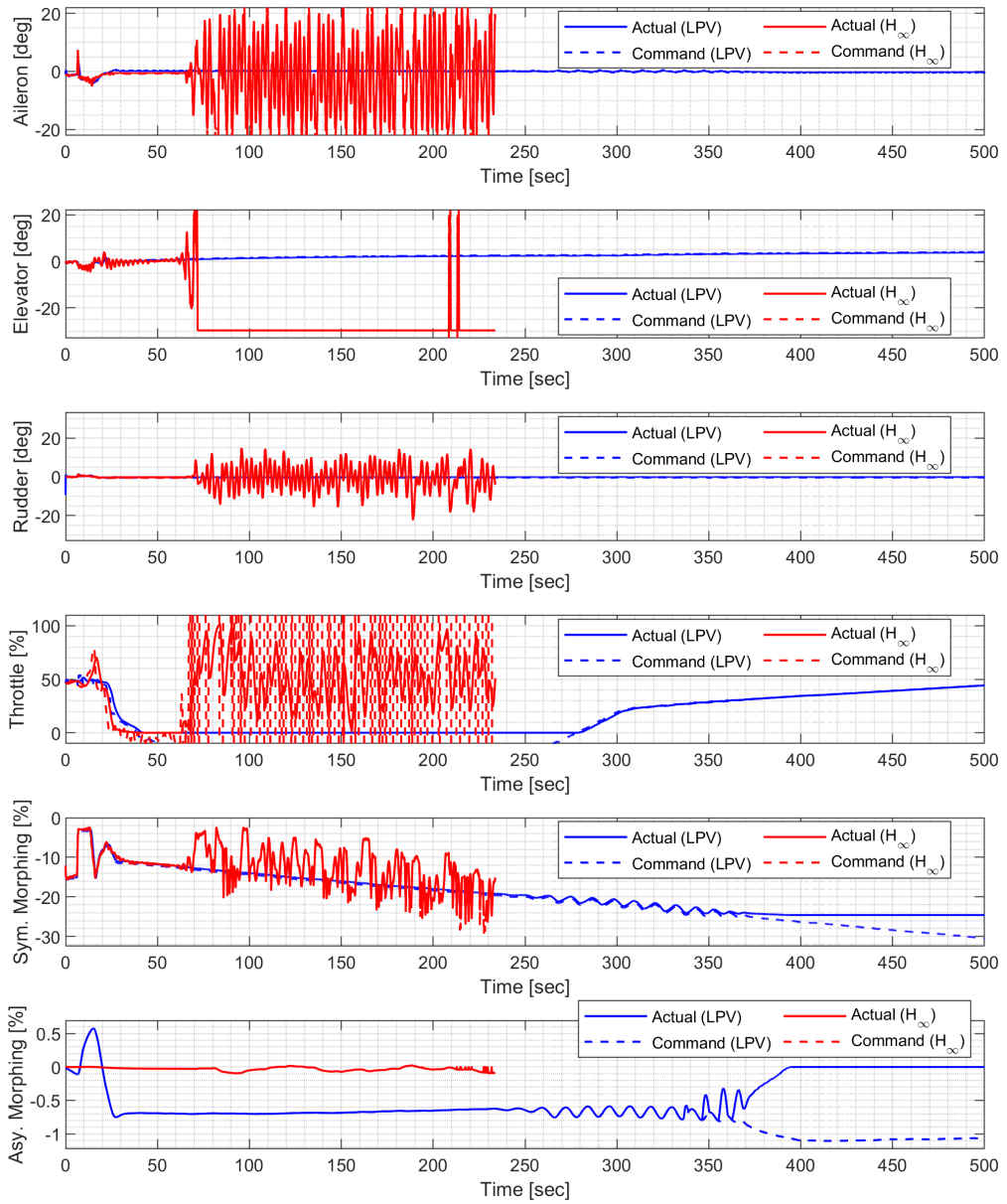


Figure 5.26 Input history of the helical descent.

Chapter 6

Conclusion

6.1 Concluding Remarks

A novel framework is proposed for flight control of morphing unmanned aerial vehicles (UAVs). The proposed scheme takes the benefits of symmetric span morphing in the longitudinal performance while utilizing asymmetric span morphing as a means for roll control. The control system was designed based on linear parameter-varying (LPV) methods which naturally suit the parameter-varying nature of morphing UAVs.

First, a high-fidelity model of asymmetric variable-span morphing UAV was derived from the NASA generic transport model (GTM). The impacts of morphing on the center of mass, inertia matrix, and aerodynamics were appropriately modeled. Symmetric span morphing was included in the scheduling parameters. Longitudinal and lateral-directional LPV models were constructed by associating point-wise linear time-invariant models obtained through Jacobian linearization.

Second, the control augmentation system was designed based on LPV methods to track normal acceleration and roll rate command while maintaining a small angle of the sideslip. The relatively low bandwidth of the morphing actu-

ator was adequately considered in the control design procedure. Strategies for determining symmetric span morphing configuration to assist maneuver were proposed. A high-fidelity GTM simulator was used to demonstrate that the proposed scheme is successfully applied to agile maneuvers such as push-over and pull-up maneuvers and high-g turn.

Finally, the autopilot was designed based on LPV methods to track air-speed, altitude, and roll angle command while maintaining a small angle of sideslip. Nonlinear guidance law was coupled with the autopilot to enable three-dimensional trajectory tracking. It was demonstrated that symmetric morphing configuration could be arbitrarily changed without affecting stability to either assist maneuver or optimize aerodynamic characteristics for a given flight condition.

6.2 Future Work

In the future, a technique for determining the optimal shape in real time can be studied. Determination of the optimal shape considering only flight conditions can also be done offline. Therefore, the online optimum shape determiner should be able to appropriately consider not only the current flight conditions but also guidance commands given from the outside. For example, even under the same flight conditions, a longer span can be extended when a large amount of lift is required. However, a short span can be advantageous when a high-speed dash or rapid rotation of a roll axis is required. When only one morphing parameter is considered as a scheduling parameter, the problem can be easily solved with a simple line search as long as the problem is well-defined. However, if there are two or more morphing parameters, the problem may become more

difficult to solve.

Bibliography

- [1] Reich, G., and Sanders, B., “Introduction to Morphing Aircraft Research,” *Journal of Aircraft*, Vol. 44, No. 4, 2007, p. 1059.
DOI:10.2514/1.28287

- [2] Valasek, J., *Morphing Aerospace Vehicles and Structures*, John Wiley & Sons, Chichester, UK, 2012.

- [3] Wickenheiser, A. M., and Garcia, E., “Aerodynamic Modeling of Morphing Wings Using an Extended Lifting-Line Analysis,” *Journal of Aircraft*, Vol. 44, No. 1, 2007, pp. 10–16.
DOI:10.2514/1.18323

- [4] Cunningham, K., Cox, D. E., Murri, D. G., and Riddick, S. E., “A Piloted Evaluation of Damage Accommodating Flight Control Using a Remotely Piloted Vehicle,” *AIAA Guidance, Navigation, and Control Conference*, Portland, OR, Aug. 2011.
DOI:10.2514/6.2011-6451

- [5] Dimino, I., Lecce, L., and Pecora, R., *Morphing Wing Technologies: Large Commercial Aircraft and Civil Helicopters*, Elsevier, Amsterdam, Netherlands, 2018.

- [6] Bye, D. R., and McClure, P. D., “Design of a Morphing Vehicle,” *48th AIAA/ASME/ASCE/AHS/ASC Structures, Structural Dynamics and Materials Conference*, Honolulu, HI, Apr. 2007.
DOI:10.2514/6.2007-1728
- [7] Friswell, M. I., and Wereley, N. M., “Special Topical Issue on Morphing Aircraft,” *Journal of Intelligent Material Systems and Structures*, Vol. 22, No. 9, 2011, pp. 821–822.
DOI:10.1177/1045389X11419004
- [8] Mulyanto, T., Luthfi, M., Nurhakim, I., and Sasongko, R. A., “Development of a Morphing Flying Platform for Adaptive Control System Study,” *27th Congress of the International Council of the Aeronautical Sciences*, Nice, France, Sep. 2010.
- [9] Sirohi, J., “High-Speed Hover-Capable Morphing Micro Air Vehicle,” *Journal of Aircraft*, Vol. 50, No. 6, 2013, pp. 1765–1775.
DOI:10.2514/1.C032144
- [10] Frommer, J. B., and Crossley, W. A., “Enabling Continuous Optimization for Sizing Morphing Aircraft Concepts,” *43rd AIAA Aerospace Sciences Meeting and Exhibit*, Reno, NV, Jan. 2005.
DOI:10.2514/6.2005-816
- [11] Snow, S. A., *Airframe and Systems Design, Analysis, and Testing of the Horizon Morphing-Wing Aircraft*, MS Thesis, Department of Mechanical and Aerospace Engineering, Utah State University, Logan, UT, 2021.

- [12] Peters, C., Roth, B., Crossley, W. A., and Weisshaar, T. A., “Use of Design Methods to Generate and Develop Missions for Morphing Aircraft,” *9th AIAA/ISSMO Symposium on Multidisciplinary Analysis and Optimization*, Atlanta, GA, Sep. 2002.
DOI:10.2514/6.2002-5468
- [13] Barbarino, S., Bilgen, O., Ajaj, R. M., Friswell, M. I., and Inman, D. J., “A Review of Morphing Aircraft,” *Journal of Intelligent Material Systems and Structures*, Vol. 22, No. 9, 2011, pp. 823–877.
DOI:10.1177/1045389X11414084
- [14] Joshi, S. P., Tidwell, Z., Crossley, W. A., and Ramakrishnan, S., “Comparison of Morphing Wing Strategies Based Upon Aircraft Performance Impacts,” *Collection of Technical Papers - AIAA/ASME/ASCE/AHS/ASC Structures, Structural Dynamics and Materials Conference*, Palm Springs, CA, Apr. 2004.
DOI:10.2514/6.2004-1722
- [15] Bil, C., Massey, K., and Abdullah, E. J., “Wing Morphing Control with Shape Memory Alloy Actuators,” *Journal of Intelligent Material Systems and Structures*, Vol. 24, No. 7, 2013, pp. 879–898.
DOI:10.1177/1045389X12471866
- [16] Abdullah, E. J., Bil, C., and Watkins, S., “Performance of Adaptive Airfoil Control System Using Shape Memory Alloy Actuators For UAV,” *11th AIAA Aviation Technology, Integration, and Operations (ATIO) Conference*, Virginia Beach, VA, Sep. 2011.
DOI:10.2514/6.2011-6849

- [17] Bashir, M., Lee, C. F., and Rajendran, P., “Shape Memory Materials and Their Applications in Aircraft Morphing: An Introspective Study,” *ARPJ Journal of Engineering and Applied Sciences*, Vol. 12, No. 19, 2017, pp. 5434–5446.
- [18] Barbarino, S., Flores, E. L. S., Ajaj, R. M., Dayyani, I., and Friswell, M. I., “A Review on Shape Memory Alloys with Applications to Morphing Aircraft,” *Smart Materials and Structures*, Vol. 23, No. 6, Article 063001, 2014.
DOI:10.1088/0964-1726/23/6/063001
- [19] Heeb, R. M., “Design Principles for Geometrically Anisotropic Thermo-plastic Rubber Morphing Aircraft Skins,” *Journal of Intelligent Material Systems and Structures*, Vol. 34, No. 1, 2022, pp. 29–46.
DOI:10.1177/1045389X221096155
- [20] Kölbl, M., and Ermanni, P., “Structural Design and Analysis of an Anisotropic, Bi-axially Morphing Skin Concept,” *Aerospace Science and Technology*, Vol. 120, Article 107292, 2022.
DOI:10.1016/j.ast.2021.107292
- [21] Zheng, J., Chen, X., Sun, Y., Luo, Y., Xiao, L., and Li, R., “Study of a Lightweight Self-Adaptation Multi-Morphing Skin Inspired by Mechanics of Epidermis Cell Walls Producing the Leaf’s Unique Smooth Shape,” *Extreme Mechanics Letters*, Vol. 50, Article 101574, 2021.
DOI:10.1016/j.eml.2021.101574

- [22] Mattioni, F., *Thermally Induced Multi-Stable Composites for Morphing Aircraft Applications*, Ph.D. Dissertation, Department of Aerospace Engineering, Bristol University, Bristol, UK, 2009.
- [23] Jee, S.-C., *Development of Morphing Aircraft Structures using SMP*, MS Thesis, Department of Systems Engineering and Management, Air Force Institute of Technology, Wright-Patterson Air Force Base, OH, 2010.
- [24] Reich, G. W., Sanders, B., and Joo, J. J., “Development of Skins for Morphing Aircraft Applications via Topology Optimization,” *48th AIAA/ASME/ASCE/AHS/ASC Structures, Structural Dynamics and Materials Conference*, Honolulu, HI, Apr. 2007.
DOI:10.2514/6.2007-1738
- [25] Joo, J. J., Reich, G. W., and Westfall, J. T., “Flexible Skin Development for Morphing Aircraft Applications via Topology Optimization,” *Journal of Intelligent Material Systems and Structures*, Vol. 20, No. 16, 2009, pp. 1969–1985.
DOI:10.1177/1045389X09343026
- [26] Woods, B. K., and Friswell, M. I., “The Adaptive Aspect Ratio Morphing Wing: Design Concept and Low Fidelity Skin Optimization,” *Aerospace Science and Technology*, Vol. 42, 2015, pp. 209–217.
DOI:10.1016/j.ast.2015.01.012
- [27] Bubert, E. A., Woods, B. K., Lee, K., Kothera, C. S., and Wereley, N. M., “Design and Fabrication of a Passive 1D Morphing Aircraft Skin,” *Journal of Intelligent Material Systems and Structures*, Vol. 21, No. 17, 2010,

pp. 1699–1717.

DOI:10.1177/1045389X10378777

- [28] Guo, X., Zhao, Q., and Xi, F., “Design Segmented Stiff Skin for a Morphing Wing,” *Journal of Aircraft*, Vol. 53, No. 4, 2016, pp. 962–970.

DOI:10.2514/1.C033252

- [29] Olympio, K. R., and Gandhi, F., “Flexible Skins for Morphing Aircraft Using Cellular Honeycomb Cores,” *Journal of Intelligent Material Systems and Structures*, Vol. 21, No. 17, 2010, pp. 1719–1735.

DOI:10.1177/1045389X09350331

- [30] Seigler, T. M., and Neal, D. A., “Analysis of Transition Stability for Morphing Aircraft,” *Journal of Guidance, Control, and Dynamics*, Vol. 32, No. 6, 2009, pp. 1947–1953.

DOI:10.2514/1.44108

- [31] Grant, D. T., and Lind, R., “Effects of Time-Varying Inertias on Flight Dynamics of an Asymmetric Variable-Sweep Morphing Aircraft,” *AIAA Atmospheric Flight Mechanics Conference and Exhibit*, Hilton Head, SC, Aug. 2007.

DOI:10.2514/6.2007-6487

- [32] Yue, T., Wang, L., and Ai, J., “Multibody Dynamic Modeling and Simulation of a Tailless Folding Wing Morphing Aircraft,” *AIAA Atmospheric Flight Mechanics Conference*, Chicago, IL, Aug. 2009.

DOI:10.2514/6.2009-6155

- [33] Grant, D. T., Chakravarthy, A., and Lind, R., “Modal Interpretation of Time-Varying Eigenvectors of Morphing Aircraft,” *AIAA Atmospheric Flight Mechanics Conference*, Chicago, IL, Aug. 2009.
DOI:10.2514/6.2009-5848
- [34] Shi, R., and Wan, W., “Analysis of Flight Dynamics for Large-Scale Morphing Aircraft,” *Aircraft Engineering and Aerospace Technology*, Vol. 87, No. 1, 2015, pp. 38–44.
DOI:10.1108/AEAT-01-2013-0004
- [35] Obradovic, B., and Subbarao, K., “Modeling of Flight Dynamics of Morphing-Wing Aircraft,” *Journal of Aircraft*, Vol. 48, No. 2, 2011, pp. 391–402.
DOI:10.2514/1.C000269
- [36] Beaverstock, C. S., Fincham, J. H., Friswell, M. I., Ajaj, R., de Breuker, R., and Werter, N., “Effect of Symmetric and Asymmetric Span Morphing on Flight Dynamics,” *AIAA Atmospheric Flight Mechanics Conference*, National Harbor, MD, Jan. 2014.
DOI:10.2514/6.2014-0545
- [37] Abdulrahim, M., and Lind, R., “Modeling and Control of Micro Air Vehicles with Biologically-Inspired Morphing,” *2016 American Control Conference*, Minneapolis, MN, Jun. 2006.
DOI:10.1109/acc.2006.1656634
- [38] Seigler, T. M., Neal, D. A., and Inman, D. J., “Dynamic Modeling of Large-Scale Morphing Aircraft,” *47th AIAA/ASME/ASCE/AHS/ASC*

Structures, Structural Dynamics and Materials Conference, Newport, RI, May 2006.

DOI:10.2514/6.2006-1893

- [39] Huang, J., Fu, X., and Jing, Z., “Singular Dynamics for Morphing Aircraft Switching on the Velocity Boundary,” *Communications in Nonlinear Science and Numerical Simulation*, Vol. 95, Article 105625, 2021.

DOI:10.1016/j.cnsns.2020.105625

- [40] Li, L., Liu, Z., and Wen, N., “Dynamic Modeling for a Variable-Span and Variable-Sweep Unmanned Aerial Vehicle,” *2016 IEEE Chinese Guidance, Navigation and Control Conference*, Nanjing, China, Aug. 2017.

DOI:10.1109/CGNCC.2016.7828977

- [41] Obradovic, B., and Subbarao, K., “Modeling of Dynamic Loading of Morphing-Wing Aircraft,” *Journal of Aircraft*, Vol. 48, No. 2, 2011, pp. 424–435.

DOI:10.2514/1.C000313

- [42] Wei, C., Wang, R., Zheng, W., and Pu, J., “Equivalent Dynamic Modeling of Flexible Morphing Aircraft,” *Science Progress*, Vol. 104, No. 2, 2021.

DOI:10.1177/00368504211010946

- [43] Shao, P., Zhou, Z., Ma, S., and Bin, L., “Structural Robust Gain-Scheduled PID Control and Application on a Morphing Wing UAV,” *Chinese Control Conference*, Dalian, China, Jul. 2017.

DOI:10.23919/ChiCC.2017.8027856

- [44] Shao, P., Wu, J., Wu, C., and Ma, S., “Model and Robust Gain-Scheduled PID Control of a Bio-Inspired Morphing UAV Based on LPV Method,” *Asian Journal of Control*, Vol. 21, No. 4, 2019, pp. 1681–1705.
DOI:10.1002/asjc.2187
- [45] Dong, C. Y., Li, W., and Wang, Q., “ H_∞ Control of Switched Systems with Nonideal Switchings and Its Application to Morphing Aircraft,” *Proceedia Engineering*, Vol. 67, 2013, pp. 100–109.
DOI:10.1016/j.proeng.2013.12.009
- [46] Jie, Z., “ H_∞ Robust Adaptive Controller for a Morphing Aircraft Based on SRAD and LPV Model,” *2018 Chinese Control and Decision Conference*, Shenyang, China, Jun. 2018.
DOI:10.1109/CCDC.2018.8408044
- [47] Guo, T., Hou, Z., Liu, Z., and Wang, W., “ H_∞ Attitude Control with Initiative Morphing Strategy Based on Linearization for Gull-Wings,” *36th Chinese Control Conference*, Dalian, China, Jul. 2017.
DOI:10.23919/ChiCC.2017.8028358
- [48] Songhui, M., Pengyuan, S., and Chengfu, W., “LPV Based Robust Gain-Scheduling Control for Transient Mode of Morphing UAV,” *Advanced Materials Research*, Vol. 622, 2013, pp. 1368–1372.
DOI:10.4028/www.scientific.net/AMR.622-623.1368
- [49] Wu, C., Shao, P., and Ma, S., “An Effective Design of LPV Based Robust Gain-Scheduling Controller for Morphing-Wing UAV,” *32nd Chinese Control Conference*, Xi’an, China, Jul. 2013.

- [50] Jiang, W., Wu, K., Wang, Z., and Wang, Y., “Gain-Scheduled Control for Morphing Aircraft via Switching Polytopic Linear Parameter-Varying Systems,” *Aerospace Science and Technology*, Vol. 107, Article 106242, 2020.
DOI:10.1016/j.ast.2020.106242
- [51] Li, W., and Jin, D., “Gain-Scheduled Control and Stability Analysis of Morphing Aircraft in Transition Process,” *Transactions of Nanjing University of Aeronautics and Astronautics*, Vol. 35, No. 6, 2018, pp. 1080–1086.
DOI:10.16356/j.1005-1120.2018.06.1080
- [52] Yue, T., Wang, L., and Ai, J., “Gain Self-Scheduled H_∞ Control for Morphing Aircraft in the Wing Transition Process Based on an LPV Model,” *Chinese Journal of Aeronautics*, Vol. 26, No. 4, 2013, pp. 909–917.
DOI:10.1016/j.cja.2013.06.004
- [53] Jiao, X., and Jiang, J., “Learning Control Law of Mode Switching for Hypersonic Morphing Aircraft Based on Type-2 TSK Fuzzy Neural Network,” *International Journal of Machine Learning and Computing*, Vol. 5, No. 4, 2015, pp. 301–306.
DOI:10.7763/ijmlc.2015.v5.524
- [54] Xu, W., Li, Y., Lv, M., and Pei, B., “Modeling and Switching Adaptive Control for Nonlinear Morphing Aircraft Considering Actuator Dynamics,” *Aerospace Science and Technology*, Vol. 1, Article 107349, 2022.
DOI:10.1016/j.ast.2022.107349

- [55] Gong, L., Wang, Q., Hu, C., and Liu, C., “Switching Control of Morphing Aircraft Based on Q-Learning,” *Chinese Journal of Aeronautics*, Vol. 33, No. 2, 2020, pp. 672–687.
DOI:10.1016/j.cja.2019.10.005
- [56] Jiang, W., Dong, C., and Wang, Q., “A Systematic Method of Smooth Switching LPV Controllers Design for a Morphing Aircraft,” *Chinese Journal of Aeronautics*, Vol. 28, No. 6, 2015, pp. 1640–1649.
DOI:10.1016/j.cja.2015.10.005
- [57] Liu, J., Shan, J., Hu, Y., and Rong, J., “Optimal Switching Control for Morphing Aircraft with Aerodynamic Uncertainty,” *2020 IEEE 16th International Conference on Control and Automation (ICCA)*, Singapore, Oct. 2020.
DOI:10.1109/ICCA51439.2020.9264361
- [58] Cheng, H., Dong, C., Jiang, W., Wang, Q., and Hou, Y., “Non-fragile Switched H_∞ Control for Morphing Aircraft with Asynchronous Switching H_∞ Control for Morphing Aircraft,” *Chinese Journal of Aeronautics*, Vol. 30, No. 3, 2017, pp. 1127–1139.
DOI:10.1016/j.cja.2017.01.008
- [59] He, Y., Li, C., Zhang, W., Shi, J., and Lü, Y., “Switching LPV Control Design with Mdatd and Its Application to a Morphing Aircraft,” *Kybernetika*, Vol. 52, No. 6, 2016, pp. 967–987.
DOI:10.14736/kyb-2016-6-0967

- [60] Jiao, X., Fidan, B., Jiang, J., and Kamel, M., “Adaptive Mode Switching of Hypersonic Morphing Aircraft Based on Type-2 TSK Fuzzy Sliding Mode Control,” *Science China Information Sciences*, Vol. 58, No. 7, 2015, pp. 1–15.
DOI:10.1007/s11432-015-5349-z
- [61] Xu, D., Hui, Z., Liu, Y., and Chen, G., “Morphing Control of a New Bionic Morphing UAV with Deep Reinforcement Learning,” *Aerospace Science and Technology*, Vol. 92, 2019, pp. 232–243.
DOI:10.1016/j.ast.2019.05.058
- [62] Valasek, J., Tandale, M. D., and Rong, J., “A Reinforcement Learning - Adaptive Control Architecture for Morphing,” *Journal of Aerospace Computing, Information and Communication*, Vol. 2, No. 4, 2005, pp. 174–195.
DOI:10.2514/1.11388
- [63] Syed, A. A., Khamvilai, T., Kim, Y., and Vamvoudakis, K. G., “Experimental Design and Control of a Smart Morphing Wing System Using a Q-Learning Framework,” *2021 IEEE Conference on Control Technology and Applications (CCTA)*, San Diego, CA, Aug. 2021.
DOI:10.1109/CCTA48906.2021.9658986
- [64] Valasek, J., Doebbler, J., Tandale, M. D., and Meade, A. J., “Improved Adaptive-Reinforcement Learning Control for Morphing Unmanned Air Vehicles,” *IEEE Transactions on Systems, Man, and Cybernetics, Part B: Cybernetics*, Vol. 38, No. 4, 2008, pp. 1014–1020.
DOI:10.1109/TSMCB.2008.922018

- [65] Yao, Z., “Research on Flight Control Method of Morphing UCAV Based on Reinforcement Learning,” *27th Congress of the International Council of the Aeronautical Sciences*, Nice, France, Sep. 2010.
- [66] Gong, L., Wang, Q., Dong, C., and Zhong, K., “Prescribed Performance Control of Morphing Aircraft Based on Switched Nonlinear Systems and Reinforcement Learning,” *Measurement and Control*, Vol. 52, No. 5-6, 2019, pp. 608–624.
DOI:10.1177/0020294019830434
- [67] Tandale, M. D., Rong, J., and Valasek, J., “Preliminary Results of Adaptive-Reinforcement Learning Control for Morphing Aircraft,” *AIAA Guidance, Navigation, and Control Conference and Exhibit*, Providence, RI, Aug. 2004.
DOI:10.2514/6.2004-5358
- [68] Ataei-Esfahani, A., and Wang, Q., “Robust Failure Compensation for a Morphing Aircraft Model Using a Probabilistic Approach,” *IEEE Transactions on Control Systems Technology*, Vol. 15, No. 2, 2007, pp. 324–331.
DOI:10.1109/TCST.2006.883188
- [69] Wu, Z., Lu, J., Shi, J., Liu, Y., and Zhou, Q., “Robust Adaptive Neural Control of Morphing Aircraft with Prescribed Performance,” *Mathematical Problems in Engineering*, Vol. 2017, Article 1401427, 2017.
DOI:10.1155/2017/1401427
- [70] Whitmer, C. E., and Kelkar, A. G., “Robust Control of a Morphing Airfoil Structure,” *2005 American Control Conference*, Portland, OR, Jun. 2005.

DOI:10.1109/acc.2005.1470404

- [71] Jia, Z., Dong, C., Cheng, H., and Wang, Q., “A Robust Fault Detection for Control System of Morphing Aerial Vehicle Based on Switched System Approach,” *27th Chinese Control and Decision Conference*, Qingdao, China, May 2015.

DOI:10.1109/CCDC.2015.7162461

- [72] Liu, C., and Zhang, S., “Novel Robust Control Framework for Morphing Aircraft,” *Journal of Systems Engineering and Electronics*, Vol. 24, No. 2, 2013, pp. 281–287.

DOI:10.1109/JSEE.2013.00035

- [73] He, Y., Zhang, W., Zhang, Y., and Li, C., “Robust Control of Morphing Aircraft Based on Switched Polytopic System,” *2015 IEEE International Conference on Cyber Technology in Automation, Control, and Intelligent Systems*, Shenyang, China, Jun. 2015.

DOI:10.1109/CYBER.2015.7288192

- [74] Qiao, F., Zhang, W., Li, G., Shi, J., Qu, X., Che, J., and Zhou, H., “Robust Adaptive Back-Stepping Control Design Based on RBFNN for Morphing Aircraft,” *2018 IEEE CSAA Guidance, Navigation and Control Conference*, Xiamen, China, Aug. 2018.

DOI:10.1109/GNCC42960.2018.9018937

- [75] Zhang, J., and Wu, S. T., “Robust Controller Design for a Morphing Aircraft Based on SRAD,” *26th Chinese Control and Decision Conference*,

Changsha, China, May 2014.

DOI:10.1109/CCDC.2014.6852195

- [76] Wu, Z., Lu, J., Rajput, J., Shi, J., and Ma, W., “Adaptive Neural Control Based on High Order Integral Chained Differentiator for Morphing Aircraft,” *Mathematical Problems in Engineering*, Vol. 2015, Article 787931, 2015.

DOI:10.1155/2015/787931

- [77] Chandrasekaran, B. K., and Steck, J. E., “An Adaptive Flight Control System for a Morphing Flapping Wing Aircraft,” *AIAA SciTech 2020 Forum*, Orlando, FL, Jan. 2020.

DOI:10.2514/6.2020-0592

- [78] Wu, Z., Lu, J., Zhou, Q., and Shi, J., “Modified Adaptive Neural Dynamic Surface Control for Morphing Aircraft with Input and Output Constraints,” *Nonlinear Dynamics*, Vol. 87, No. 4, 2017, pp. 2367–2383.

DOI:10.1007/s11071-016-3196-0

- [79] Qiao, F., Shi, J., Qu, X., and Lyu, Y., “Adaptive Back-Stepping Neural Control for an Embedded and Tilttable V-Tail Morphing Aircraft,” *International Journal of Control, Automation and Systems*, Vol. 20, No. 2, 2022, pp. 678–690.

DOI:10.1007/s12555-020-0694-0

- [80] Nigam, N., Zhang, Y., Chen, P. C., Wolfe, G., Pillsbury, T., Wereley, N. M., and Suh, P. M., “Adaptive Control and Actuation System Development for Biomimetic Morphing,” *24th AIAA/AHS Adaptive Structures*

Conference, San Diego, CA, Jan. 2016.

DOI:10.2514/6.2016-1084

- [81] Wen, N., Liu, Z., and Zhu, L., “Linear-Parameter-Varying-Based Adaptive Sliding Mode Control with Bounded L_2 Gain Performance for a Morphing Aircraft,” *Proceedings of the Institution of Mechanical Engineers, Part G: Journal of Aerospace Engineering*, Vol. 233, No. 5, 2019, pp. 1847–1864.

DOI:10.1177/0954410018764472

- [82] Wu, Z., Lu, J., and Shi, J., “Adaptive Neural Dynamic Surface Control of Morphing Aircraft with Input Constraints,” *2017 29th Chinese Control And Decision Conference (CCDC)*, Chongqing, China, May 2017.

DOI:10.1109/CCDC.2017.7978057

- [83] Qiao, F., Shi, J., Qu, X., and Lyu, Y., “Hardware-In-Loop Adaptive Neural Control for a Tilttable V-Tail Morphing Aircraft,” *Defence Technology*, 2022, Article in Press.

DOI:10.1016/j.dt.2021.12.012

- [84] Yan, B., Dai, P., Liu, R., Xing, M., and Liu, S., “Adaptive Super-Twisting Sliding Mode Control of Variable Sweep Morphing Aircraft,” *Aerospace Science and Technology*, Vol. 92, 2019, pp. 198–210.

DOI:10.1016/j.ast.2019.05.063

- [85] Wang, Q., Gong, L., Dong, C., and Zhong, K., “Morphing Aircraft Control Based on Switched Nonlinear Systems and Adaptive Dynamic Program-

- ming,” *Aerospace Science and Technology*, Vol. 93, Article 105325, 2019.
DOI:10.1016/j.ast.2019.105325
- [86] Menon, A. N., Chakravarthy, A., and Nguyen, N. T., “Adaptive Control for Hybrid PDE Models Inspired From Morphing Aircraft,” *2018 AIAA Guidance, Navigation, and Control Conference*, Kissimmee, FL, Jan. 2018.
DOI:10.2514/6.2018-0872
- [87] Lee, H., Lee, J., hun Kim, S., Jung, S., and Kim, Y., “Adaptive Control Allocation-Based Control Design for Non-affine Morphing Aircraft System,” *9th European Conference for Aeronautics and Space Sciences (EUCASS)*, Madrid, Spain, Jul. 2019.
DOI:10.13009/EUCASS2019-163
- [88] Yao, L., You, S., Xiaodong, L., and Bo, G., “Control Allocation for a Class of Morphing Aircraft with Integer Constraints Based on Levy Flight,” *Journal of Systems Engineering and Electronics*, Vol. 31, No. 4, 2020, pp. 826–840.
DOI:10.23919/JSEE.2020.000056
- [89] Liu, J., and Wang, J., “Incremental Sliding-Mode Control and Allocation for Morphing-Wing Aircraft Fast Manoeuvring,” *Aerospace Science and Technology*, Vol. 131, Part A, Article 107959, 2022.
DOI:10.1016/j.ast.2022.107959
- [90] Wen, N., Liu, Z., Sun, Y., and Zhu, L., “Design of LPV-Based Sliding Mode Controller with Finite Time Convergence for a Morphing Air-

craft,” *International Journal of Aerospace Engineering*, Vol. 2017, Article 8426348, 2017.

DOI:10.1155/2017/8426348

- [91] Wu, Q., Liu, Z., Liu, F., and Chen, X., “LPV-Based Self-Adaption Integral Sliding Mode Controller with L_2 Gain Performance for a Morphing Aircraft,” *IEEE Access*, Vol. 7, 2019, pp. 81515–81531.

DOI:10.1109/ACCESS.2019.2923313

- [92] Wu, Q., Liu, Z., Ding, B., and Zhu, L., “Design of Sliding Mode Controller with Self-Adaption for a Morphing Aircraft,” *2018 Chinese Automation Congress (CAC)*, Xi’an, China, Nov. 2019.

DOI:10.1109/CAC.2018.8623073

- [93] Xu, L., Lu, Y., He, Z., Yin, M., and Song, C., “Sliding Mode Control of Morphing-Aided Maneuver for Folding Aircraft,” *2018 33rd Youth Academic Annual Conference of Chinese Association of Automation (YAC)*, Nanjing, China, May 2018.

DOI:10.1109/YAC.2018.8406387

- [94] Lee, J., and Kim, Y., “Neural Network-Based Nonlinear Dynamic Inversion Control of Variable-Span Morphing Aircraft,” *7th European Conference for Aeronautics and Space Sciences*, Milan, Italy, Jul. 2017.

DOI:10.13009/EUCASS2017-195

- [95] Tharaka, G., and Aponso, G., *Nonlinear Dynamic Inversion Control of a Miniature Morphing Aircraft*, MS Thesis, Department of Aerospace Engineering, Wichita State University, Wichita, KS, 2013.

- [96] Lee, J., and Kim, Y., “Neural Network-Based Nonlinear Dynamic Inversion Control of Variable-Span Morphing Aircraft,” *Proceedings of the Institution of Mechanical Engineers, Part G: Journal of Aerospace Engineering*, Vol. 234, No. 10, 2020, pp. 1624–1637.
DOI:10.1177/0954410019846713
- [97] Liang, X., Wang, Q., Xu, B., and Dong, C., “Back-Stepping Fault-Tolerant Control for Morphing Aircraft Based on Fixed-Time Observer,” *International Journal of Control, Automation and Systems*, Vol. 19, No. 12, 2021, pp. 3924–3936.
DOI:10.1007/s12555-020-0764-3
- [98] Wu, K. J., Zhang, P. X., and Wu, H., “A New Control Design for a Morphing UAV Based on Disturbance Observer and Command Filtered Backstepping Techniques,” *Science China Technological Sciences*, Vol. 62, No. 10, 2019, pp. 1845–1853.
DOI:10.1007/s11431-018-9377-8
- [99] Liu, H., “Attitude Control of Hypersonic Morphing Aircraft Based on Incremental Backstepping Sliding Mode,” *2022 7th International Conference on Intelligent Computing and Signal Processing (ICSP)*, Xi’an, China, Apr. 2022.
- [100] Wang, L., and Su, J., “Disturbance Rejection Control of a Morphing UAV,” *2013 American Control Conference*, Washington, DC, Jun. 2013.
DOI:10.1109/acc.2013.6580502

- [101] Gong, L., Wang, Q., and Dong, C., “Disturbance Rejection Control of Morphing Aircraft Based on Switched Nonlinear Systems,” *Nonlinear Dynamics*, Vol. 96, No. 2, 2019, pp. 975–995.
DOI:10.1007/s11071-019-04834-9
- [102] Cai, G., Yang, Q., Mu, C., and Li, X., “Design of Linear Parameter-Varying Controller for Morphing Aircraft Using Inexact Scheduling Parameters,” *IET Control Theory & Applications*, 2022.
DOI:10.1049/cth2.12380
- [103] Martin, D. P., Johnson, K. E., Zalkind, D. S., and Pao, L. Y., “LPV-Based Torque Control for an Extreme-Scale Morphing Wind Turbine Rotor,” *2017 American Control Conference*, Seattle, WA, May 2017.
DOI:10.23919/ACC.2017.7963146
- [104] Scherer, C. W., Njio, R. G., and Bennani, S., “Parametrically Varying Flight Control System Design with Full Block Scalings,” *36th IEEE Conference on Decision and Control*, San Diego, CA, Dec. 1997.
DOI:10.1109/cdc.1997.657686
- [105] Mueller, J. B., and Balas, G. J., “Implementation and Testing of LPV Controllers for the NASA F/A-18 Systems Research Aircraft,” *AIAA Guidance, Navigation, and Control Conference and Exhibit*, Denver, CO, Aug. 2000.
DOI:10.2514/6.2000-4446
- [106] Hjartarson, A., Seiler, P., and Balas, G. J., “LPV Analysis of a Gain Scheduled Control for an Aeroelastic Aircraft,” *2014 American Control*

Conference, Portland, OR, Jun. 2014.

DOI:10.1109/ACC.2014.6859301

- [107] Barker, J. M., and Balas, G. J., “Flight Control of a Tailless Aircraft via Linear Parameter-Varying Techniques,” *1999 Guidance, Navigation, and Control Conference and Exhibit*, Portland, OR, Aug. 1999.

DOI:10.2514/6.1999-4133

- [108] Hired, A., Duc, G., Friang, J. P., and Farret, D., “Linear-Parameter-Varying/Loop-Shaping H_∞ Synthesis for a Missile Autopilot,” *Journal of Guidance, Control, and Dynamics*, Vol. 24, No. 5, 2001, pp. 879–886.

DOI:10.2514/2.4821

- [109] Yue, T., Wang, L., and Ai, J., “Longitudinal Linear Parameter Varying Modeling and Simulation of Morphing Aircraft,” *Journal of Aircraft*, Vol. 50, No. 6, 2013, pp. 1673–1681.

DOI:10.2514/1.C031316

- [110] Biannic, J. M., Apkarian, P., and Garrard, W. L., “Parameter Varying Control of a High-Performance Aircraft,” *Journal of Guidance, Control, and Dynamics*, Vol. 20, No. 2, 1997, pp. 225–231.

DOI:10.2514/2.4045

- [111] Lu, B., and Wu, F., “Probabilistic Robust Linear Parameter-Varying Control of an F-16 Aircraft,” *Journal of Guidance, Control, and Dynamics*, Vol. 29, No. 6, 2006, pp. 1454–1460.

DOI:10.2514/1.22495

- [112] Kumar, A., and Andersen, M. R., “A Comparison of LPV Modeling Techniques for Aircraft Control,” *AIAA Guidance, Navigation, and Control Conference and Exhibit*, Denver, CO, Aug. 2000.
DOI:10.2514/6.2000-4458
- [113] Chen, L., Alwi, H., Edwards, C., and Sato, M., “Hardware-In-The-Loop Evaluation of an LPV Sliding Mode Fixed Control Allocation Scheme on the Mupal- α Research Aircraft,” *2017 IEEE Conference on Control Technology and Applications (CCTA)*, Maui, HI, Aug. 2017.
DOI:10.1109/CCTA.2017.8062526
- [114] Marcos, A., and Balas, G. J., “Development of Linear-Parameter-Varying Models for Aircraft,” *Journal of Guidance, Control, and Dynamics*, Vol. 27, No. 2, 2004, pp. 218–228.
DOI:10.2514/1.9165
- [115] Rotondo, D., Nejjari, F., and Puig, V., “Model Reference Quasi-LPV Control of a Quadrotor UAV,” *2014 IEEE Conference on Control Applications (CCA)*, Juan Les Antibes, France, Oct. 2014.
DOI:10.1109/CCA.2014.6981428
- [116] Shin, J. Y., Balas, G. J., and Kaya, M. A., “Blending Methodology of Linear Parameter Varying Control Synthesis of F-16 Aircraft System,” *Journal of Guidance, Control, and Dynamics*, Vol. 25, No. 6, 2002, pp. 1040–1048.
DOI:10.2514/2.5008

- [117] Lu, B., *Linear Parameter-Varying Control of an F-16 Aircraft at High Angle of Attack*, Ph.D. Dissertation, Department of Mechanical and Aerospace Engineering, North Carolina State University, Raleigh, NC, 2004.
- [118] Lu, B., Wu, F., and Kim, S. W., “Switching LPV Control of an F-16 Aircraft via Controller State Reset,” *IEEE Transactions on Control Systems Technology*, Vol. 14, No. 2, 2006, pp. 267–277.
DOI:10.1109/TCST.2005.863656
- [119] Natesan, K., Gu, D. W., and Postlethwaite, I., “Design of Static H_∞ Linear Parameter Varying Controllers for Unmanned Aircraft,” *Journal of Guidance, Control, and Dynamics*, Vol. 30, No. 6, 2007, pp. 1822–1827.
DOI:10.2514/1.31283
- [120] Cheng, H., Dong, C., Wang, Q., and Jiang, W., “Smooth Switching Linear Parameter-Varying Fault Detection Filter Design for Morphing Aircraft with Asynchronous Switching,” *Transactions of the Institute of Measurement and Control*, Vol. 40, No. 8, 2018, pp. 2622–2638.
DOI:10.1177/0142331217708238
- [121] Shao, P., Dong, Y., and Ma, S., “Model Predictive Control based on Linear Parameter-Varying Model for a Bio-inspired Morphing Wing UAV,” *2021 International Conference on Robotics and Control Engineering*, Tokyo, Japan, Apr. 2021.
DOI:10.1145/3462648.3462669

- [122] Ganguli, S., Marcos, A., and Balas, G., “Reconfigurable LPV Control Design for Boeing 747-100/200 Longitudinal Axis,” *2002 American Control Conference*, Anchorage, AK, May 2002.
DOI:10.1109/acc.2002.1024489
- [123] Balas, G. J., Fialho, I., Packard, A., Renfrow, J., and Mullaney, C., “On the Design of LPV Controllers for the F-14 Aircraft Lateral-Directional Axis During Powered Approach,” *1997 American Control Conference*, Albuquerque, NM, Jun. 1997.
DOI:10.1109/acc.1997.611768
- [124] Basargan, H., Mihály, A., Gáspár, P., and Sename, O., “LPV-Fuzzy Control Approach for Road Adaptive Semi-active Suspension System,” *2022 IEEE Intelligent Vehicles Symposium (IV)*, Aachen, Germany, Jun. 2022.
DOI:10.1109/IV51971.2022.9827195
- [125] Liu, Y., Ban, X., Wu, F., and Lam, H. K., “A Gain-Scheduling Control Approach for Takagi-Sugeno Fuzzy Systems Based on Linear Parameter-Varying Control Theory,” *Journal of Dynamic Systems, Measurement and Control*, Vol. 138, No. 1, 2016, pp. 011008.
DOI:10.1115/1.4031914
- [126] Wu, F., *Control of Linear Parameter Varying Systems*, Ph.D. Dissertation, Department of Mechanical Engineering, University of California at Berkeley, Berkeley, CA, 1995.
- [127] Hjartarson, A., Seiler, P., and Packard, A., “LPVTools: A Toolbox for Modeling, Analysis, and Synthesis of Parameter Varying Control Sys-

tems,” 2015.

DOI:10.1016/j.ifacol.2015.11.127

- [128] Boef, P. D., Cox, P. B., and Tóth, R., “LPVcore: MATLAB Toolbox for LPV Modelling, Identification and Control,” 2021.

DOI:10.1016/j.ifacol.2021.08.390

- [129] Bae, J. S., Seigler, T. M., and Inman, D. J., “Aerodynamic and Static Aeroelastic Characteristics of a Variable-Span Morphing Wing,” *Journal of Aircraft*, Vol. 42, No. 2, 2005, pp. 528–534.

DOI:10.2514/1.4397

- [130] Anderson, J. D., *Aircraft Performance and Design*, McGraw-Hill Education, New York, NY, 1999.

- [131] Stevens, B. L., Johnson, E. N., and Lewis, F. L., *Aircraft Control and Simulation: Dynamics, Controls Design, and Autonomous Systems*, John Wiley & Sons, Hoboken, NJ, 3rd ed., 2015.

- [132] Park, S., Deyst, J., and How, J. P., “A New Nonlinear Guidance Logic for Trajectory Tracking,” *AIAA Guidance, Navigation, and Control Conference and Exhibit*, Providence, RI, Aug. 2004.

DOI:10.2514/6.2004-4900

국문초록

본 논문에서는 모핑 무인 항공기(unmanned aerial vehicle: UAV)의 비행 제어를 위한 새로운 프레임워크가 제안된다. 제안된 기법은 모핑 구동기의 동적 특성을 고려한 횡방향축(lateral-directional) 운동 제어를 위해 비대칭 스펠 모핑을 사용하고 종축(longitudinal) 비행 성능 향상을 위해 대칭 스펠 모핑의 이점을 활용한다. 또한 설계된 제어 시스템은 선형 파라미터 가변(linear parameter-varying: LPV) 기법을 기반으로 제어가 이득이 자체적으로 스케줄링되며 모핑 형상 및 비행 조건의 임의의 변화에 대해 안정성과 성능을 엄밀하게 보장한다. 따라서 모핑 UAV는 기동 명령과 비행 조건에 따라 안정성을 상실할 우려 없이 시스템 수준의 이점을 극대화하는 동시에 내부 루프 안정화를 위한 제어에 기여하도록 최적의 형상으로 신속하게 변형될 수 있다.

첫째, NASA GTM(generic transport model)으로부터 비대칭 가변 스펠 모핑 UAV의 고충실도(high-fidelity) 비선형 모델이 획득된다. 모핑이 질량 중심, 관성 행렬 및 공기역학 계수에 미치는 영향은 날개가 비대칭적으로 손상된 모델을 기반으로 도출된다. 좌우 날개의 스펠 변화율은 대칭 및 비대칭 모핑 파라미터로 분해되며, 두 모핑 파라미터는 각각 스케줄링 파라미터 및 제어 입력으로 간주된다. 비선형 모델을 종축 및 횡방향축 운동으로 분리하고 직사각형 형태의 스케줄링 파라미터 영역의 각 격자점에서 선형화함으로써 각 점에 대한 선형 시불변(linear time-invariant: LTI) 모델이 얻어진다. LTI 모델 집합에 보간(interpolation)을 적용하면 종축 및 횡방향축 운동에 대한 모핑 UAV의 LPV 모델이 얻어진다.

둘째, 수직 가속도(normal acceleration) 명령과 옆미끄럼각(angle of sideslip) 및 롤 각속도 명령 추종을 위해 LPV 기법을 기반으로 종축 및 횡방향축 제어 증

강 시스템(control augmentation system)이 설계된다. 이때, 제어 설계 과정에서 주파수중속(frequency-dependent) 가중치 필터를 통해 낮은 대역폭(bandwidth) 과 같은 모핑 구동기 고유의 동적 특성이 고려된다. 또한 비행 특성에 대한 모핑의 다양한 영향을 고려하여 실행하고자 하는 기동을 보조하기 위한 스펙 모핑 전략이 논의된다. Pushover-pullup 기동 및 high-g turn에 대한 수치 시뮬레이션 결과를 통해 제안된 기법이 타당함을 확인할 수 있다.

마지막으로, 대기속도(airspeed) 및 고도 명령과 옆미끄럼각 및 롤 각 명령을 추종하기 위해 LPV 기법을 기반으로 종축 및 횡방향축 자동 조종 장치(autopilot)가 설계된다. 이때, 3차원 경로 추종을 위해 비선형 유도 법칙이 자동 조종 장치와 결합된다. 경로 추종 비행에 대한 수치 시뮬레이션 결과를 통해 스케줄링 파라미터의 변화 속도가 빠르거나 변화의 폭이 넓은 경우 일반적인 이득스케줄 제어기는 안정성을 상실할 수 있는 반면 제안된 기법은 만족할 만한 성능을 유지함을 확인할 수 있다.

주요어: 모핑 항공기, 무인 항공기, 선형 파라미터 가변 제어, 게인 스케줄링, 강건 제어, 비행 제어 시스템, 조종성 증강장치, 자동조종장치, 경로 추종, 비선형 유도
학번: 2014-22511